HAL open science

Quantum transport of holes in WSe2 monolayers under high magnetic field

Banan Khaled Kerdi

To cite this version:

Banan Khaled Kerdi. Quantum transport of holes in WSe2 monolayers under high magnetic field. Condensed Matter [cond-mat]. Université Paul Sabatier - Toulouse III, 2021. English. NNT : 2021TOU30009 . tel-03236106

HAL Id: tel-03236106

https://theses.hal.science/tel-03236106

Submitted on 26 May 2021

HAL is a multi-disciplinary open access archive for the deposit and dissemination of scientific research documents, whether they are published or not. The documents may come from teaching and research institutions in France or abroad, or from public or private research centers.

L'archive ouverte pluridisciplinaire **HAL**, est destinée au dépôt et à la diffusion de documents scientifiques de niveau recherche, publiés ou non, émanant des établissements d'enseignement et de recherche français ou étrangers, des laboratoires publics ou privés.

THÈSE

En vue de l'obtention du

DOCTORAT DE L'UNIVERSITÉ DE TOULOUSE

Délivré par l'**U**niversité Toulouse 3 - Paul Sabatier

Présentée et soutenue par

Banan Khaled KERDI

Le 5 Février 2021

Transport quantique des trous dans une monocouche de WSe_2 sous champ magnétique intense.

Ecole doctorale : **SDM - SCIENCES DE LA MATIERE - Toulouse**

Spécialité : **Physique de la matière**

Unité de recherche :
LNCMI - Laboratoire National des Champs Magnétiques Intenses

Jury

M. Ning WANG, Université de Hong Kong	Rapporteur
M. Benoît JOUAULT, Université de Montpellier	Rapporteur
M. Uli ZEITLER, Université de Radboud- Nimègue	Examinateur
Mme Virginie SERIN, Université Paul Sabatier	Examinatrice
M. Mathieu PIERRE, INSA-Toulouse	Membre invité
M. Walter ESCOFFIER, INSA-Toulouse	Directeur de thèse
M. Michel GOIRAN, Université Paul Sabatier	Co-directeur de thèse

Many Thanks for everyone who contributed in the achievement of this work.

A special thanks for Walter ESCOFFIER, Mathieu PIERRE and Michel GOIRAN.

Contents

Abstracts v

Acronym vii

General introduction ix

1 Structural and electronic properties of WSe_2 1
- 1.1 Introduction . . . 1
- 1.2 Crystal structure . . . 2
- 1.3 Symmetry properties and space group for TMDCs . . . 3
  - 1.3.1 Monolayer-TMDC with trigonal prismatic configuration and TMDCs with odd number of layers . . . 4
  - 1.3.2 Monolayer-TMDC with octahedral coordination and other TMDCs with even number of layers . . . 4
  - 1.3.3 Symmetry group of the wave vector . . . 5
  - 1.3.4 Consequence of the Kramers theorem on the TMDC band structure . . . 6
- 1.4 Electronic band-structure . . . 7
  - 1.4.1 Mono-layer WSe_2 . . . 8
  - 1.4.2 Bi-layer WSe_2 . . . 11
  - 1.4.3 Band gap from mono-layer to bulk TMDCs . . . 12
  - 1.4.4 Few-layer WSe_2 . . . 13

2 Electronic transport 15
- 2.1 Classical approach to charge transport . . . 15
  - 2.1.1 The Drude model of conductivity . . . 16
  - 2.1.2 Boltzmann transport equation without magnetic field . . . 17
  - 2.1.3 Electrical conductivity in the presence of a magnetic field . . . 21
  - 2.1.4 Boltzmann transport equation in the presence of a magnetic field 26
- 2.2 Transport phenomena in quantizing Magnetic . . . 30
  - 2.2.1 Landau levels . . . 31

2.2.2 Landau levels broadening 34
2.2.3 Shubnikov-de Haas oscillations 36
2.2.4 Zeeman energy 39
2.2.5 Standard analysis of the Shubnikov-de Haas oscillations 41

3 Experimental techniques 45
3.1 Device fabrication and electrical characterization 45
3.1.1 From 3D to 2D transition metal dichalcogenides 45
3.1.2 Device processing 48
3.1.3 Thickness determination 55
3.1.4 Electrical characterisation 59
3.2 Measurements in pulsed magnetic field and low temperature 65
3.2.1 Pulsed magnetic field generation 65
3.2.2 Cryogenics 66
3.2.3 Insert and sample holder 67
3.2.4 Data acquisition and induced voltage removal 68

4 Quantum oscillations in a p-doped WSe_2 monolayer 71
4.1 Sample characterization and magneto-transport 72
4.1.1 Fabrication 72
4.1.2 Characterization 72
4.1.3 High magnetic field measurements 74
4.1.4 Effective mass 76
4.2 Magneto-transport simulation 77
4.2.1 Schrödinger fermions or massive Dirac fermions ? 77
4.2.2 Electro-chemical potential 78
4.2.3 Self-consistent determination of the electrochemical potential . 79
4.2.4 Components of the conductivity tensor 80
4.2.5 Simulations 83
4.3 Experimental determination of the Landé factor 87
4.3.1 Multiplicity of the ratio E_z/E_c 87
4.3.2 Carrier density evolution of the g-factor 88
4.4 Concluding remarks 91

5 Conclusion 95

6 Résumé en français 99
6.1 Introduction 99
6.2 Propriétés électroniques des dichalcogénures de métaux de transition . 100
6.2.1 Généralités 100

6.2.2 Monocouche 100
6.2.3 Bicouche 102
6.2.4 Multi-couche 103
6.3 Transport électronique 104
6.3.1 Modèle classique de Drude 104
6.3.2 Transport sous champ magnétique intense 105
6.4 Fabrication des dispositifs et caractérisation électrique 108
6.4.1 Dichalcogénures de métaux de transition : de 3D à 2D 108
6.4.2 Fabrication et adressage électrique des échantillons 109
6.4.3 Caractérisation structurale et mesure de l'épaisseur des flocons h-BN/WSe_2 110
6.4.4 Caractérisations électriques 111
6.4.5 Génération de champ magnétique pulsé 112
6.5 Oscillations quantiques dans une monocouche de WSe_2 dopée P . . . 114
6.5.1 Caractérisation des échantillons et magnéto-transport 114
6.5.2 Simulation du magnéto-transport 116
6.5.3 Détermination expérimentale du facteur de Landé 118
6.6 Conclusion 120

List of Figures 122

List of Tables 132

Bibliography 133

Abstracts

Transport quantique des trous dans une monocouche de WSe_2 sous champ magnétique intense.

Les dichalcogénures des métaux de transition sont constitués d'un empilement de monocouches atomiques liées entre elles par des liaisons faibles de type Van der Waals. Lorsqu'une monocouche de ce matériau est isolée, la symétrie d'inversion du cristal est brisée et la présence d'un couplage spin-orbite fort introduit une levée de dégénérescence des états électroniques ayant des spins différents. Le facteur de Landé effectif ($g^\star$) qui intervient dans l'énergie Zeeman est un paramètre qui caractérise, entre autres, la structure de bande du matériau. Il est exceptionnellement grand dans le système WSe_2 en raison de la présence de tungstène et des interactions électroniques. Sa détermination au travers des mesures de résistance électrique sous champ magnétique intense est l'objet de cette thèse.
Dans un premier temps, des monocouches de WSe_2 sont produites par l'exfoliation mécanique du matériau massif et leur adressage électrique à l'échelle micrométrique est réalisé par des procédés technologiques de salle blanche impliquant la lithographie électronique. La magnétorésistance des échantillons produits est ensuite étudiée dans des conditions extrêmes de basse température et de champ magnétique intense. La densité de porteur de charges, des trous dans le cas cette thèse, peut être ajustée in-situ par effet de champ.
Dans les monocouches de WSe_2, la quantification de l'énergie des niveaux de Landau modifiée par l'effet Zeeman est révélée par la présence d'oscillations complexes de la magnéto-résistance (oscillations de Shubnikov-de Haas). Le développement d'un modèle théorique dédié, où le désordre est pris en compte par un élargissement Gaussien des niveaux de Landau, est nécessaire afin d'interpréter quantitativement les résultats expérimentaux. Il simule l'évolution des composantes du tenseur de résistivité où les paramètres d'ajustement sont la mobilité électronique, l'énergie des bords de mobilité des niveaux de Landau ainsi que le facteur de Landé effectif. L'ajustement théorique aux résultats expérimentaux permet d'extraire l'évolution de $g^\star$ des trous en fonction de leur densité dans une gamme variant de 5.10^{12} à $7.5.10^{12}$ cm^{-2}, qui s'inscrit dans la continuité des résultats issus de la littérature. Au-délà des approches novatrices sur le plan des conditions expérimentales et de modélisation, cette étude confirme l'importance des interactions électroniques dans la compréhension des propriétés électroniques de ce matériau.

Mots clés: Champ magnétique intense, métaux de dichalcogénure de transition, monocouche, brisure de symetrie, transport quantique, effet de Shubnikov-de Haas, niveaux de Landau, énergie cyclotron, énergie Zeeman, facteur de landé effectif.

Quantum transport of holes in WSe_2 monolayers under high magnetic field.

Transition metal dichalcogenides are made up of a stack of atomic monolayers bound together by weak Van der Waals interactions. When a single layer of this material is isolated, the crystal inversion symmetry is broken, leading to the degeneracy lifting of the electronic states having different spins in the presence of strong spin-orbit coupling. The effective Landé factor ($g^\star$) which arises in the Zeeman energy is a parameter which characterizes, among others, the band-structure of the material. It is exceptionally large in WSe_2 monolayers thanks to the presence of heavy tungsten atoms as well as electronic interactions. Its experimental determination through electrical resistance measurements under intense magnetic field constitutes the objective of this thesis.
First, WSe_2 monolayers are produced by mechanical exfoliation of the mother material and their electrical addressing at the micrometric scale is achieved by clean room processes involving electron-beam lithography. Their magneto-resistance is studied under extreme conditions of low temperature and high magnetic field. The charge carrier density, holes in the thesis, can be varied in situ thanks to field effect.
In WSe_2 monolayers, the quantization of the Landau level energy modified by the Zeeman effect is revealed by the presence of complex magneto-resistance oscillations (Shubnikov-de Haas oscillations). A dedicated theoretical model, where disorder is introduced through a Gaussian broadening of the Landau levels, is necessary for a quantitative understanding of the experimental results. The components of the resistivity tensor are simulated by this model where the main fitting parameters are the electronic mobility, the mobility edge of the Landau levels and the effective Landé factor. The fitting of the experimental results allows the extraction of $g^\star$ for a hole density ranging from 5.10^{12} to $7.5.10^{12}$ cm^{-2}, which follows the trend reported in the literature. Beyond the innovative approaches in terms of experimental conditions and modelling, this study confirms the importance of electronic interactions in understanding the electronic properties of this material.

Key words: High magnetic field, Transition metal dichalcogenide, monolayer, symmetry breaking, quantum transport, Shubnikov-de Haas effect, Landau levels, cyclotron energy, Zeeman energy, effective landé factor

Acronym

2DEG two dimensional electron gas

2DHG two dimensional hole gas

FET Field effect transistor

TMDCs Transition metal dichalcogenides

MTMDs monolayer transition metal dichalcogenides

WSe_2 tungsten diselenide

h-BN hexagonal boron nitride

SiO_2 Silicon dioxide

RF Radio Frequency

SC semi-conductor

LLs Landau levels

SdHO Shubnikov-de Haas oscillations

AFM atomic force microscopy

SOC spin-orbit coupling

FBZ first Brillouin zone

MDF massive Dirac fermions

SCHF Schrödinger fermions

DOS Density of states

2D two dimensional

vdW van der Waals

DFT density functional theory

i inversion symmetry

CVD Chemical Vapour Deposition

MBE Molecular Beam Epitaxy

CBM conduction band minimum

VBM valence band maximum

VB valence band

CB conduction band

PL Photo-luminescence

TEM Transmission electron microscopy

ARPES Angle-Resolved Photo-Emission Spectroscopy

BF-STEM Bright field-scanning transmission electron microscopy

General introduction

The theory of quantum mechanics describes elementary particles such as electrons with complex wave-functions. Similar to optical or mechanical waves, the confinement of electrons into one or several dimensions results in standing wave-functions whose associated quantized energy spectrum provides the systems with properties that are different from those of the bulk material from which they originate. The rapid development of techniques for manufacturing, observing, handling and characterizing confined systems from the middle of the 20th century opened a broad research field aiming at exploring these new properties of matter with reduced dimensions. One of the most interesting and studied systems is certainly the two-dimensional gas of charged particles. In this system, electrons (or holes) can evolve freely within a plane, while their confinement in the third dimension quantifies their energy into discrete energy levels. Historically, the first 2D electronic systems were fabricated in MOS-FET hetero-junctions and at the interface of GaAs/AlGaAs a few years laterby taking advantage of the built-in electrostatic potential well. At low temperature, the electronic properties of two-dimensional systems differ from their bulk counterparts, but the most surprising effect arises with the application of a sufficiently intense magnetic field perpendicular to the confinement plane. The in-plane energy spectrum of the electrons is quantized into Landau levels and gives rise to remarkable transport properties. When the match between the electron density and the intensity of the magnetic field is favorable, the electrical resistance of the system is exactly zero while the Hall resistance is equal to integer fractions of the resistance quantum h/q^2, defined only via the fundamental elementary charge q and the Planck constant h. This effect, named "Quantum Hall effect", was celebrated by the 1985 Nobel prize attributed to Klaus von Klitzing [1]. Shortly afterwards, the physics of two-dimensional electron systems was once again honored through the discovery of the fractional quantum Hall effect, whose authors Horst Störmer, Daniel Tsui and Robert B. Laughlin were also awarded the Nobel Prize in 1998 [2]. The interest aroused by these discoveries was no less linked to the theoretical interpretation of quantum transport than to the measurement of a fundamental quantity (the Hall resistance) independent of the microscopic details and the chemical nature of the host materials. The physics of two-dimensional electronic systems was again in the spotlight in the early 2000s with the discovery of graphene [3] by K. Novoselov and A. Geim, a monoatomic layer of carbon atoms arranged in a hexagonal lattice. This major discovery marked the marriage of nano-sciences and the physics of two-dimensional electron gases. Indeed, for the first time, charge carriers were no longer confined in a potential well resulting from semiconductor engineering, but in an object whose thickness reaches the ultimate limit of a single atom. Graphene was revolutionary in many ways: on one hand it changed the paradigm according to which purely 2D materials could not be stable at room temperature, and on the other hand it brought a revival of interest to the quantum Hall effect in which the values of the Hall resistance (still an integer fraction of the resistance quantum) are intimately linked to the nature of the quasi-particles ultimately defined by the atomic lattice of the material. But even beyond the major

theoretical advances of which it was the precursor (topological matter crowned by the Nobel Prize of 2016 [4]), its success lies above all in the simplicity of its manufacture, requiring only a roll of adhesive tape and eventually the technologies of electrical addressing already in place for conventional semiconductors. This manufacturing technique, named micro-mechanical exfoliation depicted in figure 1-a), is actually suitable for all materials made up of a stack of mono-atomic 2D layers interacting with each other via weak Van der Waals interactions. Their unprecedented transport and optical properties opened the exploration of many research routes where new degrees of freedom involving the spin or the valley index in addition to the charge could be exploited for future applications (see figure 1-b). The materials belonging to the family of transition metal dichacogenides are at the forefront of these research perspectives.

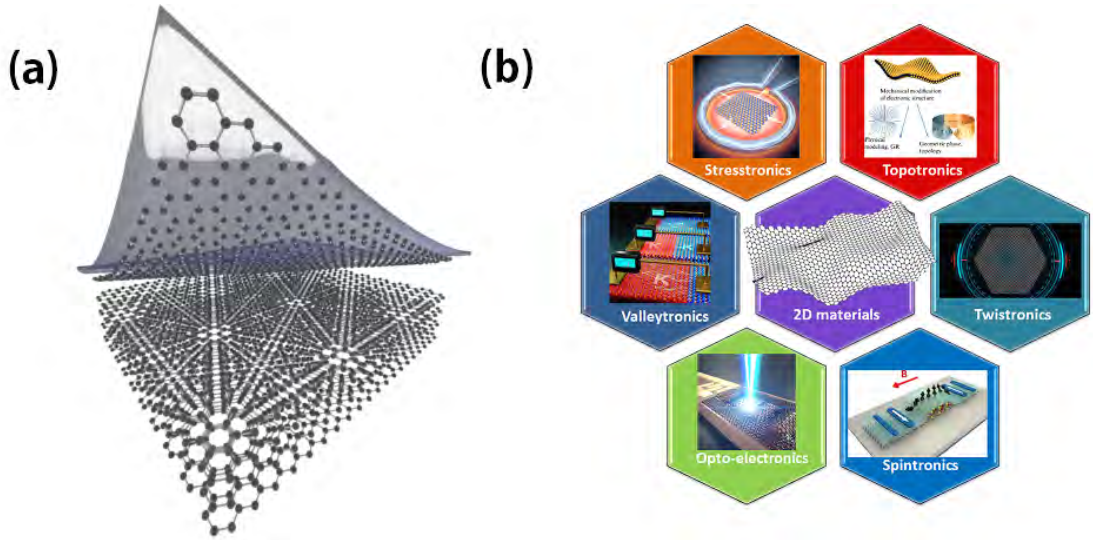

Figure 1: Left: Artistic view of micro-mechanical exfoliation of a mono-atomic layer of graphene using an adhesive tape. Right: Range of two-dimensional materials properties for potential applications.

Contrary to graphene, the transition metal dichalcogenides have a bandgap separating the valence from the conduction bands. Corresponding to visible light, the bandgap is indirect in bulk materials and turns into a direct one when the material is thinned down to a monolayer. Beyond the evident opto-electronic applications, the large spin-orbit coupling originating from the heavy metallic atoms and the broken inversion symmetry of the cristallographic structure make transition metal dichalocogenides monolayers a fertile playground for fundamental research. Indeed, the electronic properties involves both the spin and the valley degrees of freedom which are

strongly coupled by the spin-orbit interaction. This dissertation is focused on the fundamental electronic properties of monolayer tungsten diselenide (WSe_2), a member of the transition metal dichalcogenides family with the largest spin-orbit interaction. We make use of extreme conditions of intense magnetic field and low temperature to quantize the energy spectrum into discrete energy levels, which affect in turn the measured transport properties such as the electrical resistance. The magneto-resistance fingerprints are analyzed to ultimately reveal the ground state of the system, providing experimental evidences for the theoretical models. In particular, we extracted the experimental values of the effective Landé factor for hole quasi-particles (valence band) and its enhancement beyond its expected value (band-structure calculations) due to electron-electron interactions. Besides, this work constitutes the first achievement of quantum transport measurements of WSe_2 monolayers using a pulsed magnetic field. The use of very intense magnetic field (55 T) allows reaching the quantum transport regime even for samples with moderate electronic mobility, produced without complicated engineering methods. It paves the route for future technical improvements and the measurement of alternative Transition metal dichalcogenides (TMDCs) materials of higher quality.

This dissertation is organized in the following way. The chapter 1 describes the crystal structure of monolayer, bilayer and multilayer (even- and odd- number of layers) transition metal dichalcogenides as well as the group symmetry to whom they belong. In the same chapter, their main optical and electronic properties are briefly discussed. Chapter 2 is dedicated to the transport properties of a gas of charged particles. This theoretical chapter is written in a pedagogical way: I describe first the simplest concept of electronic transport considering the single-particle classical approach (Drude model), before introducing a statistical description of the electron gas referred to the Boltzmann model. Next, I comment how the dynamics of charged particles are modified by an external weak magnetic field, and the consequences on magneto-transport. Finally, for high magnetic field, the quantum nature of electrons cannot be ignored and I discuss how the energy spectrum of a 2D electron gas turns into discrete energy levels by solving the Schrödinger equation in the presence of a magnetic field. After analyzing the effects on magneto-transport and the related emergence of Shubnikov-de Haas oscillations, I comment on the Zeeman energy which is another energy scale competing with the cyclotron gap. Next, chapter 3 describes in details the fabrication techniques of monolayer WSe_2 and its electrical addressing. We discuss the influence of the metallic electrodes, leading to the emergence of Schottky barriers, which restrict the charge carrier injection in the system. This chapter also describes the different techniques to determine precisely the thickness of the WSe_2 flakes obtained by micro-mechanical exfoliation. The rest of this chapter is

dedicated to magneto-transport measurements under pulsed magnetic field. Finally, chapter 4 presents and analyses the magneto-transport results obtained from a monolayer WSe_2 sample. The measured quantum oscillations' pattern is beyond a simple interpretation in terms of energy levels separated each other from the cyclotron gap and the Zeeman energy must be taken into account. For this purpose, I detail a model to simulate the magneto-resistance which is compared to the experimental results. This analysis allows extracting transport parameters and most particularly the effective Landé factor. Its evolution with the carrier density, modified *in situ* using a back-gate voltage, constitutes a direct evidence of the important role played by the electron-electron interactions in monolayer WSe_2 systems.

Chapter 1

Structural and electronic properties of WSe_2

Contents

1.1 Introduction **1**

1.2 Crystal structure **2**

1.3 Symmetry properties and space group for TMDCs **3**

1.3.1 Monolayer-TMDC with trigonal prismatic configuration and TMDCs with odd number of layers 4

1.3.2 Monolayer-TMDC with octahedral coordination and other TMDCs with even number of layers 4

1.3.3 Symmetry group of the wave vector 5

1.3.4 Consequence of the Kramers theorem on the TMDC band structure 6

1.4 Electronic band-structure **7**

1.4.1 Mono-layer WSe_2 8

1.4.2 Bi-layer WSe_2 11

1.4.3 Band gap from mono-layer to bulk TMDCs 12

1.4.4 Few-layer WSe_2 13

1.1 Introduction

There are about 60 different compounds belonging to the TMDCs family. Two-third of these assume a layered structure [25] of the form MX_2, where M stands for groups 4-10 transition metal atoms and X stands for the chalcogen atoms (see figure1.1-a). TMDCs monolayers are made of M structure, many of these stochiometric planes are stacked upon each other and the stability of the crystal is ensured by weak van der Waals (vdW) interactions as depicted in figure 1.1-b[25].

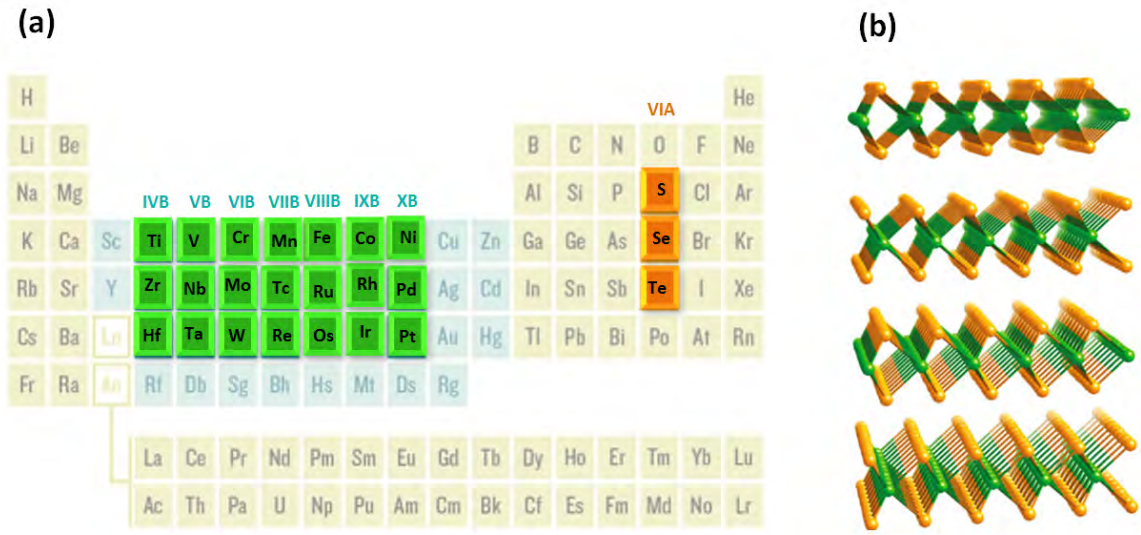

Figure 1.1: (a) Periodic classification of elements, where groups 4-10 transition metal atoms and chalcogen atoms have been highlighted. b) Schematics of the layered atomic structure of the transition metal dichalcogenides.

1.2 Crystal structure

Monolayer TMDCs consists of three atomic planes. The top and bottom planes are chalcogen atoms arranged in a triangular lattice, and the middle plane is also a triangular lattice of metal atoms. There are two polymorphs of mono-layer TMDCs with atomic trigonal prismatic (H) and octahedral (T) coordination of the metal atom as shown in figure 6.1-a. Monolayer TMDCs (stochiometric planes) are the building blocks from which complex 3D crystals are formed. Bulk TMDCs can be found in three polymorphs called 1T, 2H and 3R. In this nomenclature, the number indicates how many MX_2 layers are present in the unit cell while the letter stands for the symmetry group (T for trigonal, H for hexagonal, R for rhombohedral) [32]. These polymorphs are schematically shown in figure 6.1-b. The unit cell is sketched with the c-axis perpendicular to the layers while the parameter a represents the minimal in-plane distance between two chalcogen atoms. TMDCs crystals with trigonal symmetry are charaterized by one layer per unit cell and an octahedral coordination of the metal atoms. On the other hand, the hexagonal symmetry is described with two layers per unit cell and a trigonal prismatic coordination of the metal atoms. Finally, the rhombohedral symmetry maintains the trigonal prismatic coordination of the metal atoms, but is defined with three layers per unit cell shifted by each other. First-principle calculations show that 2H stacking is the most stable configuration. Upon

reducing the number of TMDCs layers down to unity, the symmetry elements of the system undergo drastic changes which translate into modifications of the material's electronic structure, affecting directly the optical and transport properties.

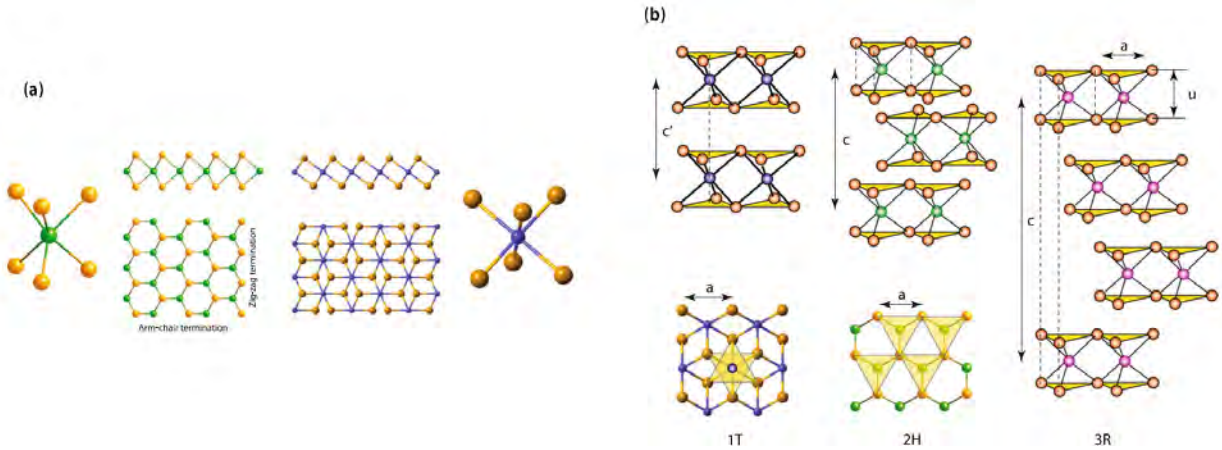

Figure 1.2: (a) Side and top views of the two polymorphs of monolayer TMDCs. Left panel trigonal prismatic (2H); right panel octahedral (1T). Chalcogen and metal atoms are shown in orange and green/violet, respectively .(b) Schematics of the structural polytypes of TMDCs from left to right 1T (tetragonal symmetry, one layer per unit cell and, octahedral coordination of the metal), 2H (hexagonal symmetry with two layers per unit cell and trigonal prismatic coordination) and 3R (rhombohedral symmetry with three layers per unit cell and trigonal prismatic coordination of the metal atoms). The yellow-filled triangles highlight the spatial position of the chalcogen atoms. For the 1T and 2H polytypes, top views are additionally shown. Note that in these images the yellow triangles highlight spatial positions of the chalcogen atoms. Adapted from [28].

1.3 Symmetry properties and space group for TMDCs

The symmetry elements of TMDCs depend on the metal atom coordination and whether the total number of layers is odd or even. The difference between these two groups is ultimately given by the presence or absence of point inversion symmetry.

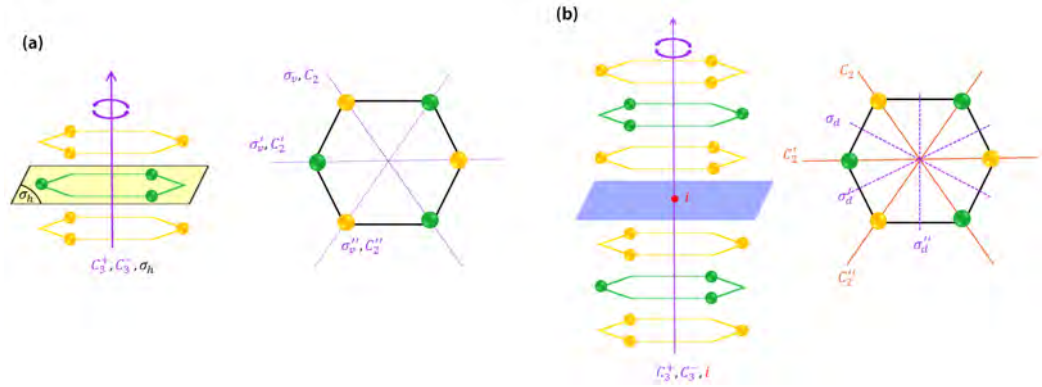

Figure 1.3: Representation of symmetry elements for (a) monolayer and (b) bi-layer TMDCs (both with trigonal prismatic configuration of the metal atom). The chalcogen and metal atoms are shown in orange and green respectively. σ_h is the mirror symmetry operation by the horizontal planes sketched in yellow for monolayer and violet for bilayer. The red dot in inset (b) is an inversion symmetry point.

1.3.1 Monolayer-TMDC with trigonal prismatic configuration and TMDCs with odd number of layers

Monolayer TMDCs with trigonal prismatic configuration belongs to the D^1_{3h} hexagonal space group [27], as well as other few-layer TMDCs with odd (> 1) number of layers. The symmetry elements characterizing these compounds are the identity (E), the clockwise and anticlockwise rotations of 120° (C_3^+ and C_3^-) along the axis perpendicular to the TMDCs plane ; as well as the mirror symmetry (σ_h) by the plane passing through the transition metal atoms shown in figure 1.3-a. The system is also unchanged upon 180° rotation along the three in-plane axis C_2 oriented 120° each other, connecting two opposite corners of the in-plane projection of the hexagonal unit cell. Mirror reflections, noted σ_v, by the three vertical planes that contain the aforementioned axis are other symmetry elements of the monolayer. Besides, the symmetry elements also include two S_3 operations, namely the clockwise and anticlockwise rotations followed by the reflection σ_h by the horizontal plane . It is worth noting that these systems lack inversion symmetry.

1.3.2 Monolayer-TMDC with octahedral coordination and other TMDCs with even number of layers

Monolayer-TMDC with octahedral configuration of the metal atom and any other few-layer TMDCs with an even number of layers belong to the D^3_{3d} hexagonal space group [27]. The symmetry operations which leave the system unchanged are: the identity

(E) as well as the clockwise and anticlockwise rotations of 120° (C_3^+ and C_3^-) along c-axis represented in figure 1.3-b. These systems also hold inversion symmetry (i) where the point of inversion is depicted as the red dot. Another symmetry elements include the 180° rotations along axes placed in between two adjacent stochiometric planes (e.g. in the middle of the van der Waals gap) connecting two opposite corners of the in-plane projection of the hexagonal unit cell. We also note mirror symmetry from dihedral vertical planes containing the violet dashed lines in figure 1.3-b. Besides, the crystal is invariant under two S_6 operations, namely the clockwise and anticlockwise rotations of 60° along C_6 axis followed by a σ_h operation.

1.3.3 Symmetry group of the wave vector

For the two types of monolayers (trigonal prismatic or octahedral configuration of the metal atom), equation 6.4 defines $\vec{\boldsymbol{a}_1}$ and $\vec{\boldsymbol{a}_2}$ as the primitive vectors of the real space lattice depicted in figure 6.2-a, projected onto the Cartesian basis vectors $\hat{x}$ and $\hat{y}$. Equation 6.4 defines also the reciprocal vectors $\vec{\boldsymbol{b}_1} = \frac{2\pi}{a^2}\left(\vec{\boldsymbol{a}_2} \wedge \vec{\boldsymbol{k}}\right)$ and $\vec{\boldsymbol{b}_2} = \frac{2\pi}{a^2}\left(\vec{\boldsymbol{k}} \wedge \vec{\boldsymbol{a}_1}\right)$ where $\vec{\boldsymbol{k}} = \hat{x} \wedge \hat{y}$ is a unit vector oriented in the out-of-plane direction.

$$\vec{\boldsymbol{a}_1} = \frac{a}{2}(\sqrt{3}\hat{x} + \hat{y}) \quad \vec{\boldsymbol{a}_2} = \frac{a}{2}(-\sqrt{3}\hat{x} + \hat{y}) \quad \vec{\boldsymbol{b}_1} = \frac{2\pi}{a}(\frac{\sqrt{3}}{3}\hat{x} + \hat{y}) \quad \vec{\boldsymbol{b}_2} = \frac{2\pi}{a}(-\frac{\sqrt{3}}{3}\hat{x} + \hat{y}) \tag{1.1}$$

Figure 6.2-b shows the reciprocal space including the high symmetry points K, K', Γ and M ; the high symmetry lines T, T' and Σ as well as the points Q and Q' located half-way along the $\Gamma - K$ and $\Gamma - K'$ lines, respectively. The six corners of the first Brillouin zone lie at the inequivalent K and K' points due to strong spin-orbit coupling. The two groups of equivalent corners are related to each other by reciprocal lattice vectors. The unit cell contains one metal atom and two chalcogen atoms.

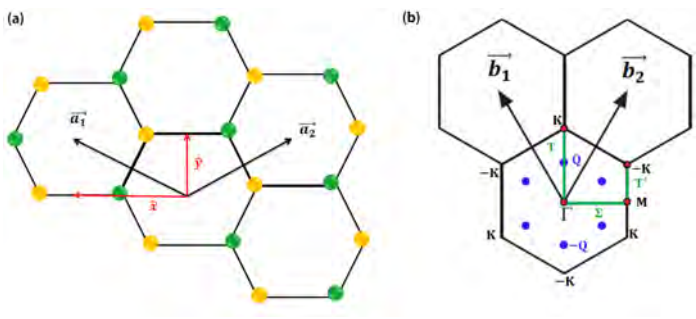

Figure 1.4: a) Real and b) reciprocal space representation of a monolayer TMDC.

	Space group	Γ	$K(K')$
N odd	D^1_{3h}	D^1_{3h}	C^1_{3h}
N even	D^3_{3d}	D^3_{3d}	D^2_3
Bulk	D^4_{6h}	D^4_{6h}	D^4_{3h}

Table 1.1: Space groups and wave vector symmetry elements for 2H TMDCs. Adapted from [27].

The D^1_{3h} and D^3_{3d} space groups, representing respectively odd and even number of few layer TMDCs with trigonal prismatic coordination of the metal atoms, imply different symmetry elements for the wave vector at the high symmetry points or directions in the reciprocal space. Table 1.1 summarizes the wave-vector symmetry properties at relevant high symmetry points and axes of the first Brillouin Zone (BZ), including bulk TMDCs (infinite number of layers) for which inversion symmetry is prevalent.

1.3.4 Consequence of the Kramers theorem on the TMDC band structure

The knowledge of a system's quantum state at a given time t combined with the deterministic laws of physics are sufficient to determine the quantum state of the system. If the wave function $\psi(r,t)$ specifies the time evolution of the state $\psi(r,0)$, then $\psi(r,-t)$ is called the time-reversed conjugate of $\psi(r,t)$. The time-reversed conjugate quantum state is achieved by running the system backwards in time, therefore reversing all the velocities of the system. In the following, the time reversal operation $t \rightarrow -t$ is denoted by the operator $\hat{T}$. We also introduce the inversion operation $r \rightarrow -r$ denoted by the operator $\hat{I}$. A crystal is inversion symmetric when the operator $\hat{I}$ leaves it unchanged. When the Hamiltonian commutes with the spin (e.g. in systems without spin-orbit interaction), the same Schrödinger equation is solved for both spins, leading to spin-degenerate quantum states whether or not there is spatial inversion symmetry. On the other hand, when the spin must be taken into account, a spin degeneracy lifting occurs only if the system is not inversion-symmetric. Indeed, we remind that the time-reversal operation changes both the sign of the wave-vector and the spin of a quantum state, so that $\hat{T}\psi(r,k,t,\uparrow) = \psi(r,-k,-t,\downarrow)$. Since the Hamiltonian and time-reversal operators commute, we end up with:

$$E(k,\uparrow) = E(-k,\downarrow) \quad \text{and} \quad E(k,\downarrow) = E(-k,\uparrow) \tag{1.2}$$

In addition, if the system is inversion-symmetric, we have :

$$E(k,\uparrow) = E(-k,\uparrow) \quad \text{and} \quad E(k,\downarrow) = E(-k,\downarrow) \tag{1.3}$$

The combination of equations 1.2 and 1.3 leads to

$$E(k,\downarrow) = E(k,\uparrow) \tag{1.4}$$

making $\psi(r, k, t, \uparrow)$ and $\psi(r, k, t, \downarrow)$ spin-degenerate quantum states. This demonstration is known as the Kramer degeneracy theorem.

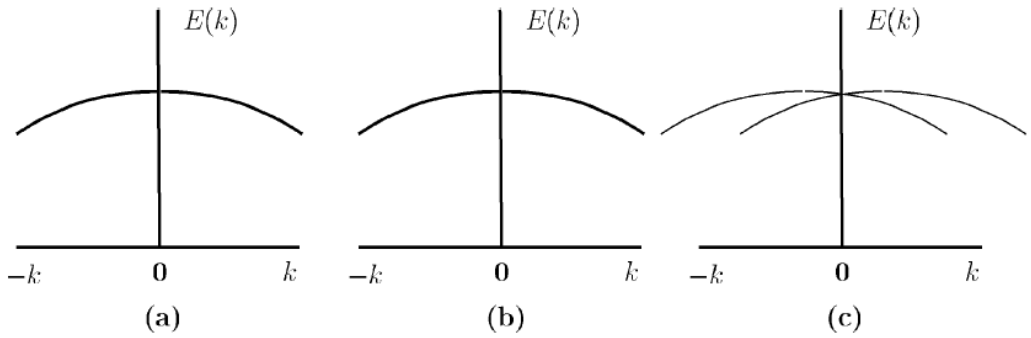

Figure 1.5: Schematic example of Kramers degeneracy in a crystal in the case **(a)** no spin-orbit interaction where each level is doubly degenerate, **(b)** both spin-orbit interaction and inversion symmetry are present leading to two-fold degenerate quantum states, **(c)** spin-orbit interaction and no inversion symmetry leading to non-degenerate quantum states. Adapted from [57].

However, if there is no inversion symmetry, only equation 1.2 remains fulfilled leading to spin degeneracy lifting (except in some particular high symmetry points of the 1st BZ) as shown in figure 1.5-c.

1.4 Electronic band-structure

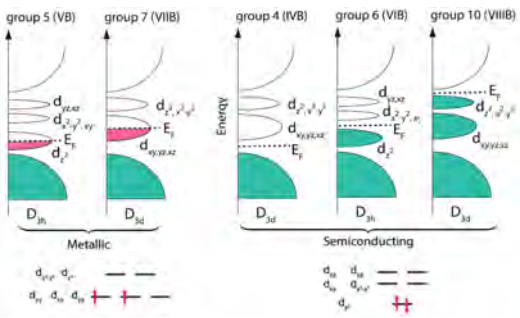

Figure 1.6: Schematic density of states of bulk layered TMDCs from different groups of the Periodic Table. Adapted from[33].

The electronic band-structure of bulk TMDCs strongly depends on the coordination geometry and the number of electrons occupying the d-orbitals of the transition atom.

In systems with octahedral coordination (belonging to the D_{3d} symmetry group), two degenerate bands are formed: the e_g band (originating from the d_{z^2} and $d_{x^2-y^2}$ atomic orbitals) and the t_{2g} band (originating from the d_{xy}, d_{yz} and d_{xz} atomic orbitals) which can together accommodate up to 6 d-electrons. In the trigonal prismatic configuration (belonging to the D_{3h} symmetry group), the hybridation of atomic d-orbitals produces three

bands named: A_1 (d_{z^2}) ; E ($d_{x^2-y^2} + d_{xy}$) and $E'(d_{yz} + d_{xz})$ [29, 9].

The different electronic properties of TMDCs result from the progressive filling of these bands. If the highest occupied band is partially filled, the material is a metal (group 5 and 7 in figure 1.6). On the other hand, when the lowest energy band is fully occupied and the highest energy one is left empty, the material shows semi-conducting properties (group 4, 6 and 10 in figure 1.6). The impact of the nature of the chalcogen atoms on the electronic properties of TMDCs is minor (the d-bands broaden with a concomitant decrease of the energy gap) compared to the effect of the transition metal atomic species. In the following, we will focus our discussion on WSe_2 band-structure and provide indication when a qualitative comparison is not appropriate to other TMDCs of the same group.

1.4.1 Mono-layer WSe_2

A precise and complete description of the electronic band-structure of monolayer WSe_2 requires rigorous density functional theory (DFT) calculations. This approach, detailed in [8], is out of the scope of this thesis: we focus below our discussion on the main results only, considering the highest-energy valence band (VB) and the lowest-energy conduction band (CB). The conduction band minimum (CBM) and the valence band maximum (VBM) are both located at the 6 corners of the first Brillouin zone (FBZ) **K** and **K'**, thereby forming a direct band-gap. Although the quantum states at the 1st BZ corners have the same energy, they are not identical since a pair of points **K** and **K'** is not related through a reciprocal lattice vector. The band extrema are energetically degenerate so that the valley index (also referred to as the pseudospin) constitutes an additional degree of freedom with respect to the trivial spin. It is worth reminding here that the two groups of **K** and **K'** points transform into each other under the time reversal operation.

The electronic quantum states must be described by considering the spin-orbit interaction originating from the d-orbitals of the metal atoms [15]. We start our discussion by noting that the symmetry element $\boldsymbol{\sigma}_h$ imposes a Bloch state and its mirror reflection to have the same energy. The operation, $\boldsymbol{\sigma}_h$ transforms a spin in the in-plane direction into its opposite, while the out-of-plane spin direction remains unchanged (see figure 1.7). As a consequence, only the out-of-plane spin degeneracy can be lifted by the spin-orbit coupling and the spin expectation values will

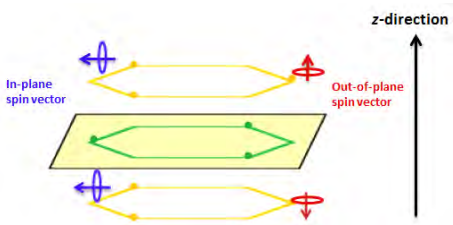

Figure 1.7: Spin states under $\boldsymbol{\sigma}_h$ symmetry operation.

be either "**up**" or "**down**". On the other hand, the time reversal symmetry dictates an identical magnitude but opposite sign of the spin at **K** and **K'** points [42, 43]. This important property is sketched in figure 6.3 where the spin splitting of both the VB and CB extrema are interchanged at **K** and **K'** points. The spin-splitting is larger in the VB compared to the CB at **K**-points for tungsten-based TMDCs and change sign for their molybdenum-based counterparts. The spin-orbit interaction introduces a coupling between the spin and valley degree of freedom, so that the spin state is intimately related to the valley index. In agreement with equation 1.2, this coupling is inherent to monolayer and odd-number of layers TMDCs, which lack i as opposed to their even-number of layer counterparts.

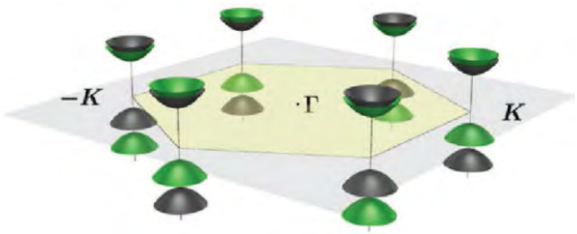

Figure 1.8: Out-of-plane spin splitting with opposite signs at the **K** and **K'** points of the 1st BZ in mono-layer WSe_2. Adapted from [9].

In the following, K_c and K_v denote the quantum states at the CBM and the VBM respectively. We also note that the CB has six local minima at the low symmetry **Q** points, while the VB has a local maximum at the **Γ** point, which will be referred as to Q_c and $\mathbf{\Gamma}_v$ quantum states, respectively. These states, which are energetically close to K_c and K_v, become the global CBM and VBM in the case of mutli-layer WSe_2. The **Γ**, **K** and **Q** points of the 1st BZ are invariant under C_3 operation, so that the dispersion relation in the neighborhood of these points show a three-fold rotational symmetry named after "trigonal warping" (not shown in figure 6.3).

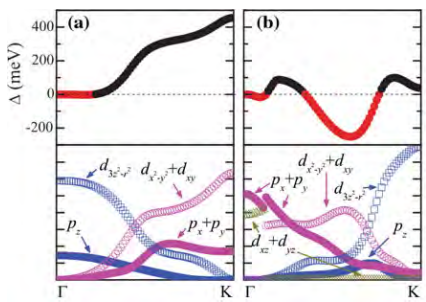

(c)

Band edge	Majority orbitals	Minority orbitals
K_c	$M(d_{z^2})$	$X(p_x, p_y)$
K_v	$M(d_{x^2-y^2}, d_{xy})$	$X(p_x, p_y)$
Q_c	$M(d_{x^2-y^2}, d_{xy})$	$M(d_{z^2}), X(p_x, p_y, p_z)$
Q_v	$M(d_{z^2})$	$X(p_z)$

Figure 1.9: (a),(b) orbitally resolved contributions of Se and W atoms in the band-structure of mono-layer WSe_2 (c) Qualitative contribution of atomic orbitals to the Bloch states at high symmetry points of the FBZ. See the main text for the nomenclature. Adapted from [15].

First principles calculations predict that the K_c and K_v quantum states are predominately from the transition metal $T(d_{x^2-y^2}, d_{xy}, d_{z^2})$ orbitals as well as chalcogen $X(p_x, p_y)$ orbitals. On the other hand, the contribution from $X(p_z)$ orbitals become significant in the Q_c and $\mathbf{\Gamma}_v$ states. Anticipating section 1.4.2, the non-negligible $X(P_z)$ orbital overlap in multilayer WSe_2 leads to appreciable energy changes of Q_c and $\mathbf{\Gamma}_v$ which triggers a transition from a direct band-gap to an indirect one.
The main difference between the molybdenum- and tungsten- based compounds is the larger splitting of the valence band for the latter, which is due to the larger spin-orbit coupling strength [37]. The splitting typically ranges from 150 meV to 450 meV for light molybdenum- and heavy tungsten-based TMDCs, respectively. The table 1.10 illustrates the values of the splitting in the VB and CB for different mono-layers obtained from first-principles calculations [41, 9].

	Δ^{v}_{SOC} (eV)					Δ^{c}_{SOC} (eV)
	GGA			HSE	GW	GGA
MoS_2	0.148,	0.146		0.193	0.164	−0.003
WS_2	0.430,	0.426,	0.425	0.521	0.456	0.029
$MoSe_2$	0.184,	0.183		0.261	0.212	−0.021
WSe_2	0.466,	0.456,	0.461	0.586	0.501	0.036

Figure 1.10: spin-orbit coupling (SOC) splitting at K_v and K_c in TMDCs mono-layers from first-principles calculations. Adapted from [40].

Experimental evidence for such a giant spin-orbit coupling can be proved by performing direct measurements of the band structure using Angle-Resolved Photo-Emission Spectroscopy (ARPES), as shown in figure 1.11-a) for a single-layer WSe_2 [18]. Two spin-resolved traces are clearly identified near the point K. In addition, the photo-luminescence quantum yield (QY), shows a dramatic enhancement between bulk (dark) and monolayer (bright) confirming the transition from indirect-gap in bulk crystal to a direct-gap in monolayers [44]. Two Photo-luminescence (PL) peaks, attributed to A and B excitons, correspond to an energy separation in agreement with the VB spin splitting at points $\pm K$ of the first BZ (see figure 1.11-a). Besides, Raman measurements shows distinct spectra between monolayer TMDCs and its few-layer counterpart, where there are four Raman-active modes, namely A_{1g}, E_{1g}, E^1_{2g} and E^2_{2g} modes, only 2 modes are present in measurements which are A_{1g} and E^1_{2g} (see figure 1.11-b).

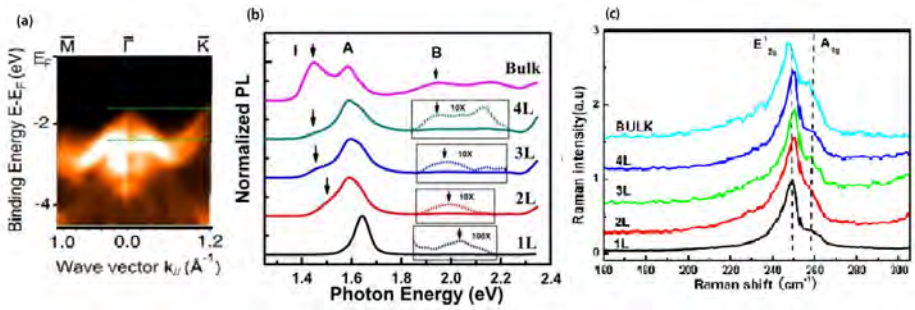

Figure 1.11: (a)The experimental monolayer WSe_2 band structure the top of the valence band along the high symmetry lines [18], (b) Normalized PL spectra by the intensity of peak A of thin layers of WSe_2 for N= 1-4 and bulk, (c) Raman spectra of WSe_2 for N=1-4 and bulk [45].

1.4.2 bi-layer WSe_2

First-principle calculations show that bi-layer TMDCs, where the transition metal atoms have trigonal prismatic coordination, is the most stable atomic structure [49]. The unit cell of bilayer WSe_2 is the double of that of a monolayer, where the upper and lower layers are in-plane rotated by 180° with respect to each other. This system is point inversion symmetric and therefore, even in the presence of SOC, the electronic states are spin-degenerate (see section 1.3.4). Actually, the two layers interact only weakly via van der Waals forces and the electronic properties of bilayer-TMDCs resembles, at first sight, much like those of two independent monolayers rotated 180° to each other. This symmetry operation switches the two valleys K and K' (see figure 6.4) but leaves the spin unchanged, so that the valley-dependent physical properties naturally average to zero (valley Hall effect, valley circular dichroism) while the spin-dependent effects add up (spin Hall effect and spin optical dichroism). In bilayer WSe_2, the sign of the spin-splitting is intimately related to the valley as well as the layer index, which is a new degree of freedom for the electronic states (e.g. the electron wave-function for bilayer WSe_2 can be regarded as a linear superposition of two wave-functions fully localized either on the top or the bottom layers). Considering now the interaction between the two stochiometric planes, we note that interlayer hopping does not naturally change the spin and crystal momentum of charged particles. Therefore, such a hopping is allowed only if the electron spin is simultaneously changed with an associated spin splitting energy cost [43]. In WSe_2, the SOC is particularly strong and the spin splitting is much larger than the hopping energy, so that inter-layer hopping is effectively suppressed. It follows that spin-up(down) quantum states are localized either in the top(bottom) or in the bottom(top) layer depending on the valley index, which sets a spin-layer locking of the degrees of freedom. As

anticipated above, the valley physics at points K and K' is similar to the one of two decoupled monolayers. Nevertheless, it is important to stress that a perpendicular electric field breaks inversion symmetry [26] and restores the valley-dependent properties. For instance, references [16, 13] report inversion symmetry breaking in bi-layer MoS_2 and WSe_2 by applying an external perpendicular electrical field, controlled by a gate voltage in the transistor configuration.

The first-principle band-structure calculations for bilayer TMDCs are much sensitive

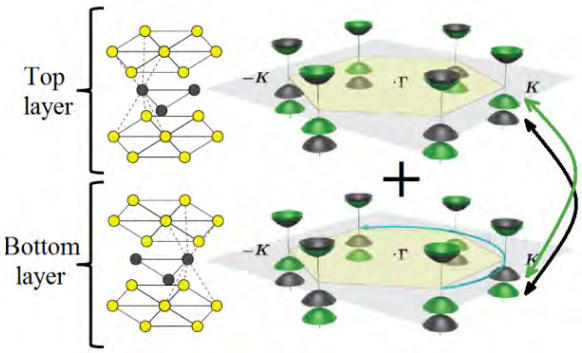

Figure 1.12: The electronic properties of 2H-bilayer TMDCs resemble those of two monolayer TMDCs in-plane rotated of 180° to each other. In the reciprocal space, the band edges at K and K' points of a bilayer TMDCs 1st BZ is merely a superposition of the band edge of each monolayer, leading to spin-degenerate states as required for point inversion symmetry systems.

to the lattice and interlayer distances, leading to quite different band edges and band-gaps [50]. A review of such calculations is out of the scope of this thesis [51, 52], but we stress the presence of an indirect band-gap as the most important feature. The transition from direct band-gap at K-points in monolayer WSe_2 to indirect band-gap in bilayer finds its origin in interlayer hopping [40]. In the presence of spin-orbit coupling, the valence band edge at K-points is not much affected due to the spin-layer coupling effect. However, the valence and conduction band edges at Γ and Q-points respectively are particularly affected. Indeed, the Bloch states at Q_c and Γ_v include a contribution of $X(p_z)$ orbitals with strong overlap, since the chalcogen atoms are the nearest neighbors at the van der Waals gap between the top and bottom layers. For comparison, even when the spin-orbit coupling is turned of, the quantum states defining K_v barely change their energy from mono to bilayer WSe_2, since these states are mainly derived from the weakly overlapping transition metal orbitals [38].

1.4.3 Band gap from mono-layer to bulk TMDCs

Monolayer WSe_2 and other group VI TMDCs have a direct band gap, which turn into indirect as new successive layers are added (bilayers, trilayers to bulk TMDCs). This transition was first reported in reference [34]. The band gap transition to an indirect one at the bilayer, as well as its evolution with increasing number of layers is illustrated in figure 1.13 for WSe_2 where the SOC is taken into account.

The electronic band gap is defined as the energy difference between the CBM and the

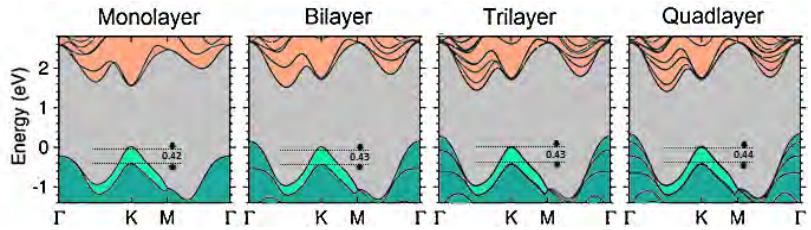

Figure 1.13: Band structure of mono-, bi-, tri- and quad-layer WSe_2 obtained from DFT calculations including SOC. The horizontal dotted lines in dictates the spin-split bands, which represents the inter-layer hopping strength. Adapted from [37]

VBM. It can be experimentally determined using transport or optical measurements. However, the value obtained from these two different methods differs due to the excitonic effect present in the optical process (see figure 1.14a). Transport experiments is sensitive to the single-particle excitations and provide a rather direct measurement of the band-gap. On the other hand, in experiments involving optical transitions, the absorption of a photon simultaneously creates an electron and a hole in the CB and VB respectively. These quasi-particles interact through the Coulomb interaction and form an exciton. The minimum energy required to create an exciton is defined as the optical band gap E_{Opt} as illustrated in figure 1.14a for group VI TMDCs. The energy difference between the electronic and optical band gaps corresponds to the binding energy of the exciton corresponding to the Coulomb interaction strength. Optical band gaps of group VI TMDCs monolayers have been determined from PL measurements (see figure 1.14b . Although the substrate and the dielectric environment may affect weakly the exact bad gap value, they reside into the visible frequency range [6].

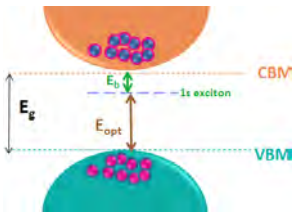

(a)

	Gap	
MoS_2	1.83,	1.90
WS_2	1.95	
$MoSe_2$	1.66	
WSe_2	1.64	

(b)

Figure 1.14: (a) Illustration of optical and electronic band-gap. (b) Optical band gap values for group VI TMDCs. Adapted from [28]

1.4.4 Few-layer WSe_2

We remind that monolayer and bilayer TMDCs belong to the space group D^1_{3h} and

D_{3d}^3 respectively, where the latter includes inversion symmetry [9]. The minima of the conduction bands are not located at the K/K' points, but rather at the Q/Q' and Γ points with quadratic dispersion relation in their neighborhood as shown in figure 6.5. The C_3 rotational symmetry dictates the threefold Q-valley degeneracy. For even-layer TMDCs, the Q and Q' valleys are related by both time reversal and inversion symmetries, where the Kramer degeneracy theorem applies [55]. On the other hand, the inversion symmetry is broken in odd-layers so that all the sub-bands at each Q-valleys are spin non-degenerate. The spin-valley locking properties of monolayer and bilayer TMDCs can be extended to few-layer TMDCs with odd and even number of layers respectively, considering however the Q valleys instead of K valleys [56].

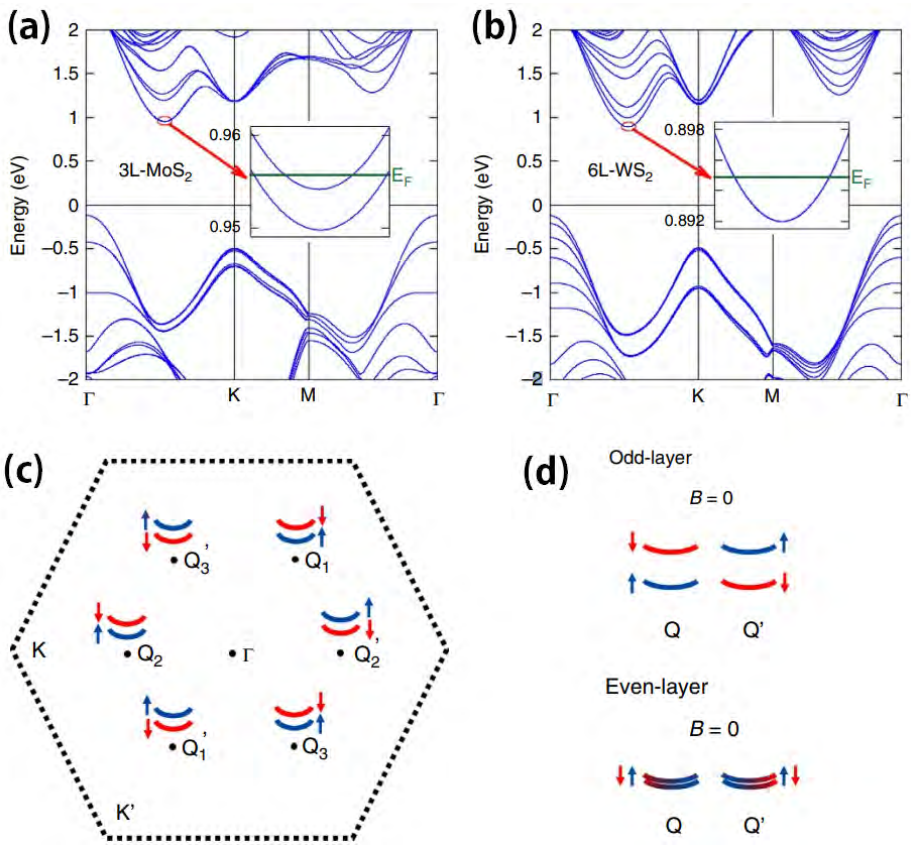

Figure 1.15: (a),(b) calculated band structure of 3L- MoS_2, and 6L-WS_2 .(b) High symmetry point representation in the reciprocal space with the red and the blue color refer to the spin-down and the spin-up respectively. (d) Schematic diagrams for the Bloch bands. Adapted from [56].

Chapter 2

Electronic transport

Contents

2.1 Classical approach to charge transport **15**

2.1.1 The Drude model of conductivity 16

2.1.2 Boltzmann transport equation without magnetic field . . . 17

2.1.3 Electrical conductivity in the presence of a magnetic field 21

2.1.4 Boltzmann transport equation in the presence of a magnetic field 26

2.2 Transport phenomena in quantizing Magnetic **30**

2.2.1 Landau levels 31

2.2.2 Landau levels broadening 34

2.2.3 Shubnikov-de Haas oscillations 36

2.2.4 Zeeman energy 39

2.2.5 Standard analysis of the Shubnikov-de Haas oscillations . 41

2.1 Classical approach to charge transport

Electrical transport involves the motion of charges (the current) under the influence of electric and/or magnetic fields. In non-ballistic systems, the charge carriers are, on one hand, accelerated by the driving fields and, on the other hand, scattered and/or slowed down when colliding onto the medium's defects, phonons or between themselves. These opposite interactions lead to a constant mean velocity of the charge carriers referred to as the drift velocity v_d. The classical treatment of conduction relies on the Drude model, which introduces a mean scattering time to take into account the diffusion processes. This concept can also be used within a statistical approach of a charged particles gas, named after the relaxation time approximation in the Boltzmann transport equation. The Drude model and its statistical counterpart will be developed in the absence of magnetic field in the first two sections. When a magnetic field is included, the dynamics of the charged particles change as well as the resulting conductivity. This problem was first tackled by Edwin Herbert Hall[1] **(1855-1938)** who found out that a homogeneous magnetic field normal to the direction of the current flow results in a voltage V_H between two points with their connecting line normal to the magnetic field and normal to the current flow. The Hall effect and the derivation of the magneto-conductivity tensor are described in the third section,

[1] An American physicist who discovered the eponymous Hall effect

while the statistical approach of a gas of charged particles in the presence of both electric and magnetic fields is derived in the last section.

2.1.1 The Drude model of conductivity

Let us consider the system in figure 2.1, where a voltage is applied between two ends of a material, say a metal or a semi-conductor. In the absence of electric field ($\mathbf{E} = 0$), the charge carriers move in all directions: their motion is random as they bounce independently on the materials' defects, its boundaries or between themselves. We assume that the direction of motion after scattering is completely independent of the motion before scattering. For a very large number of charge carriers, the net current averages to zero. On the other hand, when the electric field $\mathbf{E}$ is non-zero, the charge carriers drift along the direction of the electric field. The random motion does not disappear but its time average leads to a linear trajectory with constant drift velocity $\mathbf{v}_d$. We define the current density $\mathbf{j}$ as the product of the carrier density $\mathbf{n}$ by the drift velocity $\mathbf{v_d}$ and the elementary charge q, which can be either negative or positive for electrons or holes, respectively.

$$\mathbf{j} = en \cdot \mathbf{v}_d \tag{2.1}$$

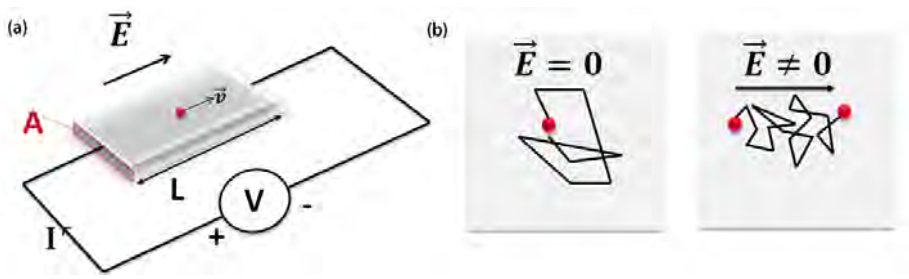

Figure 2.1: (a) Sketch of a material submitted to an external electric field. (b) Random motion of charge carriers in the absence of electric field : the net current is null. (c) Drift motion of the charge carriers in the presence of an external electric field.

The electrical conductance probes the global scattering of charge carriers taking place at a microscopic level in the material. Neglecting the spin, we distinguish different sources of scattering such as crystal defects, charged impurities, lattice vibrations (phonons) or scattering via electron-electron interaction to cite only a few examples. The mean scattering time τ is defined as the average time in between two scattering events. In the stationary regime, the drift velocity divided by the mean scattering time defines an acceleration which, multiplied by the effective mass of a charge carrier, is equivalent to a force opposite to the one produced by the external electric field. We can define the mobility μ of a material as the ratio between the drift velocity

and the electric field and, by applying the static Newton's law (the net acceleration of the charge carriers is null, for constant drift velocity), we show that the mobility alternatively relates the mean scattering time, the effective mass and the charge of the carriers:

$$\underbrace{q.\mathbf{E}}_{\mathbf{F_c}}\underbrace{-m^*\mathbf{v}_d/\tau}_{\mathbf{F_{drift}}} = 0 \Leftrightarrow \mu = \frac{|\mathbf{v_d}|}{|\mathbf{E}|} = \frac{q\tau}{m^*} \tag{2.2}$$

The mobility is proportional to the mean free time and inversely proportional to the charge carrier mass. Combining equations 6.5 and 6.6, the current density can be written as a function of the electric field where the proportionality factor defines the conductivity σ of the material. In the absence of magnetic field, the resistivity is the inverse of the conductivty:

$$\sigma = \frac{q^2\tau n}{m^*} = nq\mu \tag{2.3}$$

$$\rho = \frac{m^*}{q^2\tau n} = 1/(nq\mu) \tag{2.4}$$

To summarize, the classical Drude model describes the dynamics of a charged particle in a homogeneously disordered medium and under the influence of an external electric field. The model assumes that all the conduction electrons behave in a similar way, so that the macroscopic observables (conductivity, current...) are obtained by multiplying the single-particle dynamics by the charge carrier density. This simple approach of the material's conductivity provides the starting point for a more complex (semi-classical) theory taking into account the insights of statistical physics where the Fermi-Dirac distribution function is introduced.

2.1.2 Boltzmann transport equation without magnetic field

The driving force of the external electric field and the dissipative effect of the scattering of the charge carriers are two competing mechanisms. This section details the Boltzmann equation which describes the interplay between them. This theory is semi-classical since the charge carriers are treated as point particles but the Fermi-Dirac statistics resulting from the Pauli exclusion principle is also introduced. Let us consider the time evolution of the total number of charged particles N in a phase-space volume $\mathbf{r}^3.\mathbf{p}^3$. We now introduce the distribution function of the system $f_{(\mathbf{r},\mathbf{p},t)}$, in other words the probability density of finding a particle at position $\mathbf{r}$ with momentum $\mathbf{p}$ at time t, so that $N_{(t)} = \int_{\mathbf{p}}\int_{\mathbf{r}} f_{(\mathbf{r},\mathbf{p},t)} d^3\mathbf{p}.d^3\mathbf{r}$. To ease the derivation of the Boltzmann equation, we now restrict our analysis to a one-dimensional system, say in the x-direction, so that a given particle state is provided only by the knowledge of x and p_x. The evolution of the distribution function can be separated into two contributions

: $df_{(x,p_x,t)} = \left(df_{(x,p_x,t)}\right)_{ext} + \left(df_{(x,p_x,t)}\right)_{int}$ where $\left(df_{(x,p_x,t)}\right)_{ext}$ is related to the effect of external forces whereas $\left(df_{(x,p_x,t)}\right)_{int}$ represents the scattering contribution. In the following, we derive an explicit expression for $\left(df_{(x,p_x,t)}\right)_{ext}$ by expanding $f_{(x,p_x,t)}$ to the first order in momentum and space coordinates (we assume the distribution function does not depend explicitly with time, so that its partial derivative with respect to time is dropped off):

$$\begin{aligned} df^{ext}_{(x,p_x,t)} &= \frac{\partial f_{(x,p_x,t)}}{\partial x}.dx + \frac{\partial f_{(x,p_x,t)}}{\partial p_x} dp_x \\ &= \left(\frac{\partial f_{(x,p_x,t)}}{\partial x}\frac{p_x}{m^*} + \frac{\partial f_{(x,p_x,t)}}{\partial p_x} qE_x\right) dt, \end{aligned} \tag{2.5}$$

where $\frac{dx}{dt} = \frac{p_x}{m^*}$ and $\frac{dp_x}{dt} = qE_x$. The evolution of the distribution function due to internal forces is difficult to model, as it requires a microscopic description for the scattering processes. Nevertheless, this term is usually approximated by the so called relaxation time ansatz, which assumes an exponential return to equilibrium distribution function $f^{int}_{0(x,p_x)}$ with characteristic time set by the mean scattering time τ.

$$f^{int}_{(x,p_x,t)} = f_{0(x,p_x)} + \left[f_{(x,p_x,t=0)} - f_{0(x,p_x)}\right] \times \exp\left(-t/\tau\right) \Rightarrow \frac{df^{int}_{(x,p_x,t)}}{dt} = -\frac{f_{0(x,p_x,t)} - f_{0(x,p_x,t)}}{\tau} \tag{2.6}$$

Combining equations 2.5 and 2.6, the evolution of the 1D-distribution function is

$$df_{(x,p_x,t)} = df^{ext}_{(x,p_x,t)} + d^{int} f_{(x,p_x,t)} = \left(\frac{\partial f_{(x,p_x,t)}}{\partial x}\frac{p_x}{m^*} + \frac{\partial f_{(x,p_x,t)}}{\partial p_x} qE_x - \frac{f_{(x,p_x,t)} - f_{0(x,p_x)}}{\tau}\right).dt \tag{2.7}$$

Generalizing to the 6D phase-space, the Boltzmann equation using the relaxation time ansatz reads:

$$\frac{df_{(\mathbf{r},\mathbf{p},t)}}{dt} = \nabla_{\mathbf{p}}\left(f_{(\mathbf{r},\mathbf{p},t)}\right) q\mathbf{E} + \nabla_{\mathbf{r}}\left(f_{(\mathbf{r},\mathbf{p},t)}\right)\frac{\mathbf{p}}{m^*} - \frac{f_{(\mathbf{r},\mathbf{p},t)} - f_{0(r,p)}}{\tau} \tag{2.8}$$

The stationary solution of the Boltzmann equation is obtained by dropping off the time derivative $\frac{df_{(\mathbf{r},\mathbf{p},t)}}{dt} \equiv 0$. Additionally and for simplicity, we also assume an homogeneous system so that $\nabla_{\mathbf{r}}\left(f_{(\mathbf{r},\mathbf{p},t)}\right) = 0$. Setting the electric field $\mathbf{E} = E_x\hat{x}$ in the

x-direction, the Boltzmann equation simplifies to :

$$\underbrace{\nabla_{\mathbf{p}}\left(f(\mathbf{r},\mathbf{p},t)\right)\mathbf{F}}_{\frac{\partial f_{0(\mathbf{r},\mathbf{p})}}{\partial p_x}qE_x}+\underbrace{\nabla_{\mathbf{r}}\left(f(\mathbf{r},\mathbf{p},t)\right)\frac{\mathbf{p}}{m^*}}_{=0}=\frac{1}{\tau}\left(\underbrace{f(\mathbf{r},\mathbf{p},t)}_{f(\mathbf{r},\mathbf{p},t)}-\underbrace{f_0(\mathbf{r},\mathbf{p})}_{f_{0(\mathbf{r},\mathbf{p})}}\right)$$

$$\frac{\partial f_0(\mathbf{r},\mathbf{p})}{\partial p_x}qE_x=\frac{1}{\tau}\left(f(\mathbf{r},\mathbf{p},t)-f_{0(\mathbf{r},\mathbf{p})}\right)$$

$$f(\mathbf{r},\mathbf{p},t)=f_0(\mathbf{r},\mathbf{p})+qE_x\tau\times\frac{\partial f_0(\mathbf{r},\mathbf{p})}{\partial p_x} \tag{2.9}$$

In the following, the equilibrium distribution function will be replaced by the Fermi-Dirac function $f_0(\mathbf{r},\mathbf{p}) = \frac{2}{h^3}\frac{1}{\exp\left[\left(\epsilon_{(\mathbf{p})}-\epsilon_F\right)/k_BT\right]+1}$ as shown in figure 2.2. The pre-factor $\frac{2}{h^3}$ corresponds to the elementary quantum volume in 6D-space including the spin degeneracy. Looking at equation 2.9, the stationary distribution function resulting from an external field E_x and including the effect of scattering can be represented by a Fermi distribution shifted by $qE_x\tau$ from the equilibrium as shown in figure 2.3.

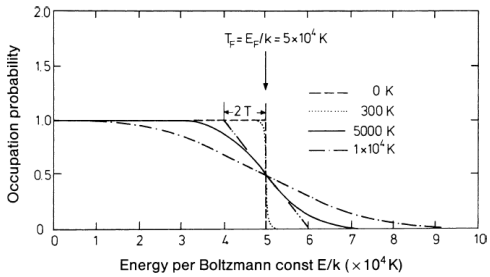

Figure 2.2: Fermi distribution at different temperatures. Adapted from [61]

The mean current density at position $\mathbf{r}$ and time t is provided by integrating over all possible states (here defined by the vector momentum) the distribution function by the velocity. Looking at the current in the x-direction only, we end up with the following expressions

$$\begin{aligned}
\langle\mathbf{j}(\mathbf{r},\mathbf{t})\rangle &= q\times\int_{\mathbf{p}} f(\mathbf{r},\mathbf{p},t)\times\frac{\mathbf{p}}{m^*}\times d^3p,\\
\langle j^x(\mathbf{r},t)\rangle &= \langle\mathbf{j}(\mathbf{r},\mathbf{t})\rangle.\hat{x} = q\times\int_{\mathbf{p}} f(\mathbf{r},\mathbf{p},t)\times\frac{p_x}{m^*}\times d^3p,\\
\langle j^x(\mathbf{r},t)\rangle &= q\times\int_{\mathbf{p}} f_0(\mathbf{r},\mathbf{p})+qE_x\tau\times\frac{\partial f_0(\mathbf{r},\mathbf{p})}{\partial p_x}\times\frac{p_x}{m^*}\times d^3p,\\
\langle j^x(\mathbf{r},t)\rangle &= \frac{q^2E_x}{m^*}\times\int_{\mathbf{p}}\tau\times\frac{\partial f_0(\mathbf{r},\mathbf{p})}{\partial p_x}\times p_x\times d^3p,
\end{aligned}$$

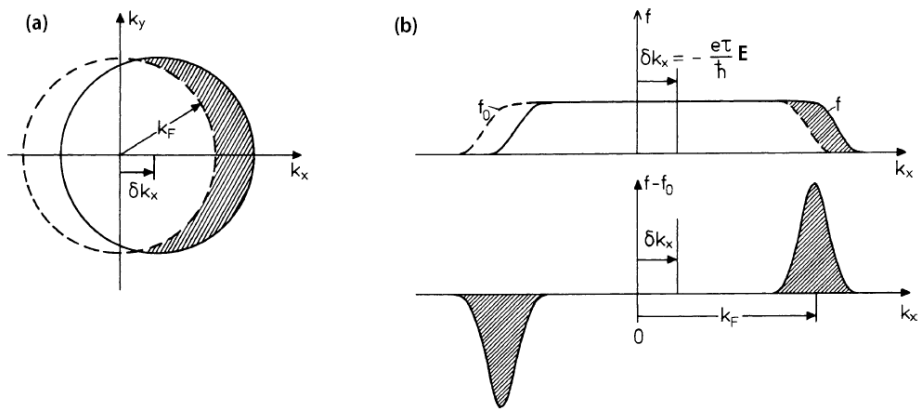

Figure 2.3: The effect of a constant electric field $\mathbf{E} = E_x\hat{x}$ on the $\mathbf{k}$-space distribution of quasi-free electrons. (a) The Fermi sphere at equilibrium is centred at zero and is displaced in the out-of-equilibrium stationary state by an amount $\delta k_x = q\tau E_x/\hbar$. (b) The out-of-equilibrium Fermi distribution $f_{(\epsilon(k))}$ only differs from the equilibrium distribution f_0 dashed in the vicinity of the Fermi energy. Adapted from [61]

where $\int_{\mathbf{p}} f_0(\mathbf{r},\mathbf{p})d^3p = 0$ since the Fermi-Dirac distribution function at equilibrium is isotropic. The mean scattering time τ is, in general, a function of momentum and must remains inside the integral. In the following, we change the integration variable from momentum to energy ($d^3p = 4\pi p^2 dp = 4\pi\left(\sqrt{2m^*\epsilon}\right)^2 \frac{d\epsilon}{\sqrt{2m^*\epsilon}}$ with $\epsilon = \mathbf{p}^2/2m^*$) and make use of the equality $\frac{\partial\epsilon}{\partial p_x} = \frac{p_x}{m^*}$:

$$\begin{aligned}
\langle j^x(\mathbf{r},t)\rangle &= \frac{q^2E_x}{m^*} \times \int_{\mathbf{p}} \tau_{(\mathbf{p})} \times \frac{\partial f_0(\mathbf{r},\mathbf{p})}{\partial\epsilon} \times \frac{\partial\epsilon}{\partial p_x} \times p_x \times d^3p, \\
\langle j^x(\mathbf{r},t)\rangle &= \frac{q^2E_x}{m^*} \times \int_{\mathbf{p}} \tau_{(\mathbf{p})} \times \frac{\partial f_0(\mathbf{r},\mathbf{p})}{\partial\epsilon} \times p_x^2 \times d^3p, \\
\langle j^x(\mathbf{r},t)\rangle &= \frac{q^2E_x}{3m^*} \times \int_{\epsilon} \tau_{(\epsilon)} \times \frac{\partial f_0(\mathbf{r},\mathbf{p})}{\partial\epsilon} \times \mathbf{p}^2 \times 4\pi\sqrt{2m^*\epsilon}d\epsilon. \qquad (2.10)
\end{aligned}$$

It is worth noting that, since $\langle j^x(\mathbf{r},t)\rangle$ would be the same if we changed p_x to p_y or p_z, we replaced p_x^2 by $\mathbf{p}^2$ and divided the overall expression by 3. The derivative of the equilibrium Fermi distribution function is peaked to $-2/h^3$ at $\epsilon = \epsilon_F$ and equal zero for all other values of the energy. The integral is therefore proportional to the integrand evaluated at the Fermi energy :

$$\langle j^x(\mathbf{r},t)\rangle = -\frac{q^2E_x}{m^*}\times\frac{2}{h^3}\times\tau(\epsilon_F)\times\mathbf{p}(\epsilon_F)^2\times 4\pi\sqrt{2m^*\epsilon_F} = -\frac{8\pi q^2E_x}{3m^*h^3}\times(2m^*)^{3/2}\times\tau(\epsilon_F)\times(\epsilon_F)^{3/2} \qquad (2.11)$$

Since the Fermi energy can be expressed as a function of the carrier density $\epsilon_F = \frac{\hbar^2}{2m^*}\left(3\pi^2 n_0\right)^{2/3}$, we obtain $\langle j^x(\mathbf{r},t)\rangle = \frac{-q^2 n_0 \tau(\epsilon_F)}{m^*} E_x$ so that the conductivity $\sigma(\mathbf{r},t) = \frac{|\langle j^x(\mathbf{r},t)\rangle|}{|E_x|}$ reads :

$$\sigma = \frac{q^2 n_0 \tau_{(\epsilon_F)}}{m^*} \tag{2.12}$$

This expression for the conductivity is similar to the one obtained using the Drude model (equation 6.8), except the mean scattering time which is evaluated at the Fermi energy. This is a direct consequence of the Fermi-Dirac distribution function which indicates that only the charge carriers at the Fermi energy contribute to the transport properties. In other words, the conductivity cannot be derived from thermodynamic principles since it does not involve all the particles in the system. The resemblance of the conductivity expressions derived from the Drude model and the Boltzmann model is linked to the relaxation time approximation, where the mean scattering time τ is introduced. Although quite general, the classical and statistical treatment of the conductivity beyond the relaxation time approximation is out of the scope of this thesis and requires advanced numerical calculations.

2.1.3 Electrical conductivity in the presence of a magnetic field

We consider a three-dimensional system made of N non-interacting charged particles (of effective mass m^* and charge q) in the presence of magnetic and electric fields. The magnetic field $\mathbf{B} = B_z\hat{z}$ is applied in the z-direction so that the Lorentz force acts only in the x-y plane. An electric field $\mathbf{E} = E_x\hat{x} + E_y\hat{y}$ is either set (or established as a consequence of the Lorentz force) in the x-y plane as well. We note that the addition of a z-component to the electric field would yield the same result as in section 2.1.1, namely the conductivity in the z-direction is defined only through the mean scattering time $\sigma_{zz} = \frac{nq^2\tau}{m^*}$ since the Lorentz force does not act on charge carriers moving in the z-direction. Besides, when the charge carrier velocity is projected into the x-y components only, the Newton's law of motion gives:

$$\begin{aligned} m^*\frac{d\mathbf{v}}{dt} &= q\mathbf{F}_L - m^*\frac{\mathbf{v}}{\tau} \quad \text{with } \mathbf{F_L} = q\left(\mathbf{E} + \mathbf{v}\wedge\mathbf{B}\right) \\ m^*\frac{d\mathbf{v}}{dt} &= \left(qE_x - m^*\frac{v_x}{\tau} + qv_yB_z\right)\hat{x} - \left(qv_xB_z + m^*\frac{v_y}{\tau}\right)\hat{y} \end{aligned} \tag{2.13}$$

Here, $\mathbf{v}$ is the drift velocity (the subscript "d" has been abandoned for clarity) and the left hand side of the equation can be set to zero in the stationary regime. Equation

2.13 can be projected onto the $\hat{x}$ and $\hat{y}$ basis vectors, providing new expressions for v_x and v_y from which the current density ($\mathbf{j} = nq\mathbf{v}$) is established as follow:

$$\begin{aligned}\mathbf{j} = j_x\hat{x} + j_y\hat{y} &= \frac{n\tau q^2}{m^*}\left[\left(E_x + v_y B_z\right)\hat{x} + \left(E_y - v_x B_z\right)\hat{y}\right] \\ \mathbf{j} = j_x\hat{x} + j_y\hat{y} &= \frac{n\tau q^2}{m^*}\left[\left(E_x + \frac{j_y}{nq}B_z\right)\hat{x} + \left(E_y - \frac{j_x}{nq}B_z\right)\hat{y}\right]\end{aligned} \tag{2.14}$$

The projection of this equation onto the unit vectors $\hat{x}$ and $\hat{y}$ leads to a system of two coupled equations involving j_x and j_y. Introducing the zero-field conductivity $\sigma_0(B = 0) = \frac{nq^2\tau}{m^*}$ and the mobility $\mu = \frac{q\tau}{m^*}$, the system can be decoupled using simple algebra where each component of the current density depends linearly on the electric field components.

$$\begin{aligned} j_x &= \tfrac{\sigma_0}{1+(\mu B_z)^2}\left(E_x + \mu B_z E_y\right) \\ j_y &= \tfrac{\sigma_0}{1+(\mu B_z)^2}\left(-\mu B_z E_x + E_y\right)\end{aligned} \tag{2.15}$$

The components of the current density can be written in a compact form involving the 2D conductivity tensor $\bar{\sigma} = \begin{pmatrix}\sigma_{xx} & \sigma_{xy} \\ \sigma_{yx} & \sigma_{yy}\end{pmatrix}$ which establishes for each component of the current density, a linear relation with both components of the electric field:

$$\mathbf{j} = \bar{\sigma}\mathbf{E} \Leftrightarrow \begin{aligned} j_x &= \sigma_{xx}E_x + \sigma_{xy}E_y \\ j_y &= \sigma_{yx}E_x + \sigma_{yy}E_y\end{aligned} \tag{2.16}$$

The identification of equation 2.15 with equation 2.16 leads to explicit expressions for the components of the conductivity tensor:

$$\sigma = \begin{pmatrix} \frac{\sigma_0}{1+(\mu.B_z)^2} & \frac{\sigma_0\mu B}{1+(\mu B_z)^2} \\ -\frac{\sigma_0\mu B}{1+(\mu B_z)^2} & \frac{\sigma_0}{1+(\mu B_z)^2}\end{pmatrix} \tag{2.17}$$

Through the Lorentz force, the magnetic field leads to non-zero off-diagonal terms for the conductivity tensor. We note that $\sigma_{xx} = \sigma_{yy} = \frac{\sigma_0}{1+(\mu B_z)^2}$ and $\sigma_{xy} = -\sigma_{yx} = \frac{\sigma_0\mu B}{1+(\mu B_z)^2}$ satisfy the time-reversal symmetry. Introducing the cyclotron pulsation $\omega_c = \frac{eB_z}{m^*}$, the term μB_z can be alternatively replaced by $\omega_c\tau$. The components of the

conductivity tensor should not be confused with the longitudinal conductivity $\sigma_L \equiv j_x/E_x$ or the Hall conductivity $\sigma_H \equiv j_x/E_y$ which depend on the sample geometry. For example, let us consider a three-dimensional electron gas having the shape of a parallelogram of length L in the x-direction, of width l in the y-direction and of thickness t in the z-direction as sketched in figure 2.4. An external magnetic field is established in the z-direction while a voltage difference is set between the two ends of the system in the x-direction. No net current can flow in the y-direction (nor in the z-direction as well) and we set $j_y = 0$ in equation 2.16. Now, the current density flowing in the x-direction can be solely written either as a function of E_x (eq. 2.18) ; or as a function of E_y (eq. 2.19):

$$j_x = \sigma_{xx}\left[1 + \left(\frac{\sigma_{xy}}{\sigma_{xx}}\right)^2\right] E_x = \sigma_0 E_x \equiv \sigma_L E_x \tag{2.18}$$

$$j_y = \sigma_{xy}\left[1 + \left(\frac{\sigma_{xx}}{\sigma_{xy}}\right)^2\right] E_y = \frac{\sigma_0}{\mu B_z} E_y \equiv \sigma_H E_y \tag{2.19}$$

One note that the longitudinal conductivity σ_L is equal to the zero-field conductivity σ_0 established within the Drude model. This result is contradicted by experimental evidences, which often show a dependence with respect to the magnetic field. Actually, one must go beyond the mean relaxation time approximation to properly describe the magnetic field dependence of the magneto-conductance, at least for weak enough magnetic field and within the classical theory (see section 2.1.4).

Another important remark must be mentioned concerning the electric field established in the y-direction: this is a direct consequence of the Lorentz force. Classically, the charged carriers are deviated from their expected mean motion in the x-direction under the influence of the external electric field. The charged particles accumulate along one edge of the sample while a deficit of charges is created on the other edge. This carrier density difference along the y-direction is at the origin of the y-component of the electric field, which counterbalances the effect of the Lorentz force. Using $\mathbf{E} = -\nabla_{\mathbf{r}}(\mathbf{V})$, one can work out the Hall voltage (V_H) between the two ends in the y-direction of the system resulting from the transverse electric field :

$$V_H = -\int_0^l E_y dy = -\int_0^l \frac{\mu B}{\sigma_0} j_x dy = -\frac{\mu.B}{\sigma_0} j_x \int_0^l dy = -\frac{\mu B l j_x}{\sigma_0} \tag{2.20}$$

$$V_H = -\frac{\mu B I}{t\sigma_0} = R_H I \tag{2.21}$$

where we used $I = \int_{y=0}^{y=l} \int_{z=0}^{z=t} j_x dy dz$. The Hall voltage scales linearly with the current flowing through the system and the proportionality factor is defined as the Hall resistance $R_H = -\frac{\mu B}{t\sigma_0} = -\frac{1}{t}\frac{B}{nq}$. The Hall effect can therefore be used not only to compute the carrier density, but also to deduce the sign of the carried charge. We note that the Hall resistance reduces to $R_H = -\frac{B}{n'q}$ where n' is the effective two-dimensional charge carrier density.

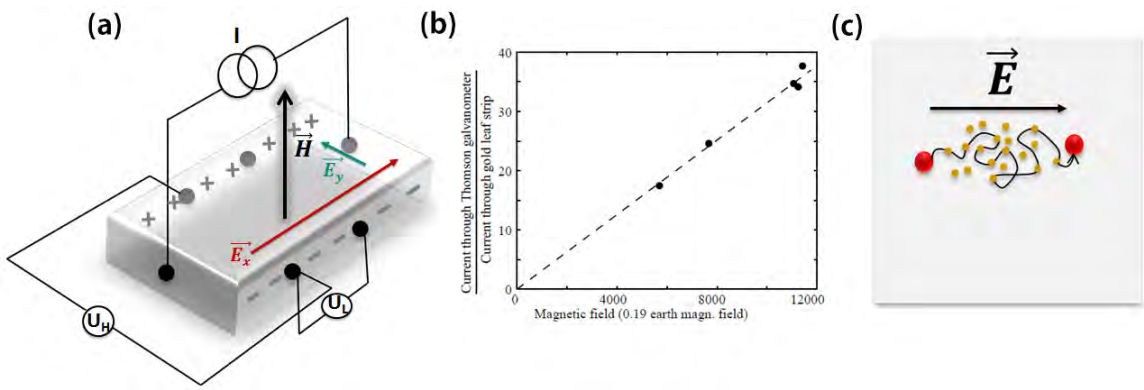

Figure 2.4: The Hall effect

The resistivity tensor $\bar{\rho}$, defined as the inverse of the conductivity tensor, is better suited to deal with samples having a bar geometry. This is because the resistivity tensor relates each component of the electric field to the components of the current flowing in the x and y-direction. In the bar geometry considered above, no current can flow in the y-direction and once one sets $j_y = 0$, the relation between j_x and E_x becomes straightforward.

$$\begin{pmatrix} E_x \\ E_y \end{pmatrix} = \begin{pmatrix} \rho_{xx} & \rho_{xy} \\ \rho_{yx} & \rho_{yy} \end{pmatrix} \cdot \begin{pmatrix} j_x \\ j_y \end{pmatrix} \underbrace{\Leftrightarrow}_{j_y=0} \begin{pmatrix} \rho_{xx} = \rho_L \equiv \frac{E_x}{j_x} \\ \rho_{xy} = \rho_H \equiv \frac{E_y}{j_x} \end{pmatrix} \tag{2.22}$$

Unlike their conductivity counterparts, the components of the resistivity tensor are directly accessible from experiment using a Hall bar sample where, on one hand, the voltage measured between two electrodes located on the same side of the bar provides the longitudinal resistivity $\rho_L = \rho_{xx} = \frac{l}{L}\frac{V_{xx}}{I}$ and on the other hand, the voltage measured between two electrodes located on opposite sides of the bar yields the Hall resistivity $\rho_H = \rho_{xy} = \frac{l}{L}\frac{V_H}{I}$. The two-dimensional resistivity tensor is obtained by conductivity tensor inversion ($\bar{\sigma}\bar{\rho} = \bar{1}$):

$$\rho = \begin{pmatrix} \rho_{xx} & \rho_{xy} \\ \rho_{yx} & \rho_{yy} \end{pmatrix} = \begin{pmatrix} \frac{\sigma_{xx}}{\sigma_{xx}^2+\sigma_{xy}^2} & \frac{-\sigma_{xy}}{\sigma_{xy}^2+\sigma_{xx}^2} \\ \frac{\sigma_{xy}}{\sigma_{xy}^2+\sigma_{xx}^2} & \frac{\sigma_{xx}}{\sigma_{xx}^2+\sigma_{xy}^2} \end{pmatrix} \tag{2.23}$$

Combining equations 2.23 and 2.15, the resistivity tensor can be re-written as a function of $\rho_0 = 1/\sigma_0 = \frac{m^*}{nq^2\tau}$ and the magnetic field:

$$\rho = \begin{pmatrix} 1/\sigma_0 & -\mu B/\sigma_0 \\ \mu B/\sigma_0 & 1/\sigma_0 \end{pmatrix} \equiv \begin{pmatrix} \rho_0 & -\rho_0\mu B \\ \rho_0\mu B & \rho_0 \end{pmatrix} \tag{2.24}$$

We note that the product of the zero-field resistivity by the mobility yields the Hall resistance ($\rho_0\mu = \frac{1}{nq} \equiv R_H$) in consistency with the Hall effect described above. The magnetic field dependence of the conductivity and resistivity tensor components are plotted in figure 6.6.

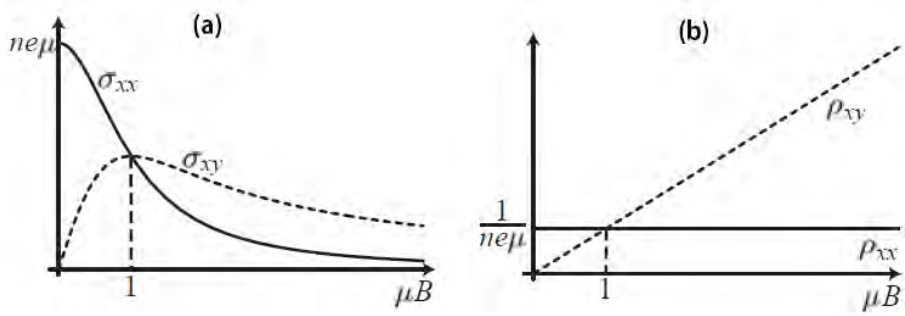

Figure 2.5: a) Components of the conductivity tensor as a function of the magnetic field. At $\mu B = 1$, $\sigma_{xx} = \sigma_{xy}$. (b) Components of the resistivity tensor as a function of magnetic field. For $\mu B = 1$, $\rho_{xx} = \rho_{xy}$

In the center of the Hall bar, the equipotentials makes an angle $\psi = \arctan(\mu.B) \equiv \arctan\left(\frac{B}{nq}\frac{1}{\rho_0}\right)$ with the y-axis. This angle is referred to as the Hall angle which does not depend on the geometry of the sample. The identification $\rho_{xx} = \rho_L$ and $\rho_{xy} = \rho_H$ is valid only when the Hall angle is constant, i.e. far from the contacts where the current lines (in the x-direction) are not perpendicular to the equipotentials. In other

words, far enough from the drain-source contacts which act as fixed equipotential volumes, the current lines are not aligned with the electric field lines. Conversely, the electric field and the current density are not uniform in the vicinity of the contacts, which breaks the initial hypotheses leading to equation 2.24. The minimum distance from the contacts where the uniform regime holds is estimated to $d = \ell \times \tan\psi \equiv \ell\mu B$. In the vicinity of the contacts, neither ρ_{xx} nor ρ_{xy} can be immediately identified to ρ_L and ρ_H, respectively, since $j_y \neq 0$.

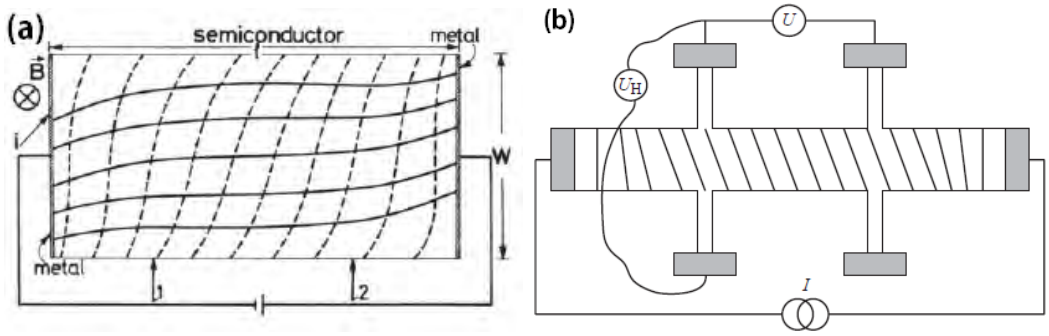

Figure 2.6: a) Equipotential (dashed) and electric field lines (solid) for a bar geometry. b) Full view of the equipotentials in a Hall bar configuration

2.1.4 Boltzmann transport equation in the presence of a magnetic field

To derive the conductivity tensor and the Hall effect with a statistical description of the electron gas in the presence of a homogeneous and constant magnetic field, our starting point is the Boltzmann equation with the mean relaxation time approximation where the distribution function is replaced by the carrier density.

$$\frac{\partial n}{\partial t} + \frac{\mathbf{p}}{m^*}\nabla_r(n) + \mathbf{F}\nabla_{\mathbf{p}}(n) = -\frac{n - n_{0(\mathbf{p})}}{\tau} \tag{2.25}$$

We now assume the permanent regime ($\frac{\partial n}{\partial t} = 0$) while the force $\mathbf{F} = q\left(\mathbf{E} + \frac{\mathbf{p}\wedge\mathbf{B}}{m^*}\right)$ results from an electric field $\mathbf{E} = E_x\hat{x}$ in the x-direction and a magnetic field $\mathbf{B} = B_z\hat{z}$ in the z-direction. The system is supposed homogeneous and isotropic so that $\nabla_r(n) = 0$. The Boltzmann equation is solved with a "test function" $n_{(\mathbf{p})} = (1+\phi) \times n_{0(\mathbf{p})}$ where ϕ is a perturbation term to be found. To complement the resolution of the Boltzmann equation in section 2.1.2, we shall use now the classical Boltzmann-Maxwell distribution function (instead of the Fermi-Dirac function) which reads $n_{0(\mathbf{p})} = n_0 \frac{\exp\left(-\frac{\mathbf{p}^2}{2m^* k_B T}\right)}{(2\pi m^* k_B T)^{3/2}}$. The use of Boltzmann-Maxwell distribution function allows straightforward simplifications of the Boltzmann equation and produces an easy

interpretation for the magneto-conductance tensor. The reader is invited to read reference [65] p.157 for a derivation using the Fermi-Dirac distribution function, whose results are reproduced in equations 2.57. The Boltzmann equation 2.25 reduces to:

$$
\begin{aligned}
n_{(\mathbf{p})} &= n_{0(\mathbf{p})} - \tau \mathbf{F} \nabla_{\mathbf{p}} \left(n_{(\mathbf{p})} \right) = n_{0(\mathbf{p})} - \tau \mathbf{F} \nabla_{\mathbf{p}} \left[(1+\phi) \times n_{0(\mathbf{p})} \right] \\
n_{(\mathbf{p})} &= n_{0(\mathbf{p})} - \tau \times \left[\mathbf{F} (1+\phi) \underbrace{\nabla_{\mathbf{p}} \left(n_{0(\mathbf{p})} \right)}_{-\frac{\mathbf{p}}{m^* k_B T} n_{0(\mathbf{p})}} + n_{0(\mathbf{p})} \underbrace{\mathbf{F} \nabla_{\mathbf{p}} (\phi)}_{q\left(\cancel{\mathbf{E}\nabla_{\mathbf{p}}(\phi)} + \frac{\mathbf{p}\wedge\mathbf{B}}{m^*} \nabla_{\mathbf{p}}(\phi)\right)} \right] \\
n_{(\mathbf{p})} &= n_{0(\mathbf{p})} - \tau \times \left[-q (1+\phi) \left(\mathbf{E} \left(\frac{\mathbf{p} n_{0(\mathbf{p})}}{m^* k_B T} \right) + \cancel{\frac{\mathbf{p} \wedge \mathbf{B}}{m^*} \left(\frac{\mathbf{p} n_{0(\mathbf{p})}}{m^* k_B T} \right)} \right) \right] \\
&+ n_{0(\mathbf{p})} q \frac{\mathbf{p} \wedge \mathbf{B}}{m^*} \nabla_{\mathbf{p}} (\phi) \\
n_{(\mathbf{p})} &= n_{0(\mathbf{p})} - \tau \times \left[-q (1+\cancel{\phi}) \left(\mathbf{E} \frac{\mathbf{p} n_{0(\mathbf{p})}}{m^* k_B T} \right) + n_{0(\mathbf{p})} q \frac{\mathbf{p} \wedge \mathbf{B}}{m^*} \nabla_{\mathbf{p}} (\phi) \right] \\
(1+\phi) \times n_{0(\mathbf{p})} &= n_{0(\mathbf{p})} + \tau \times \left[q \left(\mathbf{E} \frac{\mathbf{p} n_{0(\mathbf{p})}}{m^* k_B T} \right) - n_{0(\mathbf{p})} q \frac{\mathbf{p} \wedge \mathbf{B}}{m^*} \nabla_{\mathbf{p}} (\phi) \right]
\end{aligned}
\tag{2.26}
$$

Where the term $\mathbf{E}\nabla_{\mathbf{p}}(\phi)$ (second line of equation 2.26) and $\phi\left(\mathbf{E}\frac{\mathbf{p}n_{0(\mathbf{p})}}{m^* k_B T}\right)$ (fourth line of equation 2.26), which are of second order in $\mathbf{E}$, are neglected to keep only the linear response. On the other hand, the term $\frac{\mathbf{p}\wedge\mathbf{B}}{m^*}\left(\frac{\mathbf{p}n_{0(\mathbf{p})}}{m^* k_B T}\right)$ is null since $(\mathbf{p}\wedge\mathbf{B})$ is perpendicular to $\mathbf{p}$.

$$
\frac{\phi}{\tau} - \frac{q}{m^* k_B T} (\mathbf{E}\mathbf{p}) + \frac{q}{m^*} (\mathbf{p} \wedge \mathbf{B}) \nabla_{\mathbf{p}} (\phi) = 0 \tag{2.27}
$$

Introducing the notations $\omega_c = \frac{q\tau}{m^*}$ and $\xi = \left[1 + \omega_c^2 \tau^2\right]^{-1}$, the solution to this equation and hence the final form of $n_{(\mathbf{p})}$ are :

$$
\begin{aligned}
\phi &= \frac{q\tau\xi}{m^* k_B T} \mathbf{p}\mathbf{E} - \left(\frac{q\tau}{m^*}\right)^2 \frac{\xi}{k_B T} \mathbf{E} (\mathbf{p} \wedge \mathbf{B}) \\
n_{(\mathbf{p})} = n_0 (1+\phi) &\approx n_0 + \frac{q\tau\xi n_0}{m^* k_B T} (\mathbf{p}\mathbf{E}) - \left(\frac{q\tau}{m^*}\right)^2 \frac{n_0 \xi}{k_B T} \mathbf{E} (\mathbf{p} \wedge \mathbf{B})
\end{aligned}
\tag{2.28}
$$

When the electric and magnetic fields are set in the x- and z-direction respectively, the current flows in the x-y plane. The component of the vector current density is calculated using the relation $j_i = \frac{q}{m^*} \int_{(\mathbf{p})} n_{(\mathbf{p})} p_i d^3p$ where $i \equiv x, y$. The first term in

equation 2.28 does not contribute to the current for symmetry reason. We end up with :

$$j_x = \left(\frac{q}{m^*}\right)^2 \frac{1}{k_B T} \int_{\mathbf{p}} n_0 \tau \xi \left(p_x^2 E_x + \cancel{p_x p_y} E_y\right) d^3p - \left(\frac{q}{m^*}\right)^3 \frac{B}{k_B T} \int_{\mathbf{p}} n_0 \tau^2 \xi \left(p_x^2 E_y - \cancel{p_x p_y} E_x\right) d^3p \tag{2.29a}$$

$$j_y = \left(\frac{q}{m^*}\right)^2 \frac{1}{k_B T} \int_{\mathbf{p}} n_0 \tau \xi \left(\cancel{p_x p_y} E_x + p_y^2 E_y\right) d^3p - \left(\frac{q}{m^*}\right)^3 \frac{B}{k_B T} \int_{\mathbf{p}} n_0 \tau^2 \xi \left(\cancel{p_x p_y} E_y - p_y^2 E_x\right) d^3p \tag{2.29b}$$

where the cross-terms $p_x p_y$ yield no contribution to the integral for symmetry reasons. Comparing equations 2.29 and 2.15, we derive an expression for the components of the 2D conductivity tensor :

$$\sigma_{xx} = \frac{1}{3k_B T} \left(\frac{q}{m^*}\right)^2 \int_{(\mathbf{p})} \mathbf{p}^2 n_0 \tau \xi d^3p \tag{2.30}$$

$$\sigma_{xy} = \frac{B}{3k_B T} \left(\frac{q}{m^*}\right)^3 \int_{(\mathbf{p})} \mathbf{p}^2 n_0 \tau^2 \xi d^3p \tag{2.31}$$

$$\sigma_{yx} = -\frac{B}{3k_B T} \left(\frac{q}{m^*}\right)^3 \int_{(\mathbf{p})} \mathbf{p}^2 n_0 \tau^2 \xi d^3p \tag{2.32}$$

$$\sigma_{yy} = \frac{1}{3k_B T} \left(\frac{q}{m^*}\right)^2 \int_{(\mathbf{p})} \mathbf{p}^2 n_0 \tau \xi d^3p \tag{2.33}$$

where we used the isotropy of n_0, τ and ξ to replace the integral of the components of momentum by one-third the integral of the modulus of the vector momentum. We note, in agreement with Onsager's relations, that $\sigma_{xx}(B) = \sigma_{yy}(-B)$ and $\sigma_{xy}(B) = -\sigma_{yx}(-B)$. When the mean scattering time is independent of energy, the energy equipartition theorem $\frac{\int \frac{1}{2m^*} \mathbf{p}^2 . n_{0(\mathbf{p})} d^3p}{\int n_{0(\mathbf{p})} d^3p} = \frac{3}{2} k_B T$ can be used to simplify the expressions of σ_{xx} and σ_{xy}:

$$\sigma_{xx} = \frac{\sigma_0}{1 + \omega_c^2 \tau^2} \tag{2.34}$$

$$\sigma_{xy} = \frac{\sigma_0 \omega_c \tau}{1 + \omega_c^2 \tau^2} \equiv \sigma_{xx} \omega_c \tau \tag{2.35}$$

where $\int n_{0(\mathbf{p})} d^3p = n_0$ and $\sigma_0 = \frac{n_0 q^2 \tau}{m^*}$ is the zero-magnetic field conductivity. We end up with the same equations 2.15 provided by the Drude model. As stated earlier, the magneto-resistance does not depend on the magnetic field, which is at odd with most experimental observations where a quadratic behavior is observed for small enough magnetic field. This apparent contradiction is solved by introducing an energy-dependent scattering time $\tau_{(\mathbf{p})}$ for the mean values for the quantities of interests in equation 2.33. We define $\langle X \rangle = \frac{\int X_{(\mathbf{p})} . \mathbf{p}^2 . n_{0(\mathbf{p})} d^3p}{\int \mathbf{p}^2 . n_{0(\mathbf{p})} d^3p}$ where $X_{(\mathbf{p})} = \tau_{(\mathbf{p})} \xi_{(\mathbf{p})}$ or $\tau^2_{(\mathbf{p})} \xi_{(\mathbf{p})}$. Using once again the energy equipartition theorem (the denominator of the last equation can be replaced by $\frac{3}{2} k_B T n_0$) and the components of the conductivity tensor are:

$$\begin{aligned}
\sigma_{xx} &= \frac{1}{3k_B T} \left(\frac{q}{m^*}\right)^2 \times \int_{(\mathbf{p})} \mathbf{p}^2 n_{0(\mathbf{p})} \tau_{(\mathbf{p})} \xi_{(\mathbf{p})} d^3p \\
&= \frac{1}{3k_B T} \left(\frac{q}{m^*}\right)^2 \times \langle \tau \xi \rangle \int_{(\mathbf{p})} \mathbf{p}^2 n_{0(\mathbf{p})} d^3p \\
&= \frac{2m^*}{3k_B T} \left(\frac{q}{m^*}\right)^2 \times \langle \tau \xi \rangle \times \frac{3}{2} k_B T n_0 \\
&= \frac{q^2 n_0 \langle \tau \xi \rangle}{m^*}
\end{aligned} \tag{2.36a}$$

$$\begin{aligned}
\sigma_{xy} &= \frac{B}{3k_B T} \left(\frac{q}{m^*}\right)^3 \times \int_{(\mathbf{p})} \mathbf{p}^2 n_{0(\mathbf{p})} \tau^2_{(\mathbf{p})} \xi_{(\mathbf{p})} d^3p \\
&= \frac{B}{3k_B T} \left(\frac{q}{m^*}\right)^3 \times \langle \tau^2 \xi \rangle \int_{(\mathbf{p})} \mathbf{p}^2 n_{0(\mathbf{p})} d^3p \\
&= \frac{2m^* B}{3k_B T} \left(\frac{q}{m^*}\right)^3 \times \langle \tau^2 \xi \rangle \times \frac{3}{2} k_B T n_0 \\
&= \frac{B q^3 n_0 \langle \tau^2 \xi \rangle}{m^{*2}}
\end{aligned} \tag{2.36b}$$

When the sample is within the Hall geometry, the current is forced to flow in the x-direction while the Hall and longitudinal voltages are measured along the y- and x-direction, respectively. Setting $j_y = 0$ in equation 2.15, we end up with $E_y = \frac{\sigma_{xy}}{\sigma_{xx}} . E_x$ which, together with $j_x = \sigma_L(B) E_x$, provides $\sigma_L(B) = \frac{\sigma^2_{xx} + \sigma^2_{xy}}{\sigma_{xx}} = \sigma_0 \frac{\langle \tau \xi \rangle}{\tau} \left[1 + \left(\frac{qB}{m^*} \frac{\langle \tau^2 \xi \rangle}{\langle \tau \xi \rangle} \right)^2 \right]$. The longitudinal magneto-conductance and hence the longitudinal magneto-resistance $\rho_L \equiv \rho_{xx} = 1/\sigma_L$ are now magnetic field dependent.

2.2 Transport phenomena in quantizing Magnetic

When the magnetic field is strong enough ($\mu.B = \omega_c.\tau > 1$), the charge carrier can complete at least one complete cyclotron orbit before being scattered. Such a circular motion resembles the classical trajectory of an electron bound to its positively charged nucleus in the hydrogen atom. This problem was first tackled by N. Bohr in 1913 who, based on heuristic arguments, found that the kinetic moment $\mathbf{L}$ of the electron is quantized by units of the Planck constant. An alternative and more natural explanation was proposed after De Broglie introduced the particle wave duality in 1923, as the circular electron orbit must be an integer number of the quantum wavelength $\lambda = \frac{2\pi}{k} = \frac{h}{p}$.

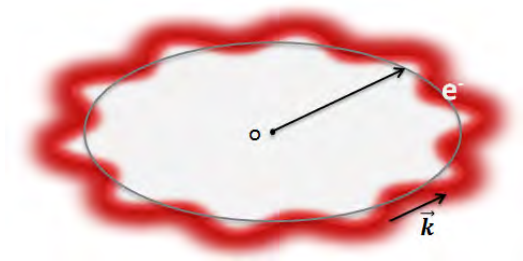

Figure 2.7: Semi-classical model of a charged particle in a magnetic field. The wave-function is a quasi-plane wave defined by k spreading along a circular trajectory of length L. The wave-function cannot be multiply defined, thus imposing the condition kL = 2πN.

Indeed, in such a semi-classical description, this constraint is imposed in closed loop trajectories since the electron wave-function cannot be multiply-defined (e.g. have different phase) at any given positions. Classically, a charged particle of effective mass m^* and charge q has a circular motion in the presence of an external magnetic field with constant pulsation $\omega_c = eB/m^*$. We note r the radius and $v = r\omega_c$ the constant velocity. The elementary quantum phase acquired as the charged particle travels along its orbit is $d\varphi = d(\mathbf{kr})$ where $\hbar\mathbf{k} = m^*\mathbf{v} - q\mathbf{A}$. We compute:

$$2\pi n = \int_{circ} d\varphi = \int_{circ} \mathbf{k}d\ell = \frac{1}{\hbar}\int_{circ} m^* v\hat{\theta} r d\theta\hat{\theta} - q\mathbf{A}d\ell$$

$$2\pi n = \frac{1}{\hbar}\int_0^{2\pi} m^* r^2 \omega_c d\theta + \frac{1}{\hbar}\iint_S -q\nabla(\mathbf{A})\mathbf{dS} = \frac{1}{\hbar}\left[2\pi m^* r^2 \frac{eB}{m^*} - qB\pi r^2\right]$$

$$2\pi\hbar n = \pi r^2 qB \Leftrightarrow r = \sqrt{2n}\ell_B$$

where $\ell_B = \sqrt{\frac{\hbar}{eB}}$ is the magnetic length. For a given energy (or momentum), the interference of the electron wave-function along its orbit is constructive when the radius scales as $\sqrt{2n} \times \ell_B$, and destructive for any other radius. In other words, a charge makes a circular motion at pulsation ω_c only for particular values of the radius. Using the relation $\epsilon_c = \frac{1}{2}m^* v^2 = \frac{1}{2}L\omega_c$, we find that the kinetic energy is also

quantized in units of $\hbar\omega_c$. Although this heuristic model predicts the quantization of the cyclotron radius and the kinetic energy of a free charged particle in the presence of a magnetic field, the correct interpretation requires a full quantum mechanical treatment detailed in sections 2.2.1 and 2.2.2, leading to the Landau levels spectrum. Next, we will discuss the Landau levels' implication in transport measurement in section 2.2.3, and in particular the oscillations of the magneto-resistance also referred to as the Shubnikov-de Haas oscillations. In section 2.2.4, we introduce the spin of the charge carriers leading to another energy scale (Zeeman energy) which competes with the energy of the Landau levels. Finally, we will review how to extract the carrier density and effective mass of the charge carriers using the Lifshitz-Kosevitch equation in the last section 2.2.5.

2.2.1 Landau levels

Let us consider a three-dimensional gas of charged particles with a magnetic field $\mathbf{B} = \mathbf{rot}\,(\mathbf{A})$ oriented along the direction [Oz]. We shall use the Landau gauge for the vector potential, so that $A_x = -By$, $A_y = 0$ and $A_z = 0$. The sample has finite dimensions in all directions, even though the length is often much longer than the width and the thickness in the bar configuration. We therefore introduce a potential $V_{(y,z)} = V'_{(y)} + V''_{(z)}$ to take into account the finite lateral dimensions of the bar, while the electrons are not confined in the x-direction. The Schrödinger equation is:

$$\left[\frac{\left(-i\hbar\frac{\partial}{\partial x} - qBy\right)^2}{2m^*} - \frac{\hbar^2}{2m^*}\left(\frac{\partial^2}{\partial y^2} + \frac{\partial^2}{\partial z^2}\right) + V_{(y,z)}\right]\Psi_{(x,y,z)} = \epsilon \times \Psi_{(x,y,z)} \tag{2.37}$$

The bracket term is the Hamiltonian which contains the kinetic and magnetic field energy of the charged particles through the Peierls substitution of the classical momentum $\mathbf{p} \to \mathbf{p} + q.\mathbf{A}$. We recall that the kinetic momentum operator is $\mathbf{p} = -i\hbar\nabla$. We expand equation 2.37 which writes:

$$\left[-\frac{\hbar^2}{2m^*}\frac{\partial^2}{\partial x^2} + \frac{2i\hbar qBy}{2m^*}\frac{\partial}{\partial x} + \frac{(qBy)^2}{2m^*} - \frac{\hbar^2}{2m^*}\frac{\partial^2}{\partial y^2} - \frac{\hbar^2}{2m^*}\frac{\partial^2}{\partial z^2} + V'_{(y)} + V''_{(z)}\right].\Psi_{(x,y,z)} \tag{2.38}$$
$$= \epsilon \times \Psi_{(x,y,z)}$$

We are looking for a solution of the Schrödinger equation (wave-function) in the form $\Psi_{(x,y,z)} = \phi_{(x)} \times \eta_{(y)} \times \xi_{(z)}$. Such a a "test wave-function" is first motivated by noticing that no potential energy is affected to the x-direction. Despite the fact that the Hamiltonian couples the operators $\partial/\partial x$ and y, both of them commute with the kinetic momentum p_x. Therefore, we expect $\phi_{(x)}$ to take the form of a plane

wave (free particle). Second, we notice that all terms involving the z-direction are independent in the Schrödinger equation, which can therefore be broken into two separate equations:

$$\left[-\frac{\hbar^2}{2m^*}\frac{\partial^2}{\partial x^2}+\frac{i\hbar qBy}{2}\frac{\partial}{\partial x}+\frac{(qBy)^2}{2m^*}-\frac{\hbar^2}{2m^*}\frac{\partial^2}{\partial y^2}+V'_{(y)}\right]\phi_{(x)}\times\eta_{(y)}=\epsilon_{(x,y)}\times\phi_{(x)}\times\eta_{(y)} \tag{2.39}$$

$$\left[-\frac{\hbar^2}{2m^*}\frac{\partial^2}{\partial z^2}+V''_{(z)}\right]\xi_{(z)}=\epsilon_{(z)}\times\xi_{(z)} \tag{2.40}$$

As expected, the second line is the standard one-dimensional Schrödinger equation for a particle moving in a potential well $V''_{(z)}$. This equation will be dropped off in order to focus on the two dimensional wave-function $\phi_{(x)}\times\eta_{(y)}$ governed by the first equation. If the gas of charged particle is not confined in the z-direction ($V''_{(z)}\equiv 0$), the kinetic energy $\hbar^2.k_z^2/2m^*$ should simply add to the total energy eigenvalues. Setting $\phi_{(x)}=\frac{1}{\sqrt{L_x}}e^{ik_xx}$ (plane wave in the x-direction) and assuming $V'_{(y)}=\frac{1}{2}.m^*.\omega_0.y^2$, the Schrödinger equation simplifies to:

$$\begin{aligned}\epsilon_{(k_x,y)}\times\eta_{(k_x,y)}&=\left[\frac{\hbar^2}{2m^*}\frac{\partial^2}{\partial y^2}+\frac{1}{2}.\hbar.\omega_c\left(y-\frac{\hbar.k_x}{q.B}\right)^2+\frac{1}{2}m^*\omega_0y^2\right]\eta_{(k_x,y)}\\&=\left[\frac{\hbar^2}{2m^*}\frac{\partial^2}{\partial y^2}+\frac{1}{2}m^*\left(\alpha^2\times(y-y_k)^2+\beta\right)\right]\eta_{(k_x,y)}=E_{(k_x,y)}\times\eta_{(k_x,y)}\end{aligned} \tag{2.41}$$

where we introduced the cyclotron frequency $\omega_c=qB/m^*$. The choice of harmonic confinement potential in the y-direction is justified only because it allows analytical solutions. Indeed, equation 2.41 takes the form to the 1D-Schrödinger equation for a particle confined in an effective harmonic potential of strength $\alpha^2=\omega_c^2+\omega_0^2$ centered at coordinate $y_k=\left(\omega_c^2\frac{\hbar k_x}{qB}\right)/(\omega_c^2+\omega_0^2)$. The additional term $1/2m^*\beta=1/2m^*\left[\left(\frac{\hbar k_x}{m^*}\right)^2\times\frac{\omega_0^2}{\omega_0^2+\omega_c^2}\right]$ is a constant with respect to the y-differential equation, and will add simply to the energy eigenvalues. We note that the wavefunction and eigenenergies for the y-component of the wave-function depends now both on y and k_x as

$$\eta_{N(k_x,y)}\propto\exp\left[-\frac{1}{2}\frac{m^*\sqrt{\omega_c^2+\omega_0^2}}{\hbar}(y-y_k)^2\right]\times H_{N[\sqrt{\frac{m^*\alpha}{\hbar}}(y-y_k)]} \tag{2.42}$$

$$\epsilon_{N(k_x,y)}=\hbar\sqrt{\omega_c^2+\omega_0^2}\left(N+\frac{1}{2}\right)+\frac{\hbar^2k_x^2}{2m^*}\frac{\omega_0^2}{\omega_0^2+\omega_c^2} \tag{2.43}$$

where N is an integer and H_N is the Hermite polynomial of the Nth order. In the absence of confining potential in the y-direction ($\omega_0 \equiv 0$), the eigen-energies are $\epsilon_N = \left(N + \frac{1}{2}\right)\hbar\omega_c$ so that the kinetic energy is quantized in units of $\hbar\omega_c$, as anticipated using the semi-classical model for high enough energy quantum states. Quantum states with small k_x wave-vector (in other words far from the edges of the sample since $y_k \sim k_x$) are localized and do not contribute much to the transport properties. On the other hand, quantum states close to the edges have a large group velocity ($v_g = 1/\hbar.\partial E/\partial k_x$) and contribute to the conductance. These quantum states are referred to "chiral edge states" since the group velocity is opposite at opposite edges of the sample.
Let us specify the length and width of the 2D system with L_x and L_y, respectively. Since the system is quasi-infinite in the x-direction, the energy does not depend on k_x. In other words, many quantum states with wave-vector allowed by the condition $k_x L_x = 2\pi n$ have the same energy. When the magnetic confinement is larger than the geometrical confinement, we note that $y_k \approx \frac{\hbar k_x}{qB}$ so that the width of a quantum state defined by the wave-vector k_x is $\delta y_k \approx \frac{\hbar.\delta k_x}{q.B}$. Clearly, the ratio between the sample's width to the width occupied by one quantum state defines the number of quantum states allowed per unit energy for the whole sample. The density of states at energy ϵ_N is derived by computing the number of quantum states allowed per unit energy per surface as follows:

$$g_{L(\epsilon_N)} = \frac{1}{S}\frac{L_y}{\delta y_k} = \frac{1}{L_x L_y} L_y \frac{qB}{\hbar \delta k_x} = \frac{qB}{\hbar L_x}\frac{L_x}{2\pi} = \frac{qB}{h} \tag{2.44}$$

The density of states is proportional to magnetic field and does not depend on the index N. These states are commonly referred to "Landau levels" at energy $\epsilon_N = \hbar.\omega_c\,(N + 1/2)$ with orbital degeneracy $g_L = q.B/h$. The degeneracy of Landau levels is increased to $g_s.g_L$ for electron gas where $g_s = 2$ stands for the spin degeneracy. We finish this section by introducing the filling factor $\nu_{(B)}$ which counts how many Landau levels are occupied in a system with carrier density n. In other words, the filling factor is the ratio of the carrier density to the Landau level degeneracy which takes the simple form:

$$\nu_{(B)} = \frac{n}{g_s g_L} = \frac{nh}{g_s qB} \tag{2.45}$$

Considering a constant Fermi energy (this approximation is valid for large filling factors only), the density of states of the conduction electrons will be large each time the energy of the Landau levels crosses the Fermi energy, that is when the filling factor is half integer. The magneto-resistivity of the systems, which depends in a complicate manner to the density of states at the Fermi energy when disorder is introduced, will therefore reflects the quantization of the system's energy into Landau levels and will oscillate with filling factor in a 1/B-periodic fashion.

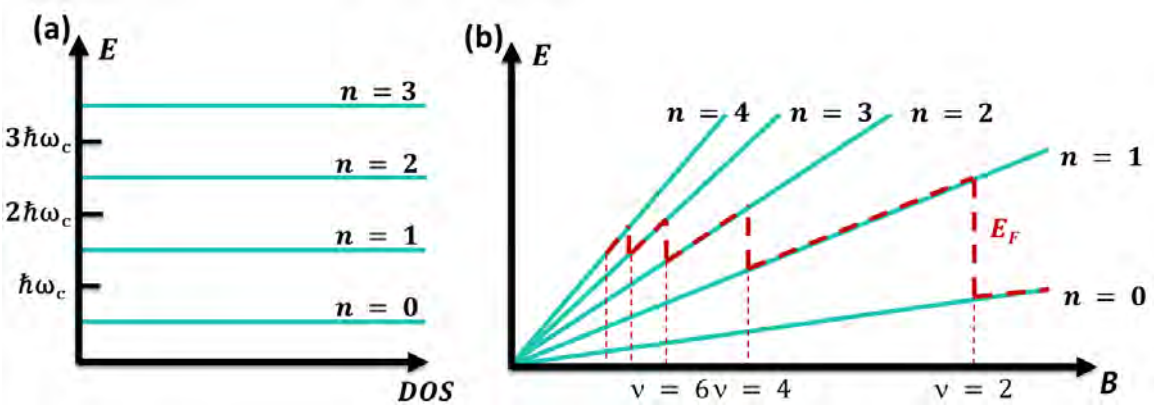

Figure 2.8: (a) The corresponding density of states Density of states (DOS) for a free 2DEG perpendicular to the magnetic field without disorder. (b) Energy levels for electrons under a magnetic field. The slope depends on the quantum number N. At a fixed electron density the Fermi energy (red dashes) oscillates as a function of the filling factor.

2.2.2 Landau levels broadening

Impurities and defects in the crystal are always present and act as a source of scattering for the charged carriers. As a consequence, the lifetime of a quantum state is limited and is referred to as τ_q: the mean quantum lifetime. Its physical interpretation is similar to the Drude mean scattering time, although the latter includes a cosine dependence of the scattering angle when multiplied by the raw scattering probability in order to put more weight on back-scattering events. Depending on the nature of scattering (e.g. range of interaction with scatterers), the quantum lifetime can be one order of magnitude shorter than its Drude counterpart. When disorder is introduced, the delta function density of states of the ideal Landau level (equation 2.44) is broadened as shown in figure 6.8. Let us assume that lifetime broadening leads to a Lorentzian density of states

$$DoS^{2D}_{(\epsilon)} = g_L g_s \frac{1}{\pi} \sum_{N=0} \frac{\frac{\hbar}{2\tau_q}}{(\epsilon - \epsilon_N)^2 + \left(\frac{\hbar}{2\tau_q}\right)^2} \tag{2.46}$$

where $1/\tau_q$ is the mean scattering rate and $\hbar/\tau_q$ is the energy broadening according to time-energy uncertainty relation. A difficulty arises by noting that the mean scattering rate is not constant under magnetic field, but actually depends on the density of states at the Fermi energy. Considering short-range scatterers, first order perturbation theory [65] yields $1/\tau_{q(\epsilon)} = (2\pi/\hbar)\, n_i \bar{\mathbf{v}^2} DoS^{2D}_{(\epsilon)}$ where n_i is the areal density of scatterers and $\bar{\mathbf{v}^2}$ is an angle and impurity ensemble averaged squared scattering matrix element. Inserting this expression into equation 2.46 yields the

elliptic density of states which now depends only on energy:

$$DoS^{2D}_{(\epsilon)} = \frac{n_L n_s}{\pi\Gamma} \sum_{N=0}^{+\infty} \left[1 - \left(\frac{\epsilon - \epsilon_N}{\Gamma_N}\right)^2\right]^{1/2} \tag{2.47}$$

where $\Gamma = \sqrt{\frac{1}{2\pi}\hbar\omega_c \frac{\hbar}{\tau_{q(0)}}}$ and $\tau_{q(0)}$ is the zero-magnetic field quantum lifetime. This expression for Γ is valid only if the magnetic length is such that $\ell_B\,(2N+1)^{1/2} > d$ where d is the range of the scattering potential. This model predicts that Landau level broadening is independent on the index N and scales with the square-root of the magnetic field. However, it fails to reproduce the tail of the Landau levels since $DoS^{2D}_{(\epsilon)} = 0$ for $|\epsilon - \epsilon_N| > \Gamma$. An alternative description [109] of the broadened density of states considers a Gaussian function:

$$Dos^{2D}_{(\epsilon)} = g_L.g_s.\sqrt{\frac{2}{\pi\Gamma^2}} \sum_{N=0}^{+\infty} \exp\left(\frac{-2\,(\epsilon - \epsilon_N)^2}{\Gamma^2}\right) \tag{2.48}$$

If the scattering rate $(1/\tau_q)$ is sufficiently large, the Landau levels merge into one another and the oscillatory behavior observed in Shubnikov-de Haas measurements is damped. Meanwhile, such oscillations will be observed only if distinct Landau levels exist, which implies that the broadening $\hbar/\tau_q$ should be less than the Landau level spacing $\epsilon_{(N)} - \epsilon_{(N-1)} = \hbar\omega_c$.

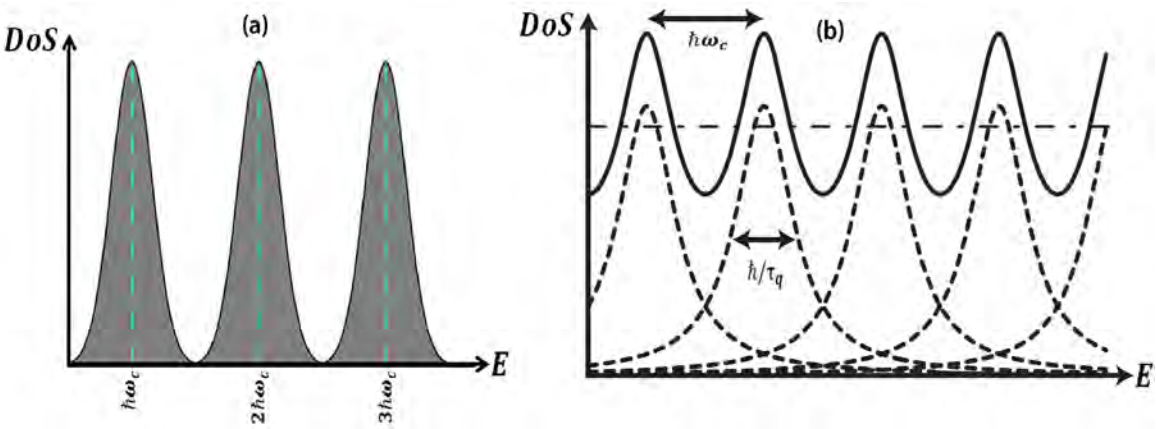

Figure 2.9: (a) The individual landau levels are broadened due to the presence of charged scatterers causing potential fluctuations in the sample. (b) The sum of broadened Landau levels defines the density of states. The modulation of the density of states induced by the magnetic field can be experimentally detected if the individual Landau levels are sufficiently separated. Adapted from [65, 70].

2.2.3 Shubnikov-de Haas oscillations

Under magnetic field, the density of states can be approximated as the sum of individual broadened Landau levels centered at energy $\epsilon_n = \hbar\omega_c\,(n + 1/2)$. We will assume a Lorentzian broadening so that each Landau level contributes to the total density of states a quantity $g_L.\mathcal{L}\,(\epsilon - \epsilon_n)$ where g_L is the orbital Landau level degeneracy (see equation 2.44) and $\mathcal{L}$ is a Lorentzian function of HWFM equals to $\hbar/\tau_q$. The density of states reads:

$$DoS_{(\epsilon,B)} = g_s g_L \sum_n \mathcal{L}_{(\epsilon-\epsilon_n)} \tag{2.49}$$

The sum over several Lorentzian fonctions peaked at different energies leads to an oscillatory behavior, which is better visualized by rewriting the density of states using Poisson's summation formula ($\sum_{n=0}^{\infty} f(n+1/2) = \int_0^{\infty} f(x)dx + 2\sum_{s=1}^{\infty}(-1)^s \int_0^{\infty} f(x)\cos(2\pi xs)dx$):

$$DoS^{2D}_{(\epsilon,B)} = g_s g_L \sum_n \mathcal{L}_{(\epsilon-\hbar\omega_c\left(n+\frac{1}{2}\right))} \tag{2.50}$$

$$DoS^{2D}_{(\epsilon,B)} = g_s g_L \times \left[\int_0^{\infty} \mathcal{L}(\epsilon - \hbar\omega_c x)dx + 2\sum_{s=1}^{\infty}(-1)^s \int_0^{\infty} \mathcal{L}(\epsilon - \hbar\omega_c x)\cos(2\pi xs)dx\right] \tag{2.51}$$

$$DOS^{2D}_{(\epsilon,B)} = \frac{g_s g_L}{\hbar\omega_c}\left[\int_{-\infty}^{\epsilon} \mathcal{L}(\xi)d\xi + 2\sum_{s=1}^{\infty}(-1)^s \int_{-\infty}^{\epsilon} \mathcal{L}(\xi)\cos\left(\frac{2\pi(\epsilon-\xi)s}{\hbar\omega_c}\right)d\xi\right] \tag{2.52}$$

where we changed the variable $\xi = \epsilon - \hbar\omega_c x$ from the second to the third equation. When the energy is much higher than the typical Landau level width $\hbar/\tau_q$, the upper bound of the integral may be replaced by $+\infty$. We remind $g_L = qB/h$ and $\omega_c = qB/m^*$ so that the prefactor of equation 2.52 simplifies to $m^*/\pi\hbar^2$ (for $g_s = 2$) which is equal to the two dimensional density of states for a free electron gas. Besides, the first term in bracket reduces to 1 since it corresponds to the total area enclosed by a Lorentzian function. We end up with:

$$DoS^{2D}_{(E,B)} = \frac{m^*}{\pi\hbar^2}\left[1 + \frac{\Delta\mathcal{D}}{\mathcal{D}}\right] \text{ where } \frac{\Delta\mathcal{D}}{\mathcal{D}} = 2\sum_{s=1}^{\infty}(-1)^s \int_{-\infty}^{E} \mathcal{L}(\xi)\cos\left(\frac{2\pi(\epsilon-\xi)s}{\hbar\omega_c}\right)d\xi \tag{2.53}$$

is the unit-less oscillatory part of the density of states. The term $\Delta\mathcal{D}/\mathcal{D}$ can be

alternatively written:

$$\frac{\Delta\mathcal{D}}{\mathcal{D}} = 2\sum_{s=1}^{\infty}(-1)^s \left[\cos\left(\frac{2\pi\epsilon s}{\hbar\omega_c}\right)\int_{-\infty}^{\infty} L(\xi)\cos\left(\frac{2\pi\xi s}{\hbar\omega_c}\right)d\xi + \sin\left(\frac{2\pi\epsilon s}{\hbar\omega_c}\right)\underbrace{\int_{-\infty}^{\infty} L(\xi)\sin\left(\frac{2\pi\xi s}{\hbar\omega_c}\right)d\xi}_{=0 \text{ if } \mathcal{L}(\xi)=\mathcal{L}(-\xi)}\right]$$

$$= 2\sum_{s=1}^{\infty}(-1)^s\cos\left(\frac{2\pi\epsilon s}{\hbar\omega_c}\right)\int_{-\infty}^{\infty} L(\xi)\cos\left(\frac{2\pi\xi s}{\hbar\omega_c}\right)d\xi = 2\sum_{s=1}^{\infty}(-1)^s\cos\left(\frac{2\pi\epsilon s}{\hbar\omega_c}\right)\times\tilde{\mathcal{L}}\left(\frac{2\pi s}{\hbar\omega_c}\right)$$

$$= 2\sum_{s=1}^{\infty}(-1)^s\cos\left(\frac{2\pi\epsilon s}{\hbar.\omega_c}\right)\times\exp\left(\frac{-\pi s}{\omega_c\tau_q}\right) \tag{2.54}$$

The second integral of the first equation vanishes for symmetry reasons if the Landau levels are identically broadened on both sides of ϵ_n while the first integral corresponds to the cosine Fourier transform of the Lorentzian function noted $\tilde{\mathcal{L}}\left(\frac{2\pi s}{\hbar\omega_c}\right)$. This Fourier transform, which can be alternatively written $\exp\left(\frac{-\pi s}{\omega_c.\tau_q}\right)$, is known as the Dingle factor and accounts for the effect of the finite Landau level width on the density of states oscillations. When the magnetic field increases, the amplitude of the modulation of the density of states increases exponentially.
We would like now to move one step forward and compute the magneto-resistance tensor from the above established low-field density of states. Looking back to the transport equations provided in sections 2.1.4 and 2.1.3, only the mean scattering time can have a connection with the density of states. This relation is very complex to establish and is out of the scope of this thesis. Instead, we hypothesize from heuristic arguments that the energy-dependent scattering rate $1/\tau_{(\epsilon)}$ is proportional to the density of states. In other words, an electron at the Fermi energy is likely to scatter when there are many unoccupied quantum states with close energy. We write:

$$\frac{1}{\tau_{(\epsilon)}} = \frac{1}{\tau_{0(\epsilon)}}\left(1+\frac{\Delta\mathcal{D}}{\mathcal{D}}\right) \text{ so that } \tau_{(\epsilon)} = \tau_{0(\epsilon)}\left(1-\frac{\Delta\mathcal{D}}{\mathcal{D}}\right) \tag{2.55}$$

where $1/\tau_{0(\epsilon)}$ is the zero-magnetic-field scattering rate. We now insert this expression of $\tau_{(\epsilon)}$ into the components of the conductivity tensor established using the Boltzmann equation with the Fermi-Dirac distribution function [65]

$$\sigma_{xx}(\epsilon) = \int\left(\frac{-\partial f_{0(\epsilon)}}{\partial\epsilon}\right)\times\frac{1}{m^*}\frac{nq^2\tau_{(\epsilon)}}{1+\omega_c^2\tau_{(\epsilon)}^2}\times d\epsilon \tag{2.56}$$

$$\sigma_{xy}(\epsilon) = \int\left(\frac{-\partial f_{0(\epsilon)}}{\partial\epsilon}\right)\times\frac{1}{m^*}\frac{nq^2\omega_c\tau_{(\epsilon)}^2}{1+\omega_c^2\tau_{(\epsilon)}^2}\times d\epsilon \tag{2.57}$$

and we keep only the linear terms in $\Delta\mathcal{D}/\mathcal{D}$. Neglecting the energy dependence of $\tau_{0(\epsilon)}$ we end up with

$$\sigma_{xx}(\epsilon) = \int \left(\frac{-\partial f_{0(\epsilon)}}{\partial \epsilon}\right) \times \frac{1}{m^*}\frac{nq^2\tau_0}{1+\omega_c^2\tau_0^2}\left[1 - \frac{1-\omega_c^2\tau_0^2}{1+\omega_c^2\tau_0^2}\frac{\Delta\mathcal{D}}{\mathcal{D}}\right] \times d\epsilon \tag{2.58}$$

$$\sigma_{xy}(\epsilon) = \int \left(\frac{-\partial f_{0(\epsilon)}}{\partial \epsilon}\right) \times \frac{1}{m^*}\frac{nq^2\omega_c\tau_0^2}{1+\omega_c^2\tau_0^2}\left[1 - \frac{2}{1+\omega_c^2\tau_0^2}\frac{\Delta\mathcal{D}}{\mathcal{D}}\right] \times d\epsilon \tag{2.59}$$

where the main mathematical difficulty is to evaluate the expression $\int_{-\infty}^{+\infty}\left(\frac{-\partial f_{0(\epsilon)}}{\partial \epsilon}\right) \times \cos\left(\frac{2\pi\epsilon s}{\hbar\omega_c}\right) d\epsilon$ (we remind that $\Delta\mathcal{D}/\mathcal{D}$ is a cosine function of the energy according to equation 2.54). Using the formula

$$\int_{-\infty}^{+\infty}\left(\frac{-\partial f_{0(\epsilon)}}{\partial \epsilon}\right) \times \cos\left(\frac{2\pi\epsilon s}{\hbar\omega_c}\right) d\epsilon = \frac{1}{2}\cos\left(\frac{2\pi\epsilon s}{\hbar\omega_c}\right) \times \int_{-\infty}^{+\infty}\frac{\cos\left(\frac{4\pi s k_B T}{\hbar\omega_c}x\right)}{\cosh(x)}dx \tag{2.60}$$

$$= -\frac{\frac{2\pi^2 s k_B T}{\hbar\omega_c}}{\sinh\left(\frac{2\pi^2 s k_B T}{\hbar\omega_c}\right)} \times \cos\left(\frac{2\pi s\epsilon_F}{\hbar\omega_c}\right) \tag{2.61}$$

we obtain the final expressions for the component of the conductivity tensor :

$$\sigma_{xx} = \frac{1}{m^*}\frac{n.q^2\tau_0}{1+\omega_c^2\tau_0^2}\left[1 - \sum_{s=1}^{\infty}(-1)^s \times 2\frac{1-\omega_c^2\tau_0^2}{1+\omega_c^2\tau_0^2} \times \exp\left(\frac{-\pi s}{\omega_c\tau_q}\right) \times \frac{\frac{2\pi^2 s k_B T}{\hbar\omega_c}}{\sinh\left(\frac{2\pi^2 s k_B T}{\hbar\omega_c}\right)} \times \cos\left(\frac{2\pi h n s}{2qB}\right)\right] \tag{2.62a}$$

$$\sigma_{xy} = \frac{1}{m^*}\frac{nq^2\omega_c\tau_0^2}{1+\omega_c^2\tau_0^2}\left[1 - \sum_{s=1}^{\infty}(-1)^s \times \frac{4}{1+\omega_c^2\tau_0^2} \times \exp\left(\frac{-\pi s}{\omega_c\tau_q}\right) \times \frac{\frac{2\pi^2 s k_B T}{\hbar\omega_c}}{\sinh\left(\frac{2\pi^2 s k_B T}{\hbar\omega_c}\right)} \times \cos\left(\frac{2\pi h n s}{2qB}\right)\right] \tag{2.62b}$$

We remind, here, that τ_0 is the mean scattering time at zero magnetic field (which we assumed independent of energy), while τ_q is the lifetime of the quantum states. By inverting the conductivity tensor and keeping only the linear terms in $\Delta\mathcal{D}/\mathcal{D}$, one can

recover the expression of the longitudinal resistivity named after the Lifshitz-Kosevich formula:

$$\rho_L = \rho_{xx} = \frac{m^*}{nq^2\tau_0}\left[1 + \sum_{s=1}^{\infty}(-1)^s \times 2\exp\left(\frac{-\pi s}{\omega_c\tau_q}\right) \times \frac{\frac{2\pi^2 s k_B T}{\hbar\omega_c}}{\sinh\left(\frac{2\pi^2 s k_B T}{\hbar\omega_c}\right)} \times \cos\left(\frac{2\pi hns}{2qB}\right)\right] \tag{2.63}$$

The longitudinal resistivity is composed of two terms. The first one is constant and corresponds to the expression of the resistivity established within to the Drude model (see equation 6.8). The second term is an oscillation function with respect to the inverse of the magnetic field. The oscillation frequency of the first harmonic (s=1) $f = hn/2q$ is proportional to the carrier density as well as the spin degeneracy (the factor 2 in the denominator). As anticipated using the Einstein relation for conductivity $\sigma_E = DoS^{2D}q^2D_{(\tau)}$, where D is the diffusion coefficient which depends on the mean scattering time, the conductivity and hence the resistivity show minima when the Fermi energy lies at minima of the density of states. The Dingle factor accounts for the finite lifetime broadening of the Landau levels and is responsible for the exponential increase of the amplitude of the oscillations as the magnetic field increases. The term $X/\sinh(X)$ corresponds to the thermal broadening which tends to reduce the amplitude of the oscillations as a result of energy averaging over k_BT around the Fermi energy. The Lifschitz-Kosevich formula is valid only for small magnetic field, where the ridge of the density of states display a series of maxima and minima corresponding to the onset of Landau levels made of extended states only. We end this section by remarking that the resistivity ρ_{xy} (not computed here) does not have an oscillatory behaviour. This statement is valid only for long-range scattering potentials within approximation 2.55. In the case of short-range scatterers, an oscillating contribution to ρ_{xy} appears. In some experimental realizations, the longitudinal resistivity shows weak oscillations on top a large background (consider, for instance, the results established in section 2.1.4) so that they are hardly exploitable. On the other hand, the same oscillations can be better extracted for the weak and linear Hall resistivity background.

2.2.4 Zeeman energy

In the presence of a magnetic field, the energy spectrum of a free electron gas within the effective mass approximation is quantized into Landau levels as shown in section 2.2.1. However, because the charge carriers (electrons or holes) have a spin of 1/2, an extra energy term arises coined the Zeeman energy:

$$\epsilon_Z = g\mu_B\sigma B \tag{2.64}$$

where $\mu_B = q\hbar/2m$ is the Bohr magneton which links the kinetic orbital moment to

the magnetic moment via the factor g . In the case of spin $\sigma = \pm 1/2$ particles such as electrons or holes in a crystal, the factor is named after the Landé factor computed from g_s and g_L, the spin and orbital contributions respectively. We have g_L=1 while $g_s \approx 2$ according to the Dirac theory of electron. In solid states physics, the quantum states for the charge carriers can be seen as a linear combination of the atomic orbitals from which the band-structure is derived using the Bloch theorem. Thanks to the Wigner-Eckart theorem, a proportionality relation between the magnetic moment and the total angular momentum holds, but the general factor is replaced by an effective Landé factor $g^\star$ encoded in the band-structure of the material. An analogy can be put forward in atomic physics where the Landé factor is not the simple sum of g_s and g_L, but involves the total spin angular momentum and the orbital angular momentum of the atom. The rules of angular momentum coupling and the different g-factors for orbital and spin parts involve a non-trivial relation between these quantities. However, the magnetic moment $\mu = g.\mu_B.\mathbf{J}$ remains proportional to the total angular momentum $\mathbf{J}$ provided an effective g-factor is included in this relation.
In addition, the effective Landé factor is further modified by electron-electron interactions and exchange. Therefore, the experimental determination of the effective Landé factor constitutes a unique probe to address the strength of electronic interactions in various materials. Considering equation 2.64, the energy of the Landau levels are $\epsilon_N = \hbar\omega_c (N + 1/2) \pm \frac{1}{2} g^\star \mu_B B$. The introduction of the Zeeman energy affects the 1/B-periodicity and the amplitude of the Shubnikov-de Haas oscillations, as a result of the superposition of two 1/B-periodic oscillating phenomena with *a priori* different frequencies and phases. For high enough magnetic field ($E_Z > \Gamma$), this effect leads usually in conventional semi-conductor to a frequency doubling. Actually, when analyzing the magneto-resistance fingerprints alone, the experimental extraction of the Zeeman energy is not straightforward and cannot be determined with precision without a dedicated theoretical model. On the other hand, this parameter can be measured accurately by tilting the magnetic field orientation with respect to the sample plane using the so-called "coincidence angle method". Indeed, the energy of the Landau levels, related to the kinetic energy of the charged particles, depends on the perpendicular projection of the magnetic field $B_\perp$ with respect to the 2D plane. On the other hand, the Zeeman energy relates to the total magnetic field B. When the direction of the magnetic field makes an angle θ with respect to the normal to the sample plane, the charged particle energy writes:

$$\epsilon_N = \frac{\hbar q B_\perp}{m^*}\left(N + \frac{1}{2}\right) \pm \frac{1}{2} g^* \mu_B B = \left[\frac{\hbar q \cos(\theta)}{m^*}\left(N + \frac{1}{2}\right) \pm \frac{1}{2} g^* \mu_B\right] \times B \qquad (2.65)$$

When the angle θ is set so that $\frac{N' \hbar q \cos(\theta)}{m^*} = g^* \mu_B$ where $N' \neq 0$ is an integer, equation 2.65 can be factorized in the form $\epsilon_{N,N'} = \hbar\omega_c^\perp (N + 1/2(1 \pm N')) \equiv \hbar\omega_c^\perp N$. This

equation yields similar Landau level energy separation as is the Zeeman contribution was absent, leading to unperturbed 1/B-periodic Shubnikov-de Haas oscillations. Under this condition, the angle θ is coined "coïcidence angle" and corresponds to the constructive superposition of two 1/B-periodic oscillating magneto-resistance phenomena. Once the minimum coincidence angle θ_c is experimentally found for $N' = 1$, the effective Landé factor writes:

$$g^* = \frac{\hbar q \cos(\theta_c)}{\mu_B m^*} = \frac{2m}{m^*} \cos(\theta_c) \tag{2.66}$$

2.2.5 Standard analysis of the Shubnikov-de Haas oscillations

The Shubnikov-de Haas oscillations constitute a unique fingerprint of the associated studied material. The $1/B$-periodic behaviour provides a direct access to the carrier density provided the quantum lifetime is large enough. The carrier density extracted from the Hall effect, on the other hand, is sensitive to all the conduction charge carriers whatever their band mobility. This is the reason why, in some complex multi-band systems, the Hall carrier density is larger than its Shubnikov-de Haas counterpart. Beyond the carrier density, the quantum life time τ_q and the effective mass m^* can be extracted. When the experiment is repeated for various orientation of the magnetic field with respect to its crystallographic axis, one is able to determine the Fermi surface of the material.
Based on equation 6.11 and considering only the first harmonic ($s = 1$), the maxima of the magneto-resistance occur when the argument of the cosine function is minimum, providing the condition $\frac{2\pi hn}{g_s qB} = \pi + 2\pi N$ where N is an integer. When plotted against $1/B$, the magneto-resistance oscillates with a frequency $\omega = hn/2\pi g_s q$, giving access to the carrier density. we can rewrite this condition with an explicit dependence on $1/B$:

$$N = \frac{hn}{g_s q} \times \left(\frac{1}{B}\right) - \frac{1}{2} \tag{2.67}$$

$$\delta N = \frac{hn}{g_s q} \times \left(\frac{1}{B_{(N)}} - \frac{1}{B_{(N-1)}}\right) \tag{2.68}$$

Traditionally, one indexes the maxima of the magneto-resistance with successive integer N and plot them as a function of their corresponding $1/B$ value as shown in figure 2.10. The plot necessarily defines a straight line where the slope equals $\frac{hn}{g_s q}$ from which the carrier density can be extracted. The absolute value of the N indices

can be determined by making sure that $N = -1/2$ when $1/B = 0$, in other words when the Fermi energy is aligned with the zeroth-index Landau level (with infinite degeneracy) for infinite magnetic field.

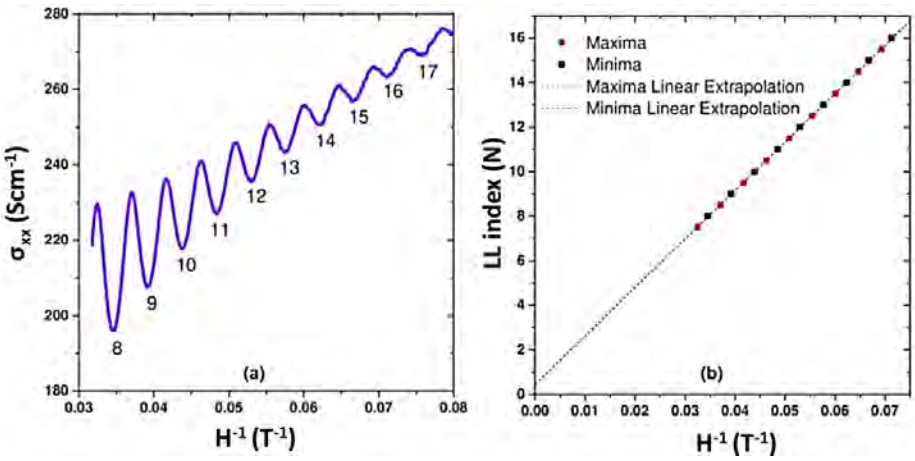

Figure 2.10: (a) Magnetoconductivity oscillations as a function of the inverse of the magnetic field for Sb_2Te_2Se single crystal.(b) Landau levels index for the minima and the maxima of the magnetocondiuctivity. The linear extrapolation of the points crosses the point with the coordinates ($\mathrm{H}^{-1} = 0, N = 0.5$) [71]

Beyond the carrier density, both the effective mass m^* and the quantum lifetime τ_q can be extracted from the measurement of the temperature dependence of the Shubnikov-de Haas oscillations. Indeed, for a given magnetic field, the logarithms of the the amplitude ($A = \rho_{xx}(N) - \rho_{xx}(N - 1/2)$) of the oscillation in the vicinity of a given magnetic field B_N, divided by the temperature simplify greatly using the approximation $\ln(\sinh x) \sim x$ when $x << 1$

$$\ln\left(\frac{A}{T}\right) = \ln\left(\frac{m^*}{nq^2\tau_0} \times 2\exp\left(\frac{-\pi}{\omega_c\tau_q}\right) \times \frac{\frac{2\pi^2 k_B}{\hbar\omega_c}}{\sinh\left(\frac{2\pi^2 k_B T}{\hbar\omega_c}\right)}\right) \tag{2.69}$$

$$\ln\left(\frac{A}{T}\right) = \underbrace{\ln\left[\frac{2m^*}{nq^2\tau_0}\right] + \ln\left[\exp\left(\frac{-\pi}{\omega_c\tau_q}\right)\right] + \ln\left[\frac{2\pi^2 k_B}{\hbar\omega_c}\right]}_{C_1} - \ln\left[\sinh\left(\frac{2\pi^2 k_B T}{\hbar\omega_c}\right)\right] \tag{2.70}$$

$$\ln\left(\frac{A}{T}\right) \approx C_1 - \frac{2\pi^2 k_B T}{\hbar\omega_c} \tag{2.71}$$

where C_1 is independent of the temperature. Thus, by plotting $\ln(A/T)$ against temperature, one obtains a straight line with a slope given by $2\pi^2 k_B m^*/q.B_N.\hbar$, from

which the effective mass can be extracted. Once m^* is known, the broadening of the Landau levels characterized by τ_q can be determined by measuring the amplitude of ρ_{xx} oscillations as a function of the magnetic field, at a given temperature. For this purpose, we compute the quantity $A \times B_N \times \sinh\left(\frac{2\pi^2 k_B m^* T}{qB_N\hbar}\right)$ for several magnetic field B_N before applying the logarithm:

$$A \times B_N \times \sinh\left(\frac{2\pi^2 k_B m^* T}{qB_N\hbar}\right) = \left(\frac{m^*}{nq^2\tau_0} \times 2\exp\left(\frac{-\pi}{\omega_c\tau_q}\right) \times \frac{2\pi^2 k_B m^* T}{q\hbar}\right) \tag{2.72}$$

$$\ln\left[A \times B_N \times \sinh\left(\frac{2\pi^2 k_B m^* T}{qB_N\hbar}\right)\right] = C_2 - \frac{\pi}{\omega_c\tau_q} = C_2 - \frac{m^*\pi}{qB_N\tau_q} \tag{2.73}$$

The plot of $\ln\left[A \times B_N \times \sinh\left(\frac{2\pi^2 k_B m^* T}{qB_N\hbar}\right)\right]$ versus B_N^{-1}, known as the Dingle plot, provides a straight line with slope $\pi m^*/q\tau_q$ from which the quantum lifetime (broadening of the Landau levels) can be extracted.

Chapter 3

Experimental techniques

Contents

3.1 Device fabrication and electrical characterization **45**
3.1.1 From 3D to 2D transition metal dichalcogenides 45
3.1.2 Device processing 48
3.1.3 Thickness determination 55
3.1.4 Electrical characterisation 59
3.2 Measurements in pulsed magnetic field and low temperature . . **65**
3.2.1 Pulsed magnetic field generation 65
3.2.2 Cryogenics 66
3.2.3 Insert and sample holder 67
3.2.4 Data acquisition and induced voltage removal 68

3.1 Device fabrication and electrical characterization

3.1.1 From 3D to 2D transition metal dichalcogenides

Thin flakes of TMDCs can be fabricated using two approaches. The top-down approach consists of thinning a bulk material down to a few atomic layers only. For exfoliable materials such as WSe_2, this hand-made technique is cheap and easy but requires long experience and special know-how. It produces high-quality 2D-systems (depending on the quality of the mother bulk crystal) with an overall size limited to a few tens of micrometers in length and width. On the other hand, the bottom-up approach consists in fabricating the desired material from its initial building blocks (e.g. atoms or molecules). The dedicated techniques for TMDCs are the Chemical Vapour Deposition (CVD) and the Molecular Beam Epitaxy (MBE) [76, 77]. The work in this thesis is only focused on the fabrication technique using the top-down approach.

Controlled layer stacking using the dry transfer technique

The objective is to fabricate a structure with a monolayer WSe_2 flake deposited on top of a larger hexagonal boron nitride (h-BN) flake. This system must be connected to several metallic electrodes for electrical transport measurements. Alternative systems where the WSe_2 monolayer is sandwiched between two larger h-BN flakes display much higher quality in terms of electronic mobility, but the electrical addressing process

remains technologically very challenging. h-BN is an ideal template for electronics based on 2D exfoliable materials, owing to its unique properties as a dielectric film [72]. It consists of alternating boron and nitrogen atoms in a honeycomb lattice with strong in-plane covalent bonding, while the atomic planes are stacked upon each other and interact via weak van der Waals forces. Even when thinned down to a few atomic layers, this material remains a wide band-gap insulator ($5.5 - 6\ eV$). It is chemically inert without any dangling bonds or charged traps [58] and stays flat when deposited on a substrate. Compared to a sample made of WSe_2 lying directly on a silicon oxide substrate, the use of h-BN few layers as a buffer layer (below the WSe_2 flake, or both below and above) improves the electronic mobility by several orders of magnitude for the following reasons: (i) The in-plane lattice parameter of h-BN (0.25 nm) matches closely the WSe_2 one, allowing material stress reduction [103] ; (ii) When the bottom h-BN flake is fairly thick ($\sim$ 20 nm), it conforms to the underlying Silicon dioxide (SiO_2) substrate and attenuates the height variations at the atomic scale. The WSe_2 flake can, therefore, be deposited on an atomically flat surface ; (iii) The large h-BN dielectric constant reduces the interaction with trapped charges in SiO_2 substrate. (Where its value in the bulk case $\varepsilon_{h-BN} = 3.8$ [78]) and (iv) h-BN shows remarkable chemical and thermal stability with high impermeability to gas and liquids [108, 102].

Substrate preparation

First, we deposit h-BN few-layer flakes randomly on a standard Si/SiO_2 substrate with d_{SiO_2}=300 nm. For this purpose, we start by cutting a small piece of **PDMS** film (Polydimethylsiloxane belongs to a group of polymeric organo-silicon compounds that are commonly referred to as silicones), purchased from Gel Pak, and we put it on a microscope glass slide. Next, we exfoliate several times the h-BN commercial bulk crystal, purchased from hq graphene company with a piece of adhesive tape. The adhesive tape is pressed gently against the PDMS, and peeled off smoothly. Some h-BN thin flakes are randomly transferred from the adhesive tape to the PDMS surface. Finally, we put the PDMS into contact with the Si/SiO_2 substrate. The use of PDMS as an intermediate step allows for a clean transfer of a few h-BN flakes with different thicknesses and sizes, well isolated from each others, onto the Si/SiO_2 substrate. Referring to contrast obtained using optical microscope (Huvitz HRM300-model) with 100x objective, we search for the most ideal h-BN thin flakes transferred into the substrate in terms of lateral size, flatness, thickness (maximum 30 nm) and surrounding free space. Figure 3.1 shows different h-BN flakes using this process. Usually, the color of the flake gives an idea about the thickness which varies from blue to green, yellow and reddish. When necessary, AFM measurements are performed to determine precisely the thickness.

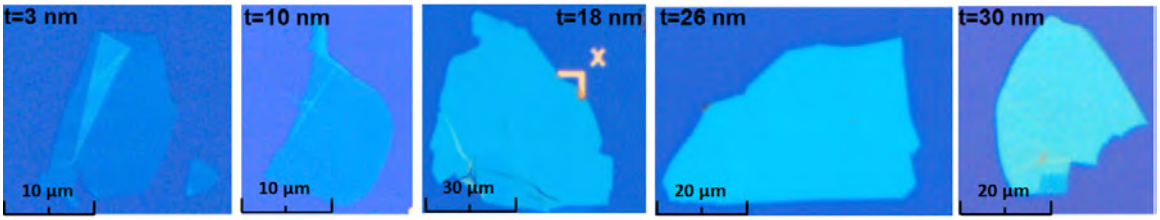

Figure 3.1: Optical microscopy photos for different exfoliated h-BN flakes, the thickness **t** is determined using AFM

2H-WSe_2 exfoliation and precise deposition onto a h-BN flake

Commercial bulk WSe_2 crystals purchased from 2D semi-conductor company are processed in the same way as detailed earlier. However, a monolayer WSe_2 flake is selected right after its deposition on the glass/PDMS system. Later, we shall deposit this flake exactly on top of the h-BN flake using a set of precision moving stages purchased from Thorlabs/RB13M/M. This method is referred to as the dry transfer technique illustrated in figure 6.9. For higher accuracy, the h-BN/SiO_2/Si substrate is itself hold on another precision X-Y stage purchased from Thorlabs/XYR1/M. The WSe_2/PDMS system is aligned with the h-BN/SiO_2/Si substrate under the objective of a microscope. The optical transparency of the PDMS and glass slide allows the visualization of both the WSe_2 and h-BN flakes by paying with the microscope focus. Once the desired alignment is reached as shown in figure 3.3, the two flakes are pressed against each other. We note that the optical colors change when the PDMS stamp touches the Si/SiO_2 wafer. Finally, we peel off the stamp slowly in order to avoid to break the stack. Most of he time, the WSe_2 flake detach from the PDMS and remains stacked on its BN counterpart.

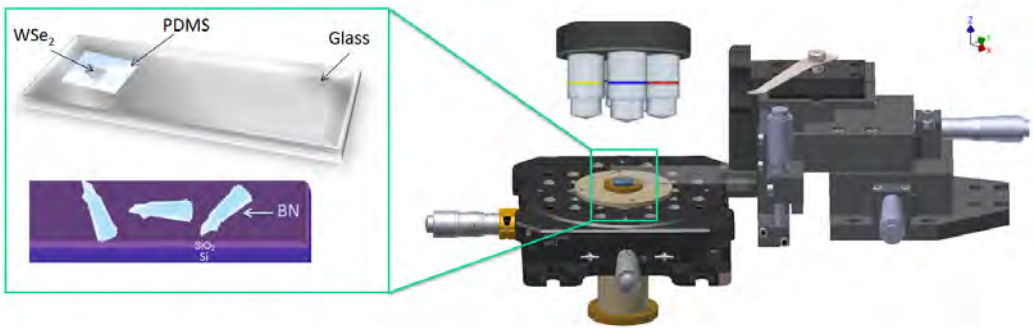

Figure 3.2: Micro-alignment setup and precision movable stage under optical microscope

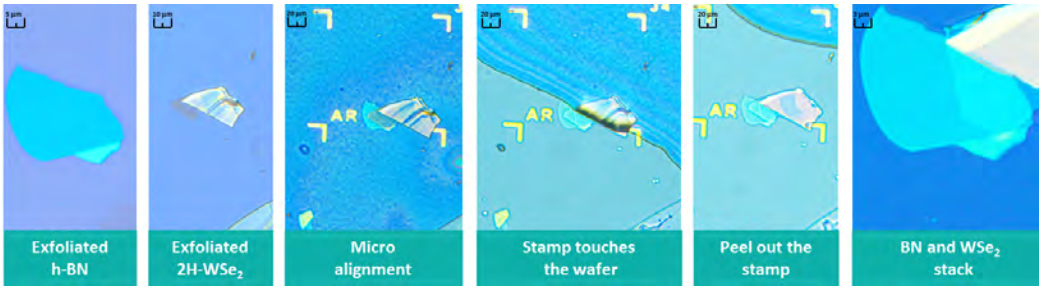

Figure 3.3: Different steps for stacking exfoliated h-BN and WSe_2 using the dry transfer technique

3.1.2 Device processing

The samples were fabricated partly at LNCMI for exfoliation and localization ; partly at the AIME clean room facility of the INSA campus for chemistry processes, electron beam lithography and dicing and partly at LPCNO for metal evaporation and sputtering as well as plasma etching. Figure 3.4 represents the flowchart for major processes, each of them will be described in details.

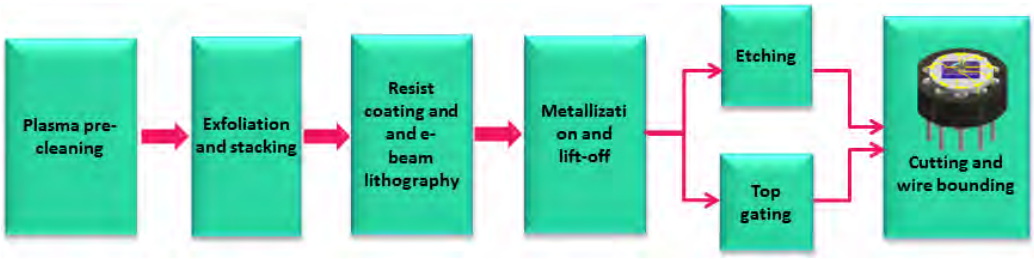

Figure 3.4: Basic fabrication process of FET based on TMDCs materials

Cleaning of Si/SiO_2 substrates

We use p-doped Si/SiO_2 square substrates with lateral size 1 cm, having an alphanumeric grid performed by standard optical lithography. The thickness of the silicon oxide is 300 nm. The LAAS laboratory and AIME clean-room facility provide us with such substrates with a resist protective layer. Most of the resist is removed when rinsing the substrate in high purity acetone, but a thin film resist usually remains. At this stage, more sophisticated methods are used to remove the residues starting from the least to the most aggressive ones to preserve at maximum the oxide layer. For instance, hot acetone and/or sonication are proven very useful. At last resort, we use oxygen plasma cleaning method with very low power and very limited exposure time (1s at 10W Radio Frequency (RF) power).

e-beam lithography

Most of the time, WSe_2 flakes of interest have lateral size of the order of a few micrometers, and can be localized anywhere on the substrate. Therefore, electron-beam lithography presents a special interest in making the electrical contacts at the micro/nano-meter scale. This technique developed in the 1960's, focuses an electron beam at the desired place on a substrate. When striking a thin polymethyl methacrylate (PMMA) resist with an energetic beam of electrons, the long-chain polymers are fragmented. When the substrate is later plunged in a dissolving solution, the exposed spots are removed much faster than the pristine (nor exposed) PMMA resist.

During this work, we used 2 different types of PMMA resists with different molecular weight with two different concentrations of solvants (anisole), namely PMMA-495/A3 and PMMA-950/A2. The lower molecular weight resist is more sensitive compared to its high molecular weigth counterpart, so that it enhances the undercut profile when used a the bottom layer. The coating was performed using a resist spinner system shown in figure 3.5. The recipe depends on the size of the electrodes. We distinguish the micro-electrodes, which are connecting directly the WSe_2 flake with high precision, from the macro-electrodes which spread over a few mm^2 and are used for electrical interconnection purposes.

Figure 3.5: The resist spinner system. The wafer is maintained onto a chuck with vacuum. The resist is dispensed at the center of the wafer just before spinning.

- Micro-electrodes: we start by spin-coating the PMMA-495/A3 with a rotation speed equal to 2000 rpm. We bake it for 1 minute before deposing another layer of PMMA-950/A2 with a rotation speed of 3000 rpm. We bake the substrate again for 1 minute. Finally, we end up with a total PMMA thikness of 180 nm.

- Macro-electrodes: we start by spin-coating the PMMA-495/A8 with a rotation speed equal to 3000 rpm. We bake it for 1 minute before deposing another layer of PMMA-950/A2 with a rotation speed of 3000 rpm. We bake the substrate again for 1 minute. We end up with a total resist thickness of the order of 520 nm.

Since each sample is different from one another, the electron beam lithography process uses unique drawings for the micro-electrodes. On the other hand, a template was used for the macro-electrodes. We use AutoCAD and kLayout softwares to design the electrodes. AutoCAD was used to design and set the macro-electrodes and the

micro-electrodes into two separate layers in order to facilitate the exposure steps (see figure 6.10). The alignment marks are drawn on the corners of each working area for precision electron beam adjustment. The AutoCAD .dwg file format was first converted into the .dxf format. This file was then imported into klayout software and later saved in the .GDS format compatible with the electron beam lithography machine.

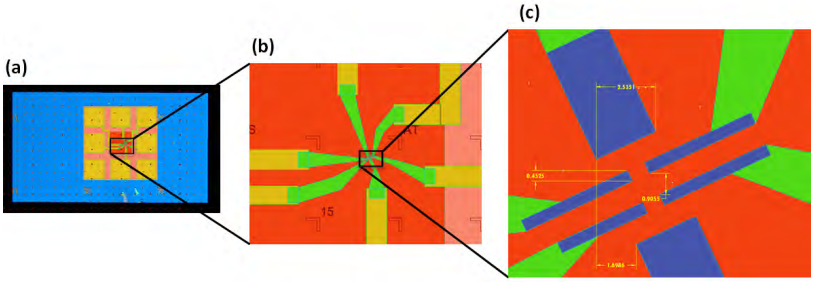

Figure 3.6: AutoCAD design for a) macro-electrodes and b) micro-electrodes. c) Hall bar dimension and typical distance between the micro electrodes

Once the resist is spin-coated and the drawings are ready, the sample is inserted into a scanning electron microscope upgraded with an electron beam lithography module. After a few alignment and focus procedures, the sample is exposed following the desired drawings where the magnification, the beam current and the area step size defines the correct electron dose. After exposure, we use a MIBK solution (1:2 solution of (4-methyl-2-pentanone):(2-propanol)) as a developer for removing the exposed parts of the PMMA resist. The development process lasts exactly for 30s. Figures 3.7-a & 3.7-b left panels show the micro and macro-electrodes pattern after exposure and development.

Parameters	**Micro-electrodes**	**Macro-electrodes**
Write field size (μm)	250	800
Min step size (μm)	0.0040	0.0130
Beam current (nA)	0.1	6
Area step size (μm)	0.0080	0.0780
Area line spacing (μm)	0.0080	0.0780
Area dwell time (ms)	0.001250	0.002000
Area dose ($\mu C/cm^2$)	195.315200	197.238659
beam speed (mm/s)	6.4000256	39.0001560

Table 3.1: Pattern parameters for micro and macro-electrodes.

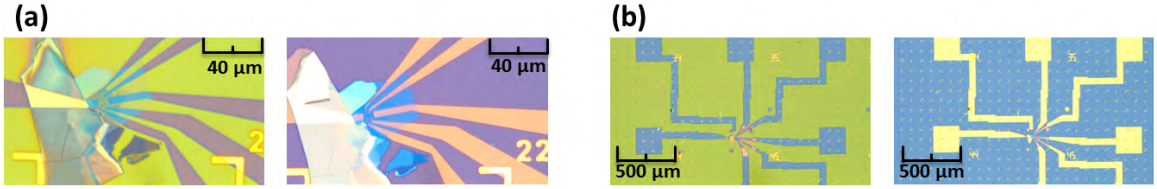

Figure 3.7: (a) Optical miscroscope image of micro-electrodes after left: MIBK development, right: metalization and lift-off. (b) Optical miscroscope image of macro-electrodes after left: MIBK development, right: metalization and lift-off.

Metalization and lift-off

Once the PMMA resist has been developed, the sample is ready for metalization. The metal must satisfy certain conditions such as low electrical resistance, good adhesion to the top of the surface and non-oxydable. The technique of deposition depends on the required thickness and suitability for lift-off. For this purpose, we deposit a metalic bilayer made of platinum (Pt) and gold (Au) for the micro-electrodes, whereas titanium (Ti) and gold are used for the macro-electrodes.

- Sputtering deposition: this technique consists of dispersing atoms on the sample originating from a bulk target containing the desired metal which is electrically grounded and serves as a cathode. Argon gas is introduced into the chamber at low pressure and ionised into positive ions (plasma) with RF frequency excitation. The ions are accelerated toward the cathode and act as a milling tool which disperse the metallic atoms to be deposited. This technique allows uniform and high quality metal films; but is not suited for lift-off unless the thickness of deposited metal is very small compared to the PMMA thickness. For the deposition of 10 nm of platinium, the flow of argon gas is 30 sccm ((cm^3/min) and the polarization voltage is set to 330V for 2 min and 50 s. For the deposition of 10 nm of titanium, the argon gas flow is 30 sccm and the polarization voltage is set to 263V for 7 min and 40s.

- Vacuum evaporation: A metal is heated under vacuum by passing a high current in a tungsten filament wrapped around. The metal source undergoes a phase transition from solid to liquid, and then from liquid to gas when the temperature is further raised. The evaporated atoms form a thin layer on the wafer held as far as possible from the source to avoid sample heating. The evaporation technique is directional and fits well the subsequent lift-off process. The gold was used in this thesis, the thickness of the evaporated gold is 30 nm for micro-electrodes and around 150 nm for macro-electrodes under a current equal to 250 A, with

a flux ratio of 0.20 nm/s.

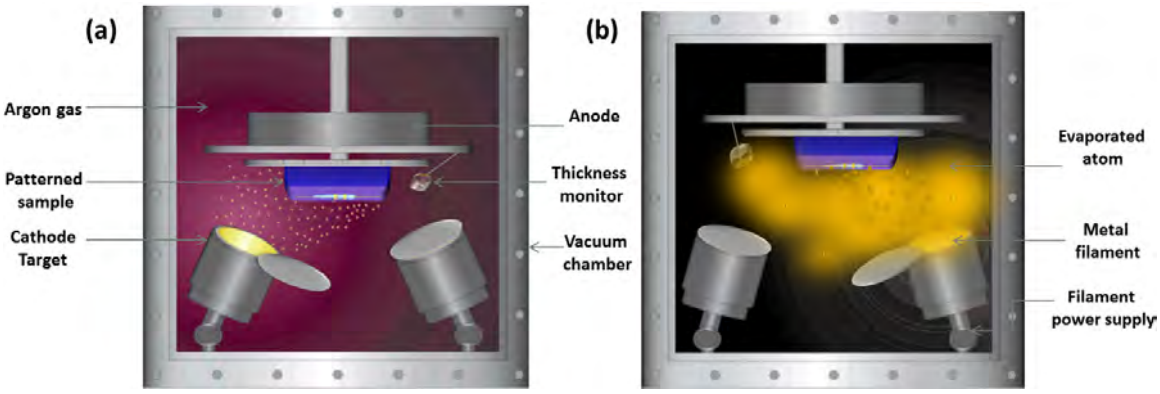

Figure 3.8: (a) Schematic representation for a sputtering process, which encloses the target, the sample holder, the ionised argon gas and the thickness monitor. (b) Evaporation source including the evaporation source, a sample holder and a tungsten filament for Joule heating.

Etching

The etching is a delicate process where numerous parameters have to be properly calibrated. Several etching techniques can be used such as dry etching, wet etching and sputter etching. In this thesis, some samples were etch before the fabrication of the electrodes for obtaining a well-shaped Hall bar geometry. We used the plasma etching technique represented in figure 3.10. The sample is first covered by PMMA resist except the parts to be etched which are removed using electron beam lithography.

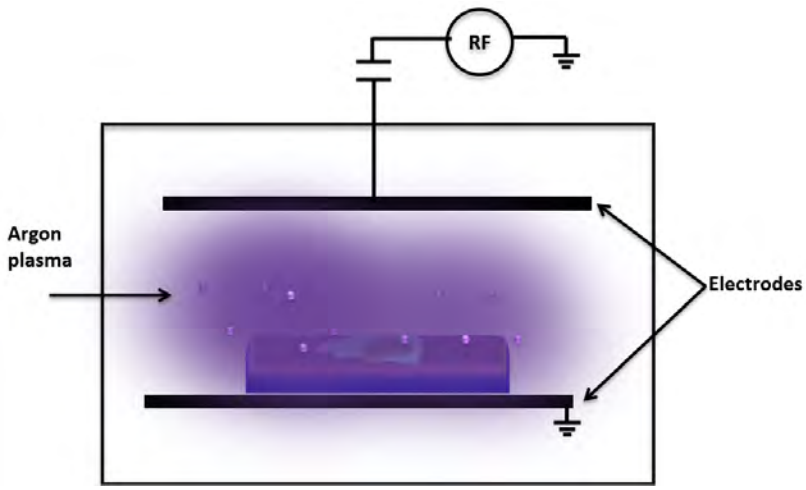

Figure 3.9: A plasma etching planar system. The plasma consists of oxygen ions accelerated toward the wafer and thus impinging the material to be etched.

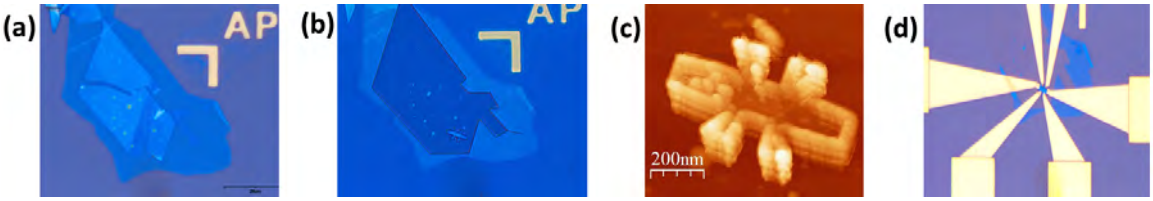

Figure 3.10: (a) WSe_2/h-BN stack before etching. (b) A Hall bar etched device with the parameter shown in table 3.2. (c) Image of an atomic force microscopy (AFM) for Hall bar etched device. (d) Etched Hall bar device addressed using classical techniques of e-beam lithography and metal evaporation.

With the etching parameters mentioned in 3.2, we found out that 90 nm of the resist was removed. This is usually more than enough to fully remove the unwanted multi-layer material attached to a WSe_2 monolayer flake of interest.

Parameters	**Values**
Plasma gas	Argon
Exposure time (min)	8
Power (W)	100
Ar pressure (mTorr)	5
Ar flow (sccm)	31.4
DC bias (V)	460

Table 3.2: Etching parameters.

Full encapsulation and top gating

Some of the samples fabricated during this thesis were fully encapsulated using h-BN flakes. In other words, a WSe_2 flake is sandwiched between two h-BN flakes so that both sides are protected from its direct environment. In case a metallic electrode is fabricated on top of the overall structure, so that the top h-BN flake acts as a top-gate dielectric, one must consider the following criteria for the choice of the top h-BN flake: (i) it should be large enough to cover all the fabricated electrodes to avoid possible short circuit (see figure 3.10-b), (ii) its thickness should be of the order of $\sim$ 20 nm to provide a gate voltage range between -10V and +10V without breaking. Thicker flakes may not be compatible with the fabrication of of the gate electrode, since the step is too high for the continuity of the metal electrodes.

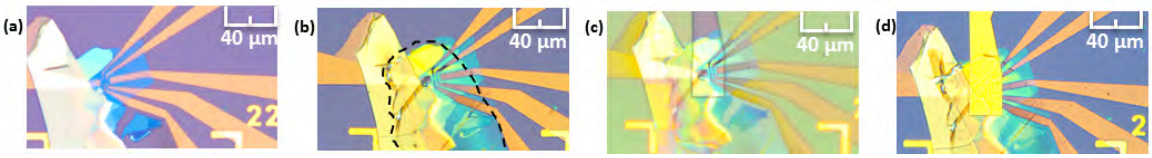

Figure 3.11: (a) h-BN/WSe_2 electrically contacted device. (b) Full encapsulation with h-BN. (c) Electron beam lithography pattern for the top gate electrode. (d) Top gate metalization.

After top h-BN deposition, the top-gate electrode (see figures 3.11 c & d) is fabricated by sputtering a 10 nm of titanium and evaporation of 60 nm of gold.

Dicing and wire bonding

At the beginning of the sample fabrication process, the Si/SiO_2 substrate is a square of 1 cm for the lateral dimensions and 500 μm for the thickness. These dimensions ensure a large enough area to search for ideal monolayer TMDCs flakes and for the spin-deposition of resist with homogeneous thickness. It is also easily to manipulate and fits most of the clean room chuck standards. However, the sample must be reduced to a square of about 3 mm in size to fit high magnetic field insert (see section 3.2.4). For this purpose, we cover the sample within a layer of PMMA (to protect the fabricated device) and we us a dicing machine equipped with a highly accurate blade as illustrated in figure 3.12-a.

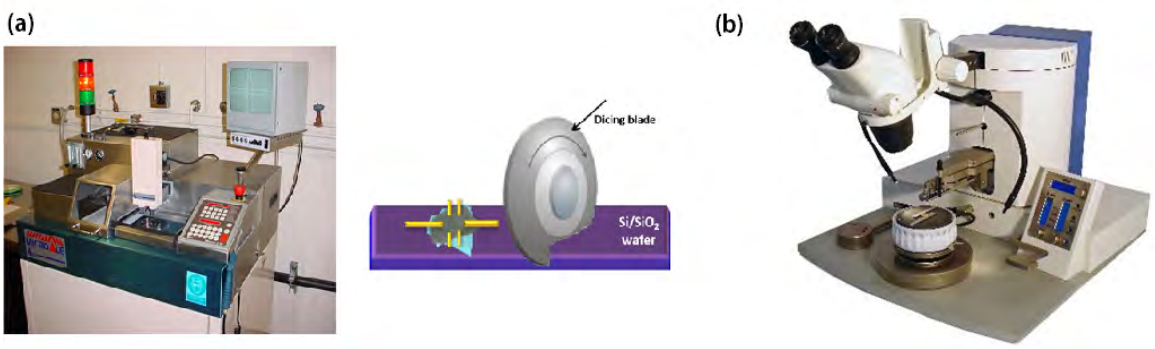

Figure 3.12: (a) Left: photograph of dicing machine available at the clean room facility AIME. Right: Dicing of the wafer with an accurate blade. (b) Photograph of the wire bonding machine used during this work.

For connecting the macro-electrodes of the sample to a larger connector, we use a wire bonding machine as shown in figure 3.12-b. A gold wire with a diameter of 10 μm is

pressed against the sample's electrode while a pulse of ultra-sounds melts the metal locally and ensure a good electrical contact. The process is repeated to the connector pad and then cut. Wire bonding is risky and may damage the SiO_2 dielectric if the parameters are not properly adjusted. The thickness of the metallic electrodes is also an important criterion for successful wedge-bonding.

3.1.3 Thickness determination

The physical properties of TMDCs are ultimately related to the number and parity of the layers, as explained in chapter 1. The number of layers can be determined using several methods such as optical microscopy, atomic force microscopy, photoluminescence, Raman spectroscopy and transmission electron microscopy.

Optical microscopy

Optical microscopy constitutes the simplest way to estimate the number of layers, from 1 to 3 at best. It is a non-destructive method, based on optical constrast, which is widely used for TMDCs materials.

The image contrast between 2D materials and the rest of the substrate under visible light originates from integrated contrasts of each wavelength component [80]. The method can be improved using a narrow-band illumination and the selection of appropriate substrates [74, 75]. With the emergence of machine learning algorithms in image analysis, the identification of 2D materials based on their number of layers becomes viable [79] as shown in figure 3.13 with recognition and topography of a MoS_2 exfoliated flake.

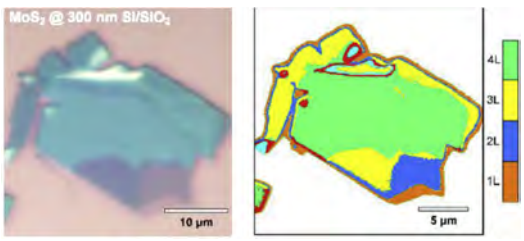

Figure 3.13: Left:Optical image of MoS2 under white illumination. Right:thickness determination based on optical contrast and artificial intelligence. Adapted from [80]

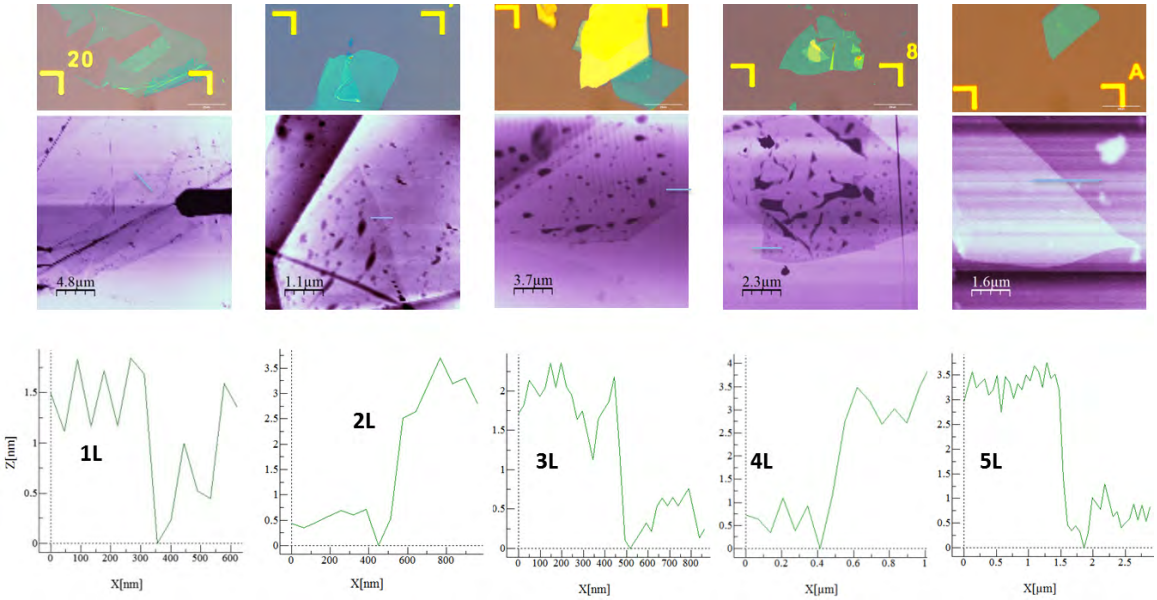

Figure 3.14: Top: Exfoliated WSe_2 flakes with different thicknesses. Middle: thickness determination using AFM. Bottom: height profile obtained from AFM measurements.

Atomic force microscopy

Atomic force microscopy was used to determine the thickness of 2D materials. The thickness of a TMDCs monolayer is of the order of 0.7 nm (depending on the nature of the substrate on which it is deposited) which corresponds to the interlayer distance between X-T-X bonds [81]. The AFM used here is **Nano-R**^{TM} from Pacific Nanotechnology, as illustrated in figure 6.11.

The imaging mode used is the tapping mode. Figure 3.14 shows AFM micrographs for different exfoliated flakes of WSe_2 with different thicknesses. For proper measurements, the scan size was 4 μm with 512 pixels resolution. The software WSxM was used for image processing. Surface contamination and water adsorption prevent a reliable determination of the number of layers. When the AFM imaging parameters are not properly set, the tapping mode damages the surface of the flakes. For this reason, optical spectroscopy techniques detailed in the next paragraphs are prefered.

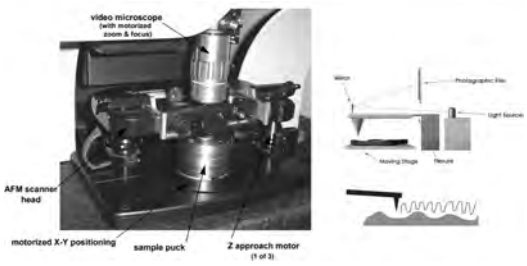

Figure 3.15: AFM for thickness determination with an illustration of the tapping mode.

Photo-luminescence

Photoluminescence (PL) is a very efficient technique to distinguish monolayer TMDCs. It is sensitive to the indirect to direct bandgap transition in monolayer TMDCs [82].

The PL intensity is very weak for indirect bandgap materials since it relies on a phonon-assisted process with low quantum yield. On the other hand, the PL response is high for monolayer TMDCs, which is a signature of a direct bandgap semi-conductor [44, 7].

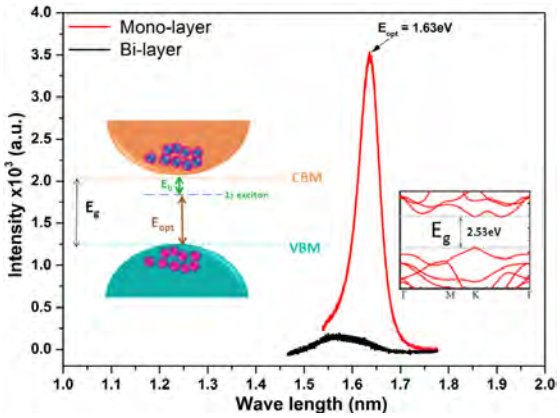

Figure 3.16: Room temperature PL spectrum for mono- and bi-layer WSe_2 exfoliated flakes on Si/SiO_2 substrate. The left inset represents the difference between optical and electrical bandgap. The right inset shows the calculated band structure of monolayer obtained from [88].

A PL emission peak at 1.63 eV was reported in references [45, 87, 51] in line with the PL measurements of our monolayer WSe_2 samples performed at CEMES laboratory in collaboration with P. Puech (see figure 3.16). The excitonic binding energy is 0.9 eV [87]. By adding the emission peak energy and the excitonic binding energy, one obtains the electronic energy gap which is equal to 2.53 eV. PL constitutes a powerful and non-invasive technique to determine monolayer flakes without any doubt. However, it is not possible to distinguish bi-layer from other multi-layer TMDCs flakes.

Raman spectroscopy

Raman spectroscopy is a powerful and non-destructive characterization tool to study 2D materials. Discovered in 1928 by Raman, this technique is based on changes in optical frequency when light is scattered by atoms or molecules into motion [90]. As a result, the photon may gain (lose) energy and we observe a Stockes (anti-Stockes) shift [85] of the frequency of the incident light. In the following, we will discuss the Raman spectra for WSe_2 flakes on Si/SiO_2 substrates. The Raman spectra are measured in collaboration with P. Puech in the CEMES laboratory, using a microscope fitted with a 40x objective and a laser excitation wavelength of 633 nm with 0.7mW power at room temperature.

Even though group theory predicts that 4 vibrational modes are Raman active, only the E^1_{2g} and A_{1g} modes are accessible by experiments. Each Raman spectra acquired 2 peaks associated to E^1_{2g} and A_{1g} vibrational modes, consistent with the phonon dispersion. The monolayer features E^1_{2g} and A_{1g} modes take values at 375 cm^{-1} and 395 cm^{-1} respectively, with frequency difference between the peak < 21.2 cm^{-1} as shown in figure 3.17. The Raman peak separation increases with increasing number of layers, and the E^1_{2g} mode is found to red-shift while the A_{1g} is found to blue-shift as we increase the layer thickness, in consistency with [86]. The frequency difference of the 2 measured modes E^1_{2g} and A_{1g} is small (> 2 cm^{-1}) between mono- and bi-layer rendering the thickness identification rather challenging.

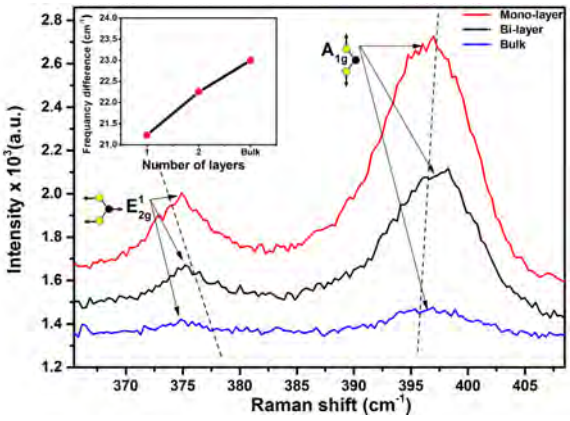

Figure 3.17: Raman spectra of mono-, bi-layer and bulk WSe_2 measured using a 633 nm excitation wavelength. Prominent peaks emerge at ~ 375 cm^{-1} and $\sim 395cm^{-1}$ corresponding to E^1_{2g} and A_{1g} modes. Inset: E^1_{2g}, A_{1g} modes frequency difference as a function of the number of layers.

Structural characterisation

The thickness determination can be performed by a direct observation of the sample using a transmission electron microscopy. This study was performed in collaboration with Bénédictde Warrot-Fonrose from the CEMES laboratory. This technique is destructive and is always performed after measuring the samples.

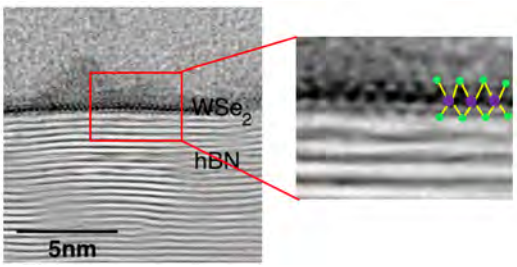

Figure 3.18: Bright Field Scanning Transmission Electron Microscopy (BF-STEM) on which the h-BN substrate appears as dark/bright fringes whereas the WSe_2 layer consists of dark spots surrounded by brighter ones. The inter-atomic distance between W and Se atoms correspond to the expected ones. The WSe_2 layer is continuous and reproduces the top surface of h-BN stack.

Transmission electron microscopy requires specific sample preparation to get electron transparent lamellae. These lamellae are realized with a Focused ion Beam (FIB) machine using the lift-out technique that allows having the least damage of the sample and the best atomic resolution. The whole process was achieved in a FEI Helios NanoLab 600i. A protection layer was deposited on top of the sample surface with ion beam platinum deposition assisted by a gas injection system (GIS). The thickness of the lamella is monitored by electron imaging at 2 kV [96, 97].

3.1.4 Electrical characterisation

Basic transport properties such as carrier density and electronic mobility can be obtained by measuring the current as a function of the gate voltage or the drain-source (bias) voltage [91]. We distinguish two measurement configurations: (i) A bias voltage is applied between the two ends of the sample while the current passing through is recorded using a low noise current preamplifier. The ratio of the measured current over the applied bias voltage provides the two probe conductance, which includes the resistances of the drain and source contacts. This method is particularly well suited for devices with large intrinsic resistance, so that the contact resistances become negligible. (ii) A current is forced to circulate through the device while the voltage difference between another two electrodes is recorded using a high resistance instrumentation amplifier. The ratio between the imposed current and the recorded voltage provides the four-probe conductance. Here, the contact resistances do not contribute since no current passes through the voltage electrodes. This method is well adapted to systems having a resistance much smaller than the amplifier input resistance. In both cases, the back-gate voltage can also be varied, allowing a measurement of the trans conductance $G_{(V_g)}$ for linear I-V characteristics, or the differential conductance $dI/dV_{bias}(V_g)$ at a given bias voltage when the I-V curve is non-linear.

Schottky barrier

When an electrical contact is achieved between a metal and a semi-conductor, a Schottky barrier is established. Near the interface, a transfer of charges occurs until the Fermi energy is the same in both materials. This effect goes hand in hand with the formation of a varying electrostatic potential across the junction. The exact charge distribution and potential profile requires solving the Poisson equation iteratively until the Fermi energy of both materials are aligned. A local modification of the extrema of the conduction and valence bands follows, with the creation of a potential barrier. The work function of platinum is 6 eV [94] while the valence band edge of WSe_2 is located about 5.5 eV [95] from the vacuum level. When into electrical contact, the WSe_2 band bending is at the origin of the Schottky barrier.

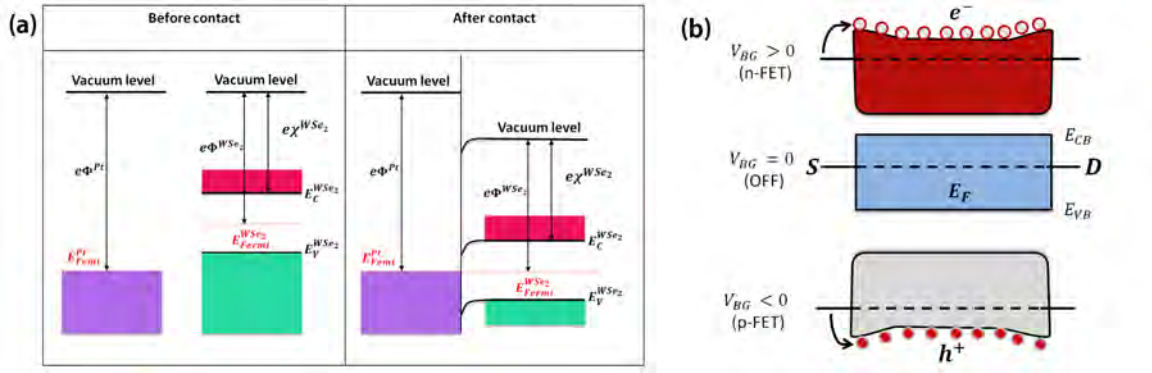

Figure 3.19: a) Illustration of band bending at the interface between a metal (Pt) and p-doped semi-conductor (SC) (WSe_2) and the formation of a Schottky barrier. b) Band diagrams representation for TMDCs FET at $V_D = 0$ for $V_{BG} >, =$ and < 0 [92].

Since the Fermi energy lies in the band-gap of WSe_2, the system is an insulator. When a negative back-gate voltage is applied to the gate electrode, the electro-chemical potential of the charge carriers in WSe_2 is modified which results in decreasing the Schottky barrier as the Fermi energy approaches the valence band maximum. For high enough (negative) back-gate voltage, the Fermi energy is close enough to the valence band edge and a current can pass through the device. On the other hand, when a positive back-gate voltage is applied to the gate electrode, electrons should be able to carry the current when the Fermi energy is close to the conduction band edge. Nevertheless, the minimum back-gate voltage required to achieve electron conduction is out of experimental reach (> 110 V). This process is illustrated in figure 3.19-b. When the Fermi energy is set close the valence band maximum (but remains inside the band-gap), some charge carriers may have enough thermal energy to overpass the barrier or to tunnel through it, resulting in a measurable net current. The current increases rapidly as the drain-source voltage becomes large enough as shown in figure 6.13. When the back-gate voltage is small (e.g. from 0 to -45V), the current is null for the explored range of bias voltage at $T = 4.2$ K. For $V_g > 60$ V, a small current can be measured only when the bias voltage is large enough, rendering a strongly non-linear I-V curve. The non-linearity tends to vanish as the back-gate voltage approaches V_{BG} = -90 V and eventually disappear if the Fermi energy is further pushed inside the valence band. Figure 6.13-b is an alternative representation of this effect, where the current I_D is displayed as a function of both the bias voltage and the back-gate voltage in a color map. The field effect mobility μ_{FE} can be extracted using the formula [14]:

$$\mu_{FE} = \frac{1}{C_{BG}} \frac{L}{W} \frac{dG}{dV_{BG}} \tag{3.1}$$

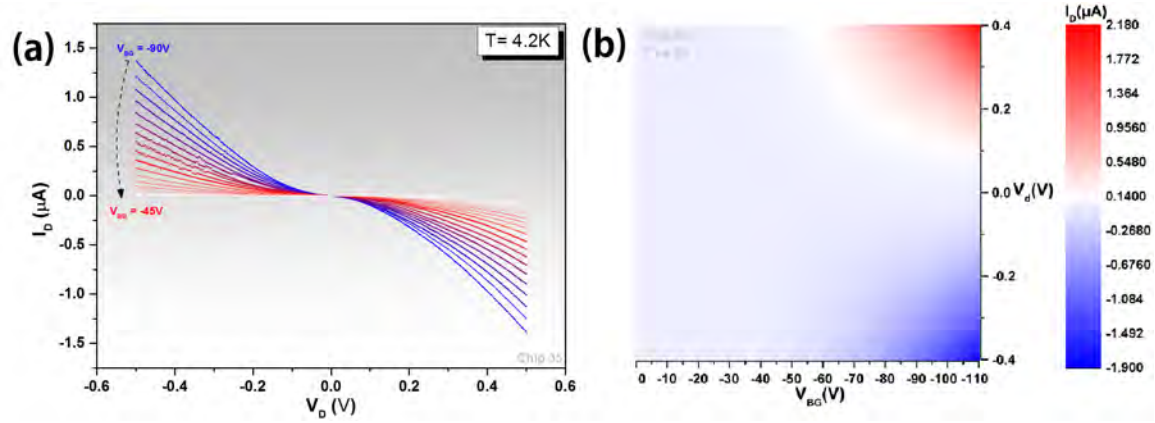

Figure 3.20: a)Drain-source current for various values of the back-gate voltage from −45 V to −90 V by steps of −2.5 V in a multi-layer WSe_2 field effect transistor at T=4.2K.b)V_{xx} vs V_{BG} at various V_D at T = 4.2K in a monolayer WSe_2 FET

where C_{BG} = 11.4 nF.cm^{-2} is the back-gate capacitance for two layers of SiO_2 (300 nm,$\epsilon_r^{SiO_2} = 3.9$) and h-BN (20 nm, $\epsilon_r^{h-BN} = 3.8$)

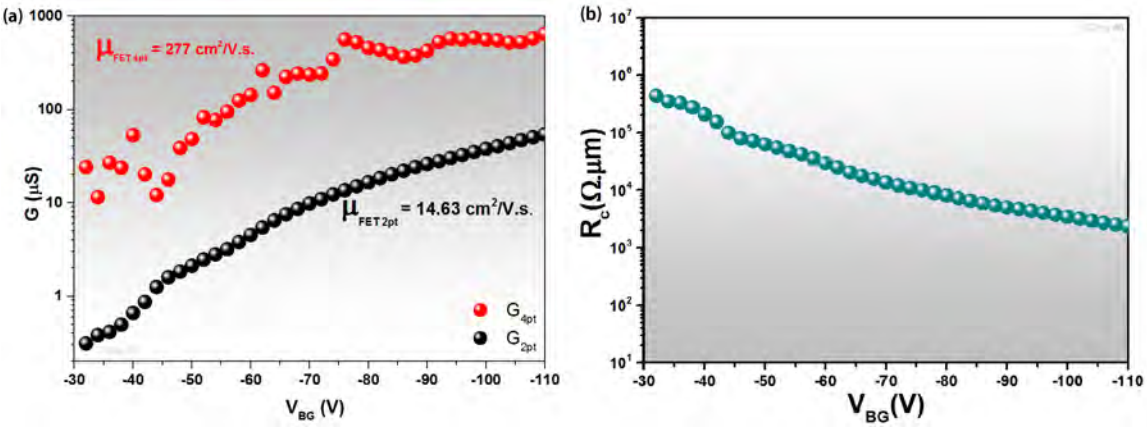

Figure 3.21: (a) Two-probe and four-probe conductance at room temperature as a function of the back-gate voltage, from which the corresponding field effect mobility is extracted. (b) Strong variation of the contact resistance as a function of the back-voltage

From the results displayed in figure 3.21-a, we extract μ_{2p} = 14 cm^2/Vs and μ_{4p} = 277 cm^2/Vs at room temperature for a monolayer WSe_2 sample(chip 46) in line with previous published reports [92, 14, 93]. The field effect mobility extracted from the two-probe conductance provides a lower bound of the intrinsic conductance since it includes large contact resistances shown in figure 3.21-b. The mean resistance per

contact is calculated using the relation $R_c = \frac{W}{2}\left(\left(\frac{1}{G_{2pt}} - \frac{1}{G_{4pt}}\right)\right)$. At room temperature, a large hysteretic behavior is observed when the back-gate voltage increases and decreases, as shown in figure 3.23-a. This behaviour tends to vanish as the temperature is lowered as shown in Fig. 3.23-b. This effect is due to molecules (such as water of oxygen) adsorbed at the surface of the device, as well as the presence of charge traps close to the interface between WSe_2 and SiO_2 as reported in [100, 99, 98].

Effect of Dual Gating

The top-gate provides another knob to tune the charge carrier in a few-layer WSe_2 FET channel, and therefore the FET characteristics. The stark difference of applying both a V_{TG} and a V_{BG} in the same time can be understood by examining the electrical field distribution in the device. Fig. 3.22 shows G_{2pt} vs (V_{BG} and V_{TG}) measured at T=4.2K.

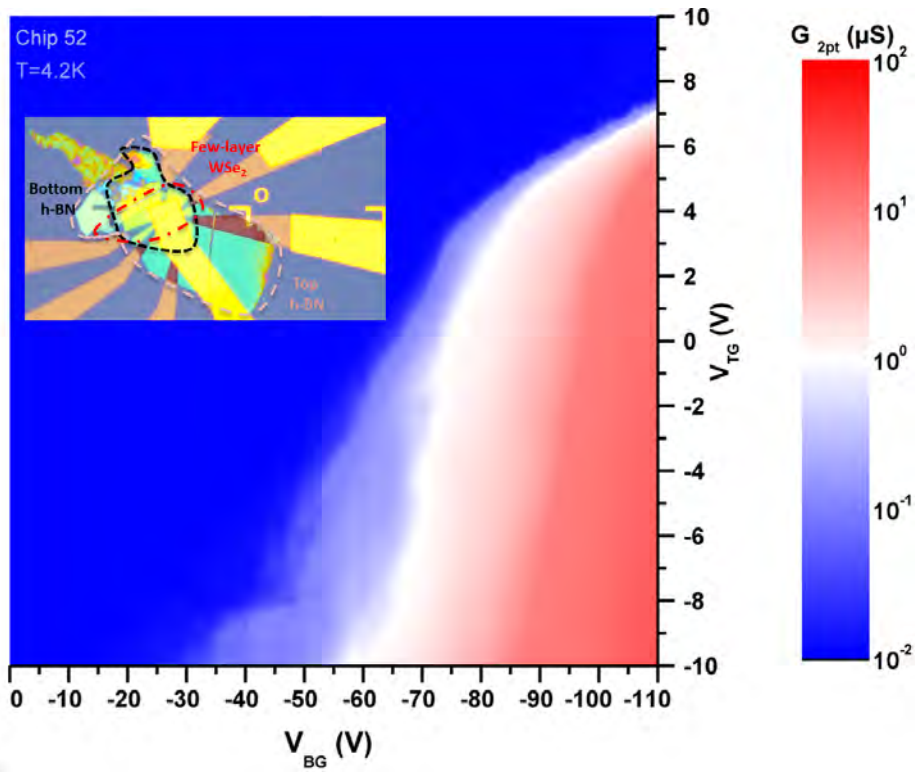

Figure 3.22: G_{2pt} **vs** (V_{BG} and V_{TG}) varying from 0 to -110V and from -10V to 10V respectively at T=4.2K. The inset represents the connected and top-gated chip 52. The edge of the bottom h-BN, the WSe_2 multi-layer and the top h-BN are limited with dashed lines.

The back-gate can tune the carrier density both in the channel and on the back of the

contacts, while the top-gate can only modulate the WSe_2 channel but not the contact regions due to the screening by the contacts. Therefore, transfer characteristics are contact resistance limited, especially at low $|V_{BG}|$. The G_{2pt} saturation is due to the contact resistance. Since the contact resistance can be modulated much more effectively using V_{BG}, G_{2pt} in the ON state is more sensitive to the V_{BG}. The shift in the V_{BG} at the onset of saturation with varying the V_{TG} values is due to the dual-gating of the channel. A more negative V_{BG} accumulates additional holes in the channel which then requires a more positive V_{TG} to deplete.

Obstacles and improvements

The conduction band of monolayer WSe_2 is difficult to probe and only a few works report on electron transport properties in the literature [13, 14] using high quality TMDCs-based devices with advanced contact engineering. In an attempt to reach this regime, or to increase the current flowing through the channel, we tried to improve our device fabrication method. In particular, we deposited the WSe_2 flakes at $T \sim 150^o$C using an integrated oven in our flake deposition setup.

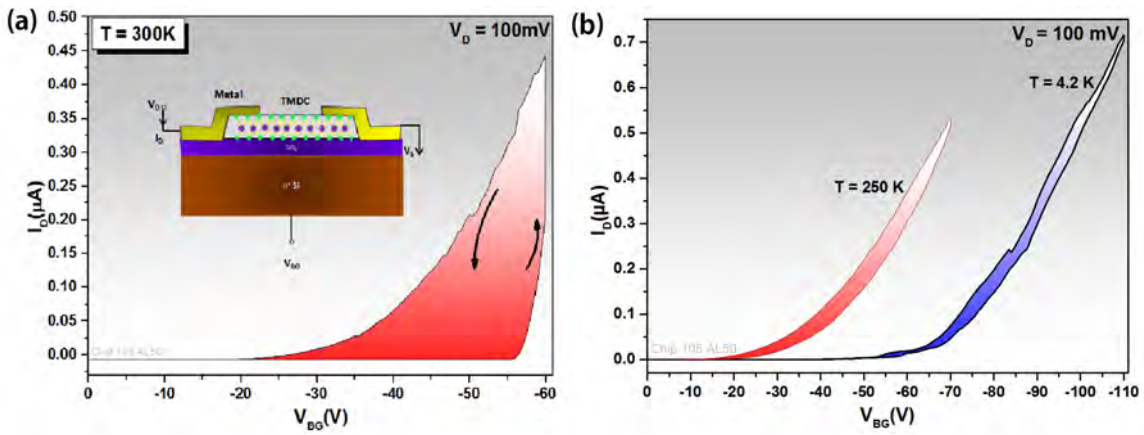

Figure 3.23: (a) Hysteresis effect on a FET based WSe_2 multi-layer contacted with platinum electrodes at room temperature. (b) The hysteresis effect decreases as the temperature is lowered.

The mechanical properties of the PDMS stamp are modified at this temperature and the formation of bubbles between the h-BN/WSe_2 interface should be reduced. However, despite many attempts, the results were not encouraging. Above room temperature, we found that a PDMS residue remains on the substrate and obstructed the homogeneous deposition of the PMMA resist. It was then impossible to proceed further with the fabrication process.

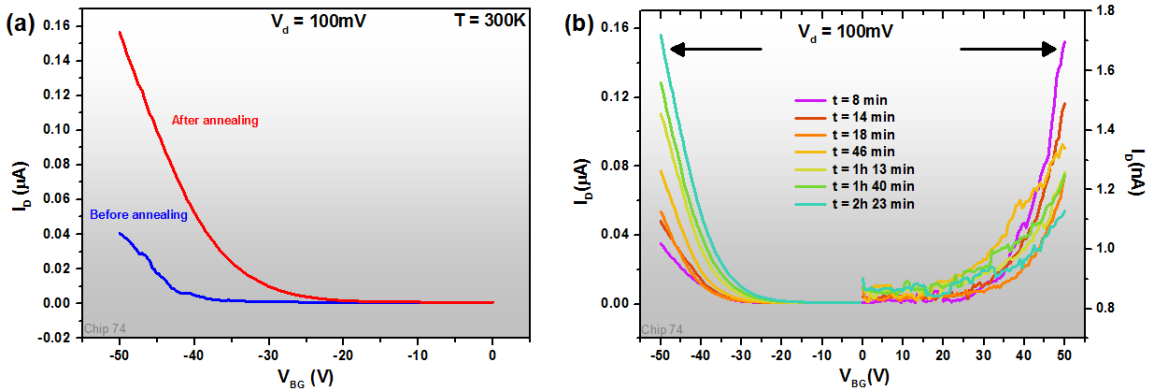

Figure 3.24: (a) Electrical characteristics of tri-layer WSe_2 before and after annealing at 400 ^{o}C. (b) and (c) Evolution of the device performance after annealing for the p-doped and n-doped regimes, respectively, (t corresponds to the time were I performed the electrical characterisation after removing the sample from the annealing chamber).

We also tried to anneal our final devices in vacuum [101]. The annealing process changed the electrical properties of the devices, but it is rather unreproducible and non permanent. Figure 3.24 shows an example of vacuum annealing of a trilayer WSe_2 device for 2 hours at $T_{max} = 400$ ^{o}C including ramps of 20 K/min, where the current after annealing exceeds 4 times the one measured before annealing at $V_{BG} = -50$ V. The n-doped regime was achieved in this particular annealed device, however the current remained too small to proceed with high magnetic field measurements.

Although the electron conduction regime has been reached in this annealed device, the current remains very weak for positive back-gate voltages. Depending on the work-functions of the materials into electrical contact and Fermi level pinning, the Schottky barriers can be much different for electrons and holes, resulting in a strong conduction asymmetry. Temperature-dependent transport measurements would have certainly helped to clarify this hypothesis, but was out of the scope of this thesis.

3.2 Measurements in pulsed magnetic field and low temperature

This chapter describes the key aspects of the experimental techniques used to generate pulsed magnetic field and to perform magneto-transport measurements at very low temperature. In comparison to DC high magnetic field, pulsed magnetic field is less expensive to operate and reaches higher maximum magnetic field. On the other hand, the repetition rate of a measurement is limited by the time required to cool down the coil at liquid nitrogen after a magnetic field pulse, while the duration of the pulse is mainly limited by the coil size (impedance) and the maximum energy which can be stored in the capacitor bank. The experimental work achieved during this thesis was performed with magnetic field pulses of duration $\sim$ 300 ms and maximum field of 55 T, which could be repeated every hour roughly. The short duration of the pulse demands a particular instrumentation and experimental know-how to obtain reliable results.

3.2.1 Pulsed magnetic field generation

Pulsed magnetic fields are produced via the discharge of a large capacitor bank in a resistive coil cooled down to liquid nitrogen temperature (77K). A scheme of principle is shown in figure 3.25.

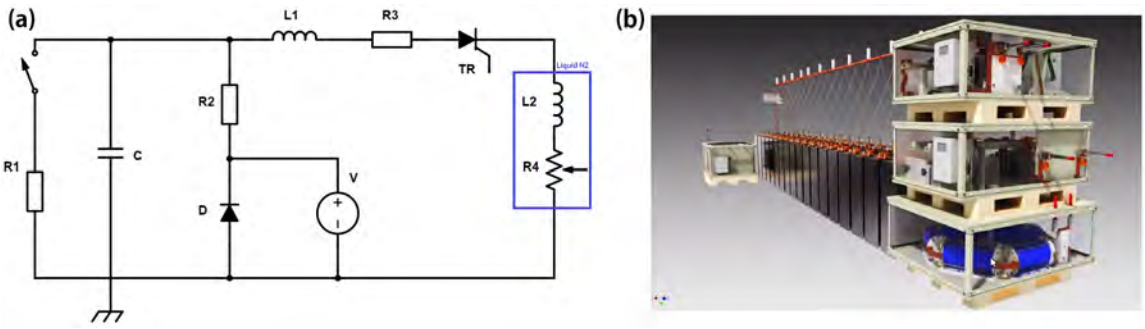

Figure 3.25: a) Schematic electric diagram to produce a pulsed magnetic field. b) New 14 MJ generator at LNCMI.

The capacitor bank is able to store an electrostatic energy of 14 MJ when charged under a maximum voltage of 24 kV. When the charge is complete, optically triggered thyristors (TR) let the current flow to the magnetic field generating coil. The coil is cooled at nitrogen temperature to reduce its resistance from $\sim$ 800 mΩ at room temperature to 125 mΩ. After a magnetic field pulse, the temperature of the coil reaches roughly 200 K. The current flowing through the coil circuit, which is proportional to

the produced magnetic field, will increase in a sinusoidal fashion until reaching its maximum value at $t = \frac{\pi}{2}\sqrt{L_2.C}$ where L_2 is the total inductance of the circuit and C is the capacity of the capacitor bank. At this moment the voltage at the capacitor bank changes sign (in a LC circuit, the voltage is at phase quadrature with the current) and the diode becomes conductive. The magnetic energy stored in the coil will dissipate by the Joule effect in a resistance in serie with the circuit containing the diode. The current, and therefore the magnetic field, will decrease according to an exponential law having a time constant $\tau = L_2/R_4$ (see figure reffig:60T coil). The inductors ($L_1 = 1mH$) in serie with the magnetic field producing coil protect the circuit against excessively strong currents which may appear in case of coil failure (short-circuit).

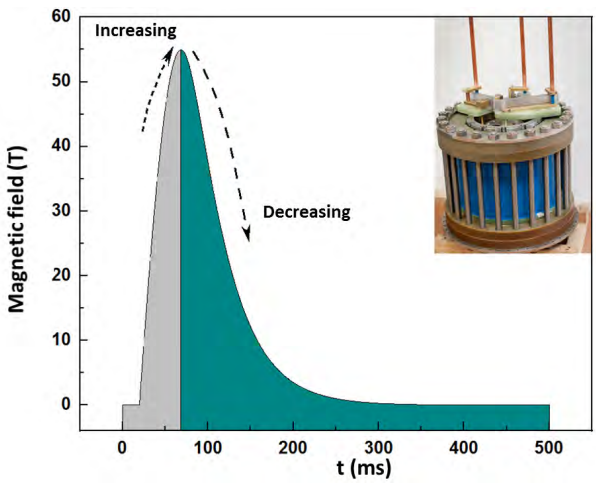

Figure 3.26: Pulsed magnetic field as a function of time, reaching 60T at maximum.

The coil represented in the inset of figure 3.26 is made by winding a copper wire reinforced with zylon embedded in epoxy resin.

3.2.2 Cryogenics

Low temperature is required to study quantum effects in condensed matter. Cryogenic liquids are used for this purpose. All the magneto-transport measurements performed during this thesis were done at low temperature in a cryostat combining both nitrogen and helium liquids.

Liquid nitrogen cryostat

The liquid nitrogen cryostat is a large vessel made with a double wall of stainless steel. It is sealed with a 3 cm thick poly-carbonate cover. The liquid nitrogen cryostat holds

the coil which produces the high magnetic field. After a pulse of magnetic field, a large part of the liquid nitrogen is used and evaporated for cooling down the coil. The evaporation process is facilitated by pumping the nitrogen vapour, which speeds up the cooling down process of the coil to roughly 40 minutes at maximum. The cryostat is automatically refilled when the liquid nitrogen level is below a user-defined threshold. The nitrogen cryostat supports a helium cryostat located in the core of the magnetic field coil (see figure 3.27-a).

Liquid helium cryostat

The helium cryostat is shaped as a cylinder with two different diameters. The largest diameter part, located at the top of the cryostat, is composed of a double wall of stainless steel containing a large quantity of liquid helium. The smaller diameter part, located at the bottom, is inserted inside the core of the coil used for magnetic field generation. It is filled with liquid helium using a cold valve (needle valve) connecting to the upper part of the cryostat. The sample is located inside the bottom part of the cryostat, using an insert, in the middle of the coil where the magnetic field is maximum. This part of the cryostat can be pumped to decrease the temperature down to 1.6K. On the contrary, to achieve temperature above liquid helium up to room temperature, a heater is glued on the inner tube of the stainless steel double wall, close to the sample (see figure 3.27-b).

3.2.3 Insert and sample holder

For performing transport-measurement, the sample must be electrically bounded and placed at the bottom of an insert. First, we glue the sample on a ceramic disk with 10 serigraphied gold pads as shown in figure 3.27-c. The gold pads allow us to connect the sample with the wedge bonding machine. The ceramic plate is then glued to a 10-pin commercial socket with GE-varnish. The electrical connections between the ceramic pad and the socket are hand-made using silver paste. The socket is directly plugged at the bottom part of the inserts, made with glass fiber instead of metal to avoid eddy current induced by the pulsed magnetic field. The wires connecting the sample (low temperature bottom part of the insert) to the Jeager connector (room temperature upper part of the insert) are twisted in pairs to reduce the parasitic induced voltage during the pulse. The insert diameter depends on the core of the coils, starting from 8 mm for 90T coils to 28 mm for 60 T coils. Some inserts are equipped with a rotation stage in order to tilt the sample from parallel to perpendicular with respect of the magnetic field direction. The precise tilt angle is measured using a pick-up coil which rotates together with the sample stage. The temperature is set and/or measured using a Lakeshore 331 controller with a diode sensor (DT-670) placed nearby the

sample.

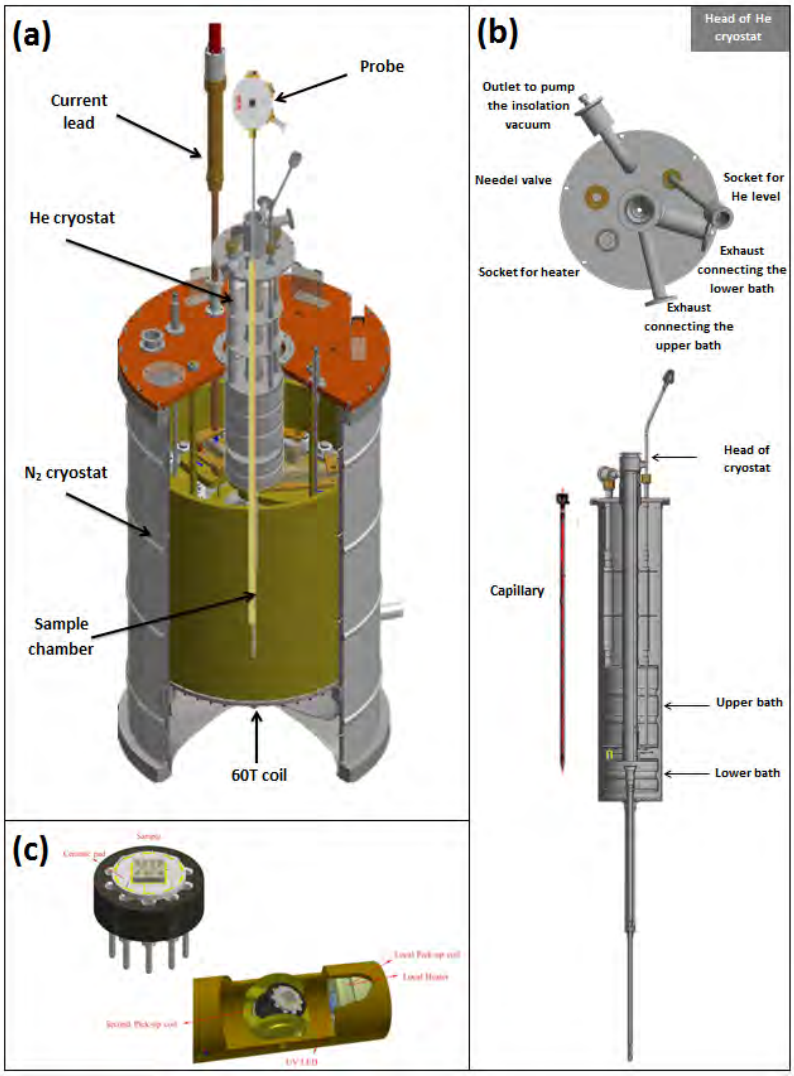

Figure 3.27: (a) a general view of The ^{4}He cryostat inserted inside the coil used for magnetic field generation, in a large nitrogen cryostat with the probe. (b) A detailed description of ^{4}He cryostat with a top and interior view. (c) Head of the rotative probe with a connected sample.

3.2.4 Data acquisition and induced voltage removal

Transport measurements in a pulsed magnetic field is usually much more challenging than its DC-field counterpart because of the short duration of the pulse. When the

typical resistance of the samples is more than a few tens of kOhms (as it is the case for the WSe_2 samples measured in this thesis), the excitation must be continuous (DC measurement mode). Indeed, the use of lock-in is prohibited in this case as the minimum modulation frequency (set by the magnetic field pulse duration) is strongly attenuated by RC low-pass filtering, where R is the sample'es resistance and C is the circuitry capacitance. An induced voltage proportional the time-derivative of the magnetic flux enclosing the sample circuitry $U = \frac{d}{dt}\left[\iint \vec{B}.d\vec{S}\right]$ adds to the sample's voltage. This parasitic induced voltage may exceed the value of the signal itself. Besides, the mechanical vibrations of the insert during a pulse of magnetic field generate noise and render the measurement of small voltages a difficult task. Usually, the excitation current or voltage must be about one order of magnitude higher compared to DC magnetic field experiments in order to achieve comparable signal-to-noise ratio.

A pulsed magnetic field measurement campaign starts with the introduction of the insert inside the cryostat, which was previously heated up at room temperature to avoid thermal shocks. During the manipulation of the insert, the sample is grounded to prevent any uncontrolled electrostatic discharge which would otherwise burn it. The electrical connection between the sample and the measurement system is realized using a switch box. Then, the sample is allowed to cool down slowly using the Lakeshore temperature controller. Once the sample is at the desired temperature (usually 4.2 K or 1.6 K) and the coil is cold enough, users must exit the experimental room, close the door and operate remotely the experiment from a computer installed in a safe place. Inside the experi-

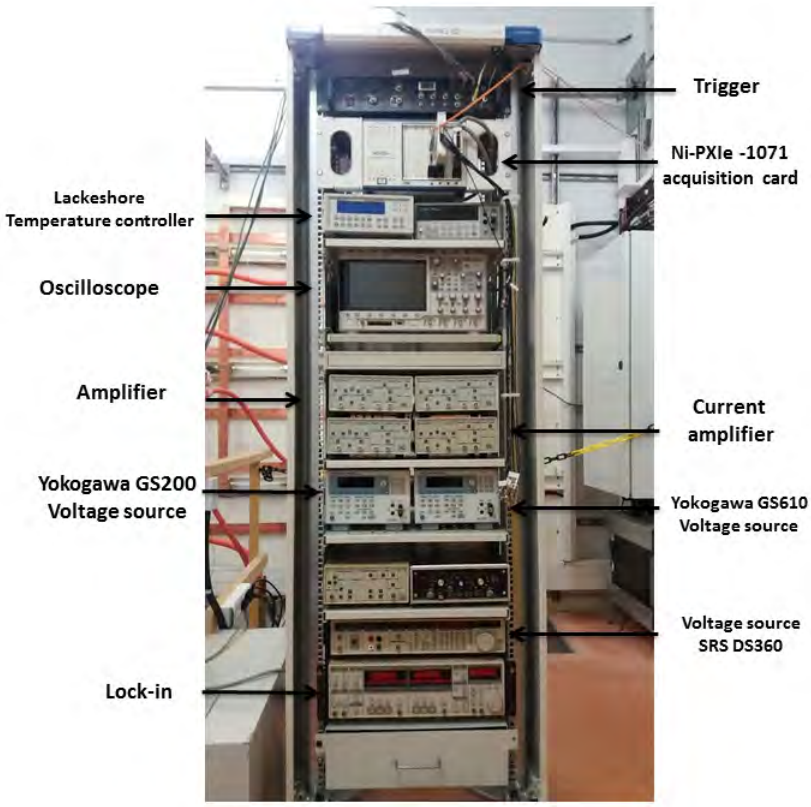

Figure 3.28: Data acquisition setup.

mental room, a PXI chassis holding a fast data acquisition card, is controlled via an optical fiber connected to the user's computer outside the room. The data acquisition system is synchronized to the pulsed magnetic field so that when the capacitor bank is fully charged, the user can start the pulsed magnetic field generation after making sure all the safety issues are respected.

The data acquisition card can measure up to 8 channels with maximum frequency 2 MHz. Two channels are dedicated to the main and rotation pick-up coils, while the rest can be set according to the experimental configuration. A Labview software drives the data acquisition process and records the raw data in a file with ASCII format, where the first column is the time. The raw data pre-processing is semi-automatic using a home-made software with screen capture shown in figures 3.29. First, a fraction of the pick up voltage is subtracted to the signal. The proportionality factor is set properly when the signal acquired as the magnetic field increases matches the one recorded when the magnetic field decreases. Due to the stray inductance and capacitance of the measuring circuit, the induced voltage removal may not be perfect. Most of the time and when temperature is not an issue, the signal recorded as the magnetic field decreases is kept for further data analysis. Next, the software smooth the data using the windows averaging method and perform basic mathematical operations to set the correct units. We note that the induced voltage can alternatively be eliminated by running two magnetic field pulses with reversed polarity. Symmetrization or anti-symmetrization of the signal is performed numerically to extract either the magneto-resistance or the Hall signal.

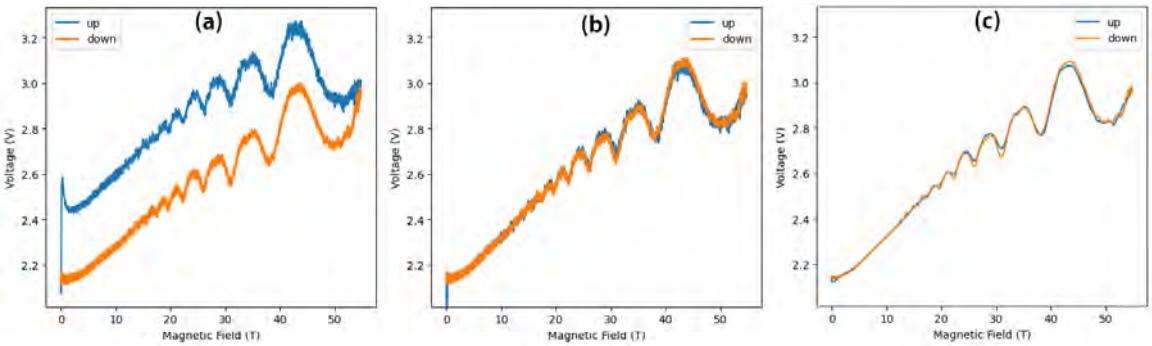

Figure 3.29: a) Raw signal: voltage vs magnetic field, b) The parasitic induced voltage has been removed from the sample's signal, c) Windows averaging is used to smooth the signal

Chapter 4

Quantum oscillations in a p-doped WSe_2 monolayer

Contents

4.1 Sample characterization and magneto-transport **72**

4.1.1 Fabrication 72

4.1.2 Characterization 72

4.1.3 High magnetic field measurements 74

4.1.4 Effective mass 76

4.2 Magneto-transport simulation **77**

4.2.1 Schrödinger fermions or massive Dirac fermions ? 77

4.2.2 Electro-chemical potential 78

4.2.3 Self-consistent determination of the electrochemical potential 79

4.2.4 Components of the conductivity tensor 80

4.2.5 Simulations 83

4.3 Experimental determination of the Landé factor **87**

4.3.1 Multiplicity of the ratio E_z/E_c 87

4.3.2 Carrier density evolution of the g-factor 88

4.4 Concluding remarks **91**

Many samples have been fabricated following the procedure described in section 3.1, however only a few of them provided exploitable magneto-transport results. Most of the time, the resistance of the samples was too large to allow a correct signal-to-noise ratio with DC measurement method, not to mention failures of the clean room processes. Besides, monolayer WSe_2 samples are fragile and a measurement campaign (lasting between one and two weeks on average) under extreme conditions of low temperature and high magnetic field remains challenging. In this chapter, we will focus on a particular monolayer WSe_2 sample with the best characteristics. We start with a description of the sample and the magneto-transport results, before presenting the model to simulate the experimental data. We finish with a discussion regarding the evaluation of the Landé factor and its evolution with carrier density.

4.1 Sample characterization and magneto-transport

4.1.1 Fabrication

Figure 6.15-a) shows the optical image of the sample after the whole fabrication process. A monolayer WSe_2 flake is deposited on top of a larger BN flake, lying on a Si/SiO_2 substrate. A red dotted line circles the monolayer WSe_2 flake (not clearly visible on the picture) and a thicker flake of thickness 10 nm attached to it. The BN flake is, on the other hand, enclosed with a blue dotted line. Although the sample could not be etched into a Hall, the electrode design includes two large contacts for current injection and four electrodes located on both sides of the sample. Two of them (left-hand side electrodes in figure 6.15-a) connect the larger WSe_2 flake before addressing the monolayer. The four-probe magneto-resistance measured with this two contacts did not provide exploitable results and have been discarded from analysis. Regrettably, the Hall voltage could not be properly measured for the same reasons. The magneto-resistance data presented later in this chapter therefore originate from the other pair of electrodes (right-hand side electrodes) with direct contact to the monolayer flake. Figure 6.15-b) shows a sketch of the sample with operating electrodes only.

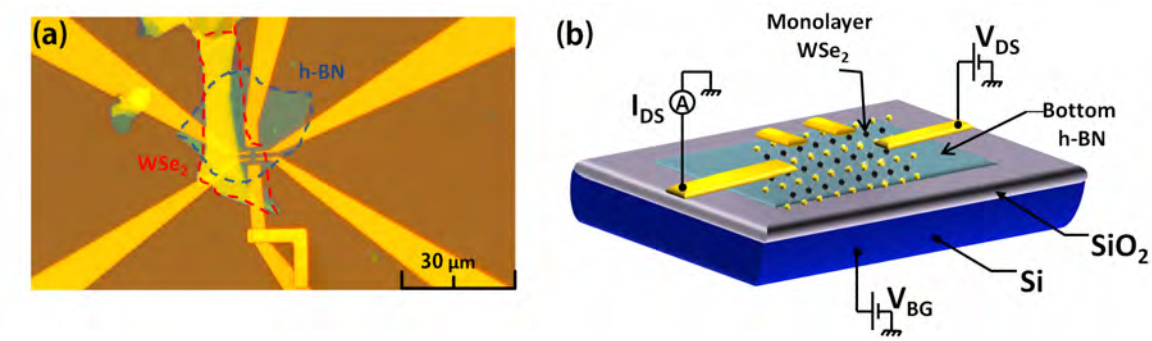

Figure 4.1: a) Optical image of a barely visible monolayer WSe_2 sample attached to a thicker flake. The whole WSe_2 flake and the underlying BN flake are enclosed by red and blue dotted lines, respectively. b) Sketch of the sample with operating electrodes connecting the monolayer WSe_2. The carrier density can be tuned electrostatically using a back-gate voltage V_{BG}.

4.1.2 Characterization

Structural and optical characterization techniques were performed to certify the monolayer nature of the WSe_2 flake in this sample. Figure 4.2-a) shows an AFM image together with the height profile on the edge of the WSe_2 flake marked with a blue line

on the image. The step height is equal to 0.7 nm in agreement with the typical monolayer thickness. Another confirmation came from Bright field-scanning transmission electron microscopy (BF-STEM) analysis (figure 4.2-b) performed on the device after the whole measurement campaign, where the monolayer WSe_2 flake is observed with side-view. The BF-STEM technique makes it possible to get atomic resolution with heavy atoms appearing in dark (tungsten and selenium atoms with atomic numbers $Z_W = 74$ and $Z_{Se} = 34$, respectively) and lighter atoms (bore and nitrogen atoms with atomic numbers $Z_B = 5$ and $Z_N = 7$, respectively) in brighter tones. When compared to other Transmission electron microscopy (TEM) techniques, BF-STEM imaging is less dependent on imaging conditions. The inter-atomic distances between W and Se atoms correspond to the expected ones. The WSe_2 layer is continuous and reproduces the top surface of the h-BN stack. Although the BF-STEM analysis visualizes only a limited sample area, we assume that the scanned part is representative of the whole flake considering its homogeneity observed with optical microscope and AFM. Last, the photoluminescence fingerprint of monolayer WSe_2 was retrieved with an emission peak at 1.63 eV as shown in figure 4.2-c).

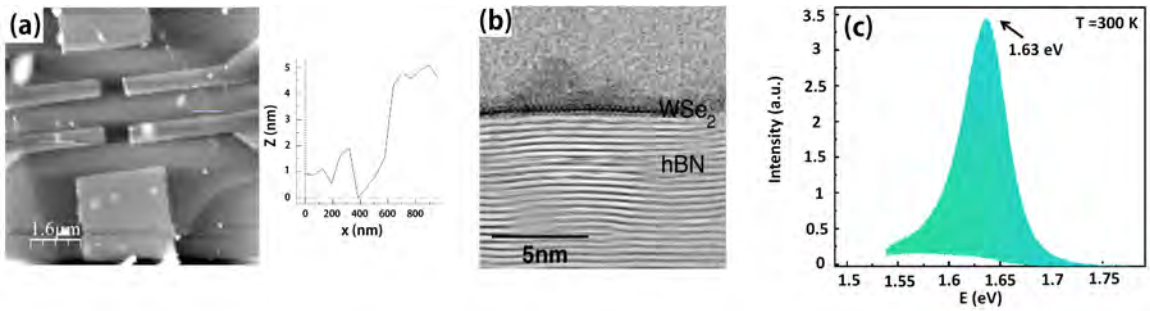

Figure 4.2: a) Left: AFM image of the sample. Right: the height profile from monolayer WSe_2 to the underlying BN flake. b) BF-STEM image on which the h-BN flake appears as dark/bright fringes whereas the WSe_2 monolayer consists of dark spots surrounded by brighter ones. c) Photoluminescence spectrum typical of WSe_2 monolayer.

After bonding the sample and fixing it into an insert dedicated for 60 T pulsed magnetic field measurements, we cooled down the sample and measured the drain-source current I_{DS} vs V_{BG} at three different temperatures as shown in figure 4.3. The drain-source voltage is set to $V_{DS} = 100$ mV while the back-gate voltage V_{BG}, ranging from 0 to -110 V, is delivered using Yokogawa GS610 voltage source. The drain-source current I_{DS} is amplified with a low noise current preamplifier (SR570) and measured with an Agilent (34401A) voltmeter. The device turns into the "ON" state only for back-gate voltages below a temperature-dependent threshold voltage V_{BG}^{thr}. When a current flows, the Fermi energy is close enough to the top of the valence band so

that thermally excited holes have enough energy to overcome the Schottky barrier. The electron conduction regime was searched for V_{BG} up to +110 V, but could not be observed for this sample.

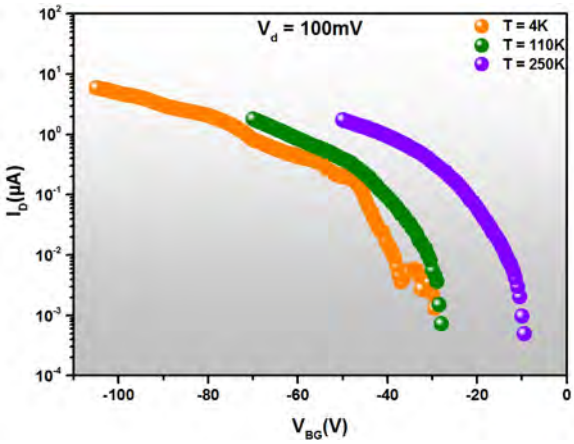

Figure 4.3: Evolution of the drain-source current as a function of the back-gate voltage, for three different temperatures, evidencing a temperature-dependent back-gate voltage threshold for the "ON" state. The fluctuations of the lowest temperature curve reflects impurity levels in the gap or in the Schottky barriers.

4.1.3 High magnetic field measurements

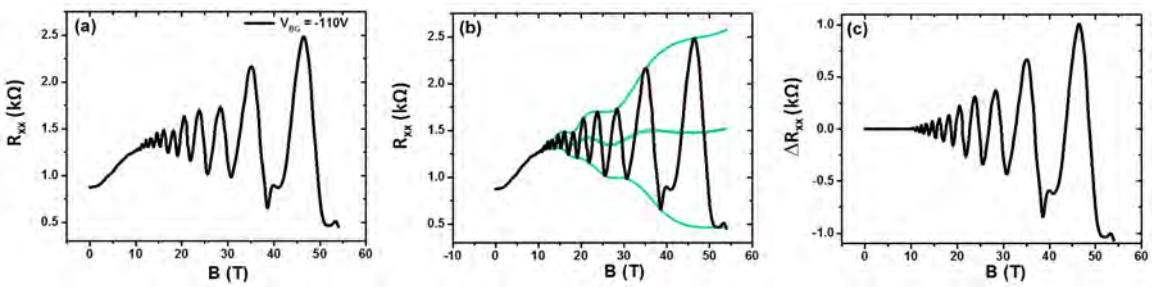

Figure 4.4: Background removal procedure. a) Raw data. b) Manual identification of the oscillations' extrema, defining the envelope spline functions and the background. c) Background subtracted data.

We performed magneto-transport measurements under pulsed magnetic field up to 55 T at low temperature down to 4.2 K for different values of the back-gate voltage. A constant DC current of 1 μA is passed through the sample while measurement the longitudinal voltage is synchronized with the magnetic field pulse. The magneto-

resistance displays large-amplitude oscillating features on top of a smooth background when the back-gate voltage is set close to its maximum experimental limit ($-110\,\mathrm{V}$), e.g. for high hole concentrations. On the other hand, for back-gate voltage close to V_{BG}^{thr}, the current injection is hindered by large Schottky barriers and may not flow homogeneously in the sample. In this regime, we measure weak and distorted oscillations of the magneto-resistance on top of a large and non-monotonous background. The proper analysis of the quantum oscillations requires their extraction by numerical removal of the magneto-resistance background, related to smooth variations of the mean scattering time induced by the magnetic field beyond the effect of the density of states quantization (equations 2.36). This treatment is quite subtle: although the periodicity of the extracted oscillations is only weakly user-dependent, the shape of the extrema is quite sensitive to the method used. For high mobility samples, the magneto-resistance background is usually a smooth and monotonous function which can be removed by subtracting to the raw data either a pair polynomial function, or the magneto-resistance data at a high enough temperature where the quantum oscillations have vanished. This simple method is however not adapted for this sample where the background is tortuous and changes drastically for different back-gate voltages. We preferred a manual method which consists first in identifying the oscillations' extrema. Then, two spline curves $\mathbf{S}^{+}_{(B)}$ and $\mathbf{S}^{-}_{(B)}$ are computed passing by the maxima and the minima respectively, thus defining the envelopes of the oscillations. The half-sum of these curves produces the background signal which is subtracted to the raw data $\Delta R_{xx}(B) = R_{xx}(B) - \frac{1}{2}(S^{+}_{(B)} + S^{-}_{(B)})$, as shown in figure 4.4 for $\mathrm{V}_{BG} = -110\mathrm{V}$. The background removal becomes subject to personal interpretation for low carrier density, where the identification of the relevant oscillations is problematic.

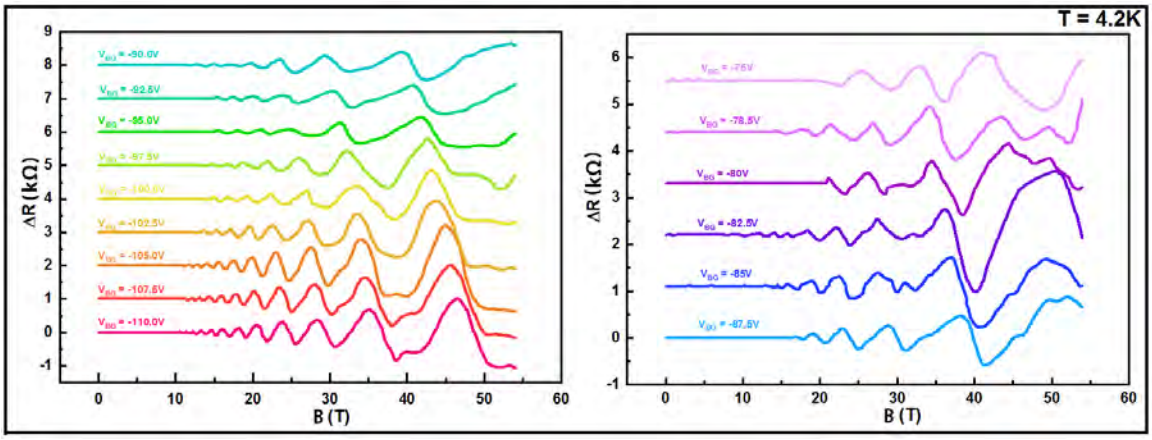

Figure 4.5: High field magneto-resistance of monolayer WSe_2 at $T = 4.2\,\mathrm{K}$, for different back-gate voltages. The curves are offset and split into two graphs for clarity.

The data after treatment are shown in figure 6.16: for all back-gate voltages, the oscillation pattern is complex and must be analyzed beyond the single band model with 1/B-periodic SdH oscillations. We assume that a large Zeeman energy competes with the cyclotron energy to produce distorted or extra oscillating features. This model will be described in the next section. Although the oscillations' extrema can be traced from one curve to the other, it is worth pointing out that they display a rather irregular behavior for $V_{BG} > -90\,\mathrm{V}$. These data will thus be discarded from analysis.

4.1.4 Effective mass

Following the lines of section 2.2.5, the temperature dependence of the quantum oscillations can be studied to determine the effective mass. As expected, the amplitude A between two successive extrema decreases with increasing temperature as plotted in the insert of figure 4.6 for $V_{BG} = -105\,\mathrm{V}$ in a temperature range of 1.4 K to 15 K. By plotting $\ln(A/T)$ versus temperature, we obtain a straight line with slope equals to $2\pi^2.m^*.k_B.T/q.B.\hbar$. The extracted value of the effective mass $m^* = (0.45 \pm 0.04) \times m_e$ is in agreement with the literature [13].

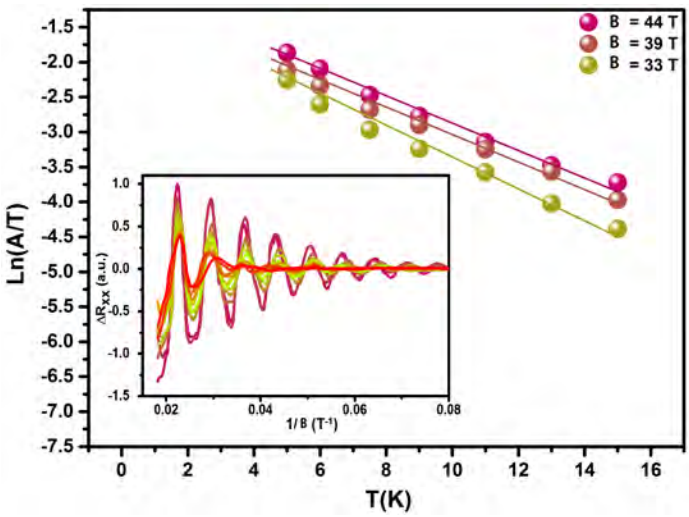

Figure 4.6: Determination of the effective mass, where the amplitude of the oscillations as a function of temperature is evaluated for different values of the magnetic field. Insert: temperature evolution of monolayer WSe_2 magneto-resistance at $V_{BG} = -105\,\mathrm{V}$, in the temperature range 1.4 K to 15 K.

4.2 Magneto-transport simulation

The Lifschitz-Kosevich formula presented in section 6.11, including the spin contribution, could reproduce parts of the longitudinal resistivity curves, but was proven unadapted when investigating the whole experimental dataset. Therefore, we decided to investigate on the quantum oscillations beyond the SdH oscillation regime. This section is devoted to the model, developed using Python, to simulate the oscillatory part of the magneto-resistivity at both weak and high magnetic field.

4.2.1 Schrödinger fermions or massive Dirac fermions ?

WSe_2 monolayers are expected to host quasi-particles named after "massive Dirac fermions" (MDF). The energy dispersion is quasi-linear in the vicinity of the K and K' points and the lack of inversion symmetry introduces a gap Δ between the conduction band and the valence bands [19]. The valence band is spin-split with a gap Δ^v_{SOC} (see table 1.10) due to the spin-orbit interaction [17, 19, 20]. For energies very close to the top of the upper valence band, the dispersion relation can be approximated to a parabolic function with effective mass $m^* = (\Delta - \Delta^v_{SOC})/v_F^2$. Setting the energy origin at the top of the upper valence band and applying a perpendicular magnetic field, the energy is quantized into Landau levels whose energy spectrum is (without taking into account the Zeeman energy):

$$\epsilon^v_{N,s\tau} = -N\hbar\omega_c = -N\frac{\hbar qB}{m^*} \tag{4.1}$$

where $N = 0, 1, 2...$, and $s.\tau = \pm 1$ are the Landau level index and the product of the spin and valley indexes, respectively. In the absence of Zeeman effect, the Landau levels are two-fold degenerate except the non-dispersive $N = 0$ Landau level which is non-degenerate. The nature of the quasi-particles (e.g. Massive Dirac fermions) is encoded in the wave-functions and cannot be revealed when looking only at the band-structure. Actually, if one changes the nature of the quasi-particles to the canonical Schrödinger fermions discussed in section 2.2.1, the Landau level spectrum would be very similar to equation 4.1 except the following points: N is changed to $N+1$ and the $N = 0$ Landau level is two-fold degenerate. Including Zeeman energy and anticipating the discussion of section 4.3.2, the two models provide the same magneto-transport signature provided the ratio between the Zeeman energy and the cyclotron energy is offset by 1. In the following and without any loss of generality, we will analyze our experimental results considering a spin degenerate 2D gas of Schrödinger fermions before discussing the massive Dirac fermion model in section 4.3.2. For simplicity and for the rest of this section, we will consider positive energies for the valence band Landau levels (e.g. the minus sign of equation 4.1 will be dropped) and the coupled

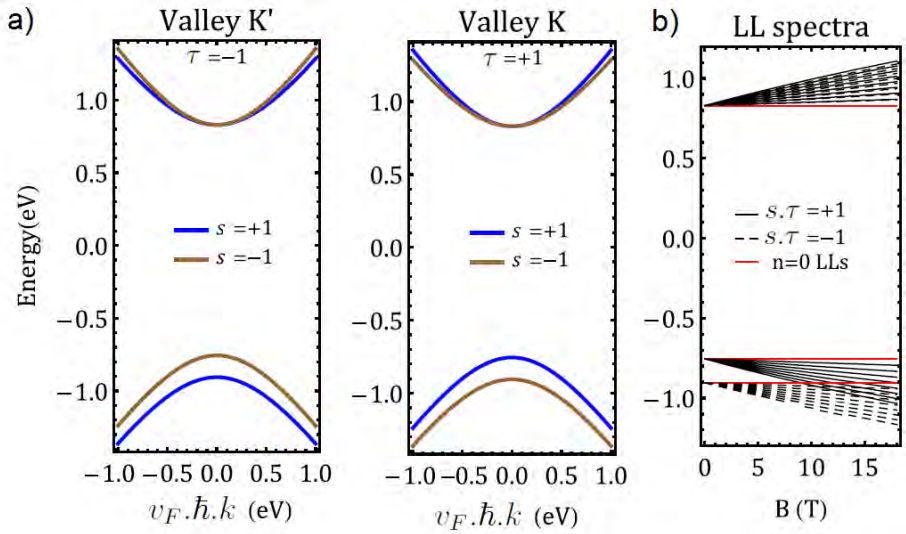

Figure 4.7: a) Band structure of monolayer WSe_2 at points K and K' of the first Brillouin zone. The dispersion relation can be approximated by a parabolic function for energies close to the top of the spin-split valence bands. b) Under perpendicular magnetic field, the energy is quantized into two-fold degenerate Landau levels, except the non-dispersive $N = 0$ Landau level. Adapted from [19]

spin/valley $s.\tau$ indexes will be referred to as the spin index $s = \pm 1$ only.

4.2.2 Electro-chemical potential

Gaussian broadening of the Landau levels

As discussed in section 2.2.3, the energy of the charge carriers are quantized into Landau levels in the presence of a perpendicular magnetic field. When the Zeeman energy is included, the energy of the Landau levels writes:

$$\epsilon_{N,s} = \frac{\hbar q B}{m^*}\left(N + \frac{1}{2}\right) + s\frac{m\left(\epsilon_z/\epsilon_c\right)}{m^*}\mu_B B \tag{4.2}$$

where ϵ_z/ϵ_c is the ratio of the Zeeman energy over the cyclotron energy, N is the Landau level index ($N = 0, 1, 2...$) and $s = \pm 1$ is the spin index. The Landau level degeneracy, $g_L = qB/h$, is the density of states contribution of each Landau levels. We assume that the energy of the quantum states of the Nth Landau level is not exactly at $\epsilon_{N,s}$ but follows a Gaussian distribution $\left(1/\sqrt{2\pi}\Gamma\right) \times \exp\left[-\left(\left(\epsilon - \epsilon_{N,s}\right)/\Gamma\right)^2/2\right]$ around the energy $\epsilon_{N,s}$. The prefactor $1/\sqrt{2\pi}\Gamma$ is required to make sure that the area enclosed by the Gaussian function is normalized to unity. The density of states is

therefore simulated using equation 6.12:

$$\rho(\epsilon, B) = \frac{qB}{h} \sum_{N,s} G_{LL}(\epsilon - \epsilon_{N,s}) = \sum_{N=0,s=\pm 1}^{N=N_c} \frac{qB}{h} \times \frac{1}{\sqrt{2\pi}\Gamma(B)} \times \exp\left[\left(\frac{-(\epsilon - \epsilon_{N,s})}{\Gamma^2(B)}\right)^2\right] \tag{4.3}$$

Here, $N_c \sim 20$ represents a cut-off parameter for the sum over the Landau level index, which should otherwise run to infinity. We also introduced the field-dependent Landau level broadening $\Gamma(B)$ so that the full width half maximum (FWHM) of the normal Gaussian distribution is given by $FWHM = 2\sqrt{2\ln(2)} \times \Gamma(B)$. This broadening is linked to the hole (quantum) mobility μ^h, a fit parameter, through the relation $\Gamma(B) = \frac{\hbar q}{m^*}\sqrt{\frac{2B}{\pi\mu^h}}$. We assume the same broadening for all the Landau levels, whatever their orbital and spin index. We note that the Landau level based density of states has been approached with a sum of Lorentzian broadening functions in section 2.46 for the demonstration of the Lifschitz-Kosevich formula. This choice was motivated by the fact that the subsequent Fourier transform of Lorentzian functions are simply exponential functions, allowing an analytical derivation of the formula, with implicit hypothesis of a constant electrochemical potential. However, the use of Lorentzian functions instead of Gaussian functions in equation 6.12 fails to properly reproduce the electrochemical variations. Indeed, the tail of the Lorentzian functions is larger to their Gaussian counterparts and leads to diverging chemical potential at low magnetic field.

4.2.3 Self-consistent determination of the electrochemical potential

The electrochemical potential, noted μ in the following, is the energy of the highest occupied quantum states. It corresponds exactly to the Fermi energy at absolute zero temperature. The carrier density is computed by counting the cumulative orbital degeneracy up to the chemical potential:

$$n^h = \int_{-\infty}^{+\infty} \rho(\epsilon, B) f\left(\epsilon - \mu_{(B)}\right) d\epsilon \tag{4.4}$$

where $f(\epsilon - \mu)$ is the Fermi-Dirac distribution function (see figure 2.2). For each value of the magnetic field in the range [0.1 T ; 55 T], a Python routine computes the electrochemical potential $\mu(B)$ so that n^h is a constant (user-defined parameter), set by the fixed back-gate voltage V_{BG}. The electrochemical potential, which varies according to the variation of the density of states induced by the magnetic field, is displayed in figure 4.8 for a given carrier density and two different hole mobilities.

For weak magnetic field, the chemical potential is nearly constant and equals the zero magnetic field expectation $\mu(B=0) = \left(2\pi\hbar^2.n^h\right)/(g_s.m^*)$ for 2D electron systems. On the other hand, large variations are observed at high magnetic field. The electrochemical potential follows the highest occupied Landau level (i^{th}) until the total density of states (which increases linearly with magnetic field) is enough to hold all the charge carriers up to the $i^{th}-1$ Landau level. The electrochemical potential drop from a Landau level to the adjacent lower energy one is sudden at low temperature and/or weak Landau level broadening, and tends to soften when the temperature and/or Landau level broadening increases. When the ratio of the Zeeman energy to the cyclotron energy is an integer (or null), the electrochemical potential crosses the Landau levels for the same magnetic field values as if the electrochemical potential was constant. However, this picture changes for non-integer values of E_z/E_c, as shown in figure 4.8 which compares the two cases.

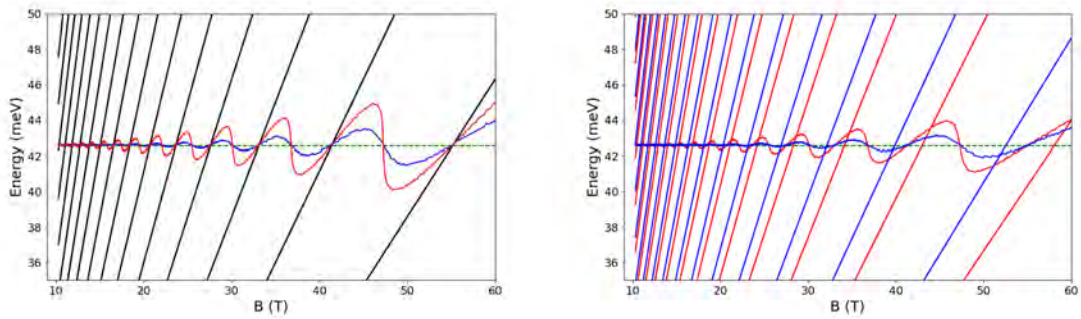

Figure 4.8: Evolution of the chemical potential $\mu(B)$ at $T = 4.2\,\mathrm{K}$ for $\mu^h = 2000\,\mathrm{cm}^2/\mathrm{V.s}$ (blue curve) and $\mu^h = 6000\,\mathrm{cm}^2/\mathrm{V.s}$ (red curve) for a) a sin-degenerate Landau level structure (E_z/E_c is an integer) and b) a spin-resolved Landau level structure. The green dotted line is $\mu(B=0)$.

4.2.4 Components of the conductivity tensor

The longitudinal conductivity for homogeneous 2D systems is approached using equation 6.14, derived from high-order perturbation theory of electron impurity scattering [109, 24, 23]:

$$\sigma_{xx}(B) = \frac{q^2}{h}\sum_{N,s}\left(N+\frac{1}{2}\right)\int_{-\infty}^{\infty}\left[-\frac{df(\epsilon-\mu_{(B)})}{d\epsilon}\right]\times\exp\left[-\frac{1}{2}\left(\frac{\epsilon-\epsilon_{N,s}}{\Gamma}\right)^2\right]d\epsilon \qquad (4.5)$$

where the exponential term can be traced back from the broadened Landau level expression. A Python-based routine computes the integral for each value of the

magnetic field, taking into account the evolution of $\mu(B)$ calculated earlier. Instead of $\pm\infty$, the lower and upper bounds of the integral is replaced by $\mu - 10 \times k_B.T$ and $\mu + 10 \times k_B.T$, respectively. This expression reproduces well the Shubnikov-de Haas oscillations at low magnetic field, but fails to describe the high magnetic field regime. This is because the nature of scattering changes when the product $\omega_c \tau_q \gg 1$. The relation between the density of states and the scattering rate is difficult to simulate in this regime and, in our case, is treated phenomenologically with a cut-off delta-function of width $\delta\epsilon(B)$ applied on the tail of the exponential functions. The contribution to the conductivity of the quantum states with energy far from $\epsilon_{N,s}$ is suppressed, and acts similarly to a magnetic field-dependent mobility edge which distinguishes the localized from the extended states in the quantum Hall regime (see section 2.2.1). Since the sum of equation 6.14 runs over $s = \pm 1$, the conductivity of the system is interpreted within the two-fluid model without interaction between the charge carriers belonging to different valley/spin indices. The contribution of each quantum states to the conductivity add therefore independently. We emphasize that this model is certainly oversimplified since it cannot reproduce Landau level anti-crossing as investigated in references [16, 11] for MoS_2 and reference [12] for WSe_2 systems. The width of the cut-off delta function ($\delta\epsilon(B)$) spans over three times the FWHM of the Gaussian broadened Landau levels at small magnetic field, so that it has no effect on the simulated curves. However, $\delta\epsilon(B)$ rapidly decreases and becomes comparable to the FWHM near a magnetic field threshold B_0. The magnetic field evolution of $\delta\epsilon(B)$ is established using a Boltzmann-like function

$$\delta\epsilon(B) = \left[\frac{A_1 - A_2}{1 + \exp\left[(B - B_0)/\delta(B)\right]} + A_2\right] \times 3 \times FWHM(B) \tag{4.6}$$

where $A_1 \equiv 1$ while $A_2 \in [0, 1]$, B_0 and δ_B will be determined by the fit routine. Although the parameter B_0 is, in principle, linked to the hole mobility and localization length, we break this constraint and make it a phenomenological free parameter in the simulation. We require the longitudinal resistivity, instead of conductivity, in order to compare the simulation outputs with the experimental results. For this purpose, we simulate the transverse resistivity using equation 4.7:

$$\rho_{xy}(B) = \frac{h}{q^2} \sum_{0}^{N,s} \int_{-\infty}^{+\infty} G_{LL}(\epsilon - \epsilon_{N,s}) \times f(\epsilon - \mu_B) \times d\epsilon)^{-1} \tag{4.7}$$

which counts how many Landau levels are below the electrochemical potential, each of them contributing to the spin-less quantum of resistance $\frac{\hbar}{q^2}$. For computational reasons, the lower bound of the integral is replaced by the lowest energy Landau level minus $5 \times \Gamma(B)$ while the upper bound is changed to $\mu + 10 \times k_B.T$. For typical hole

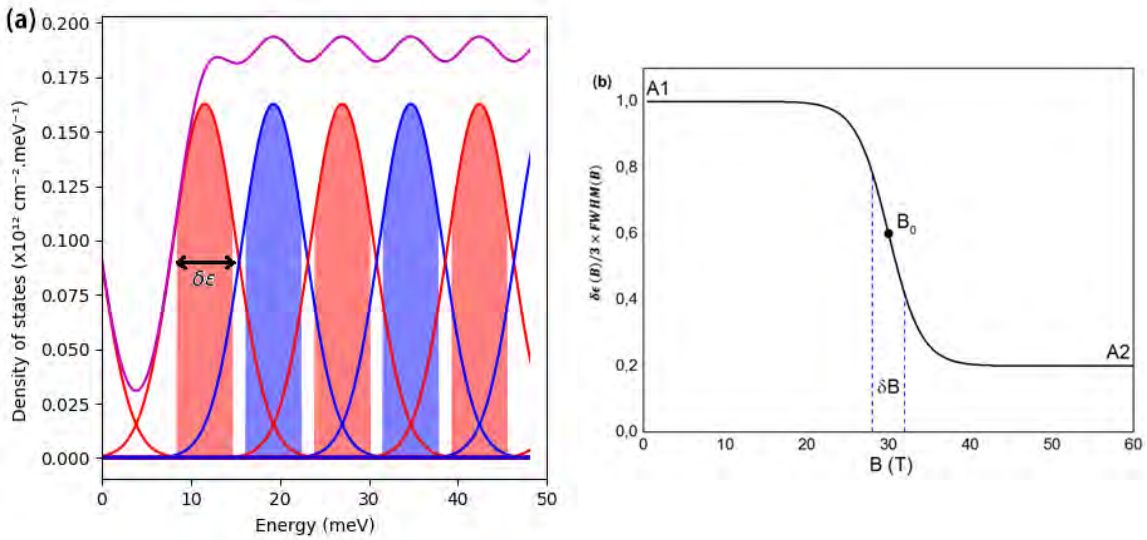

Figure 4.9: a) Spin-resolved broadened Landau levels under high magnetic field. The red curve stands for spin up Landau levels whereas the blue curve represents the spin down. The violet line is the cumulative density of states according to equation 6.12. The filled areas represent the product of the cut-off function $\delta\epsilon(B)$ with the Gaussian broadened Landau levels. Unrealistic parameters have been chosen to prevent overlapping effects and to help understanding the figure: $n^h = 8 \times 10^{12}\,\mathrm{cm}^{-2}$, $B = 60\,\mathrm{T}$, $E_z/E_c = 1/2$, $\mu^h = 2000\,\mathrm{cm}^2/\mathrm{V.s}$, $B_0 = 35\,\mathrm{T}$, $\delta\epsilon(B = 60T) = 6.28\,\mathrm{meV}$. b) Example $\delta\epsilon(B)$ with parameters $A_1 = 1$, $A_2 = 0.2$, $B_0 = 30\,\mathrm{T}$ and $\delta B = 2\,\mathrm{T}$ used to define the cut-off function of the broadened Landau levels. $\delta\epsilon(B)$ defines the actual width of the Landau level states contributing to the conductance.

mobility in the range $\mu^h \sim 2000\,\mathrm{cm}^{-2}$ and temperature $T = 4.2\,\mathrm{K}$, ρ_{xy} is equivalent to its classical expression $\rho^c_{xy} = B/(q.n^h)$ for magnetic field up to roughly 30 T. At higher magnetic field, the linear transverse resistivity is distorted with smooth plateaus reflecting the onset of the quantum Hall regime. Actually, in the magnetic field range [0, 55T], equation 4.7 can be replaced by its classical counterpart in the simulation without much difference. Using the general expressions linking the components of the conductivity tensor to the resistivity tensor, we express ρ_{xx} as a function of ρ_{xy} and σ_{xx} only. We first combine equations $\rho_{xy} = \frac{-\sigma_{xy}}{\sigma^2_{xx}+\sigma^2_{xy}}$ and $\sigma_{xy} = \frac{-\rho_{xy}}{\rho^2_{xx}+\rho^2_{xy}}$ which yields:

$$\rho_{xy}\left(\frac{\sigma_{xx}}{\rho_{xx}}\right) = \frac{\rho_{xy}}{\rho^2_{xx}+\rho^2_{xy}} \Leftrightarrow \sigma_{xx}\rho^2_{xx} - \rho_{xx} + \sigma_{xx}\rho^2_{xy} = 0$$

The solutions to this second order polynomial are : $\rho_{xx} = \frac{1\pm\sqrt{1-4\sigma^2_{xx}\rho^2_{xy}}}{2\sigma_{xx}}$. We drop the unrealistic solution with plus sign and we use the approximation $\sigma_{xx}\rho_{xy} << 1$ when the chemical potential is located in between two successive Landau levels, allowing a

power series expansion of the square-root expression:

$$\rho_{xx} = \frac{1 - \left(1 - 2\sigma_{xx}^2\rho_{xy}^2 - 2\sigma_{xx}^4\rho_{xy}^4 + ...\right)}{2\sigma_{xx}} = \sigma_{xx} \times \rho_{xy}^2 + \sigma_{xx}^3 \times \rho_{xy}^4 + ... \tag{4.8}$$

The next stage consists in extracting the oscillating part of this expression. We proceed with the same method used for the experimental data. A routine searches for the maxima and minima of $\rho_{xx}(B)$ and computes a spline function passing through these points. The half difference between the upper and the lower envelope functions yields the non-oscillating background, which is subtracted to the longitudinal magneto-resistivity. We note that the first order expression of $\rho_{xx}(B)$ is simply the longitudinal conductance multiplied by a smooth function $\rho_{xy}(B)$, which is almost eliminated during the background subtraction process. Therefore, the oscillating part of $\sigma_{xx}(B)$ is very similar to $\rho_{xx}(B)$.

4.2.5 Simulations

Algotrithm and fit procedure

For each value of the back-gate voltage (i.e. for different hole densities n^h), the developed software imports the experimental data $\Delta R_{xx}^{exp}(B)$ and tries to minimize the quantity $\eta = (\Delta R_{xx}^{exp}(B) - \Delta R_{xx}^{sim}(B))^2$. Due to the large number of input parameters (listed in table 4.1) and the difficulty to achieve a nice fitting over the whole magnetic field range, this process cannot be automatized. For instance, the exact fitting of the last oscillation must be abandoned in some cases since the background subtraction is critical at high magnetic field. However the software may consider that the overall error is minimized when this part is properly fitted, to the detriment of the more reliable low magnetic field oscillations. Since each experimental data curve contains some artifacts (due to evident noise during data acquisition or approximate background subtraction in some magnetic field range), we decided to select the best fitting curve manually. For this purpose, the software computes the magneto-resistivity for all the configurations of the user-defined input parameters and computes the associated fit quality η. The simulation, which was mainly running overnight, records the graph of the simulated magneto-resistance superimposed with the experimental data each time η is below a user-defined threshold.

Fit parameters and their relative importance

The range of input parameters and the fit quality threshold are adjusted during initial tests which explore the limits of each parameters. With sufficient practice and know-how, the interplay and contribution of the fit parameters to the magneto-resistivity

becomes more or less predictable, as summarized in table 4.1. Once the simulation stops, the user proceeds with visual inspection of the selected outputs and decide for the best set of parameters.

Fit parameter	Description
n^h	Hole density. Affects the main 1/B-oscillation frequency, especially at low field where the oscillations are more regular
ϵ_z/ϵ_c	Ratio of Zeeman to cyclotron energy. Affects the departure from "perfect" 1/B-oscillating trend
μ^h	Hole mobility. Affects the magnetic field-dependent damping of the amplitude of the oscillations
B_0, A_2, δ_B	Phenomenological parameters which distinguish localized from extended states. Affect the form of the oscillations' maxima
m*	Effective mass. Set to $0.45 \times m_e$ according to the estimation of the effective mass (see section 4.1.4 and reference [13])
T	Temperature. Set to 4.2K, according to experimental measurement conditions

Table 4.1: List of parameters for the simulation and their effect on the simulated magneto-resistance

The simulation was performed for several experimental data with different back-gate voltages, as shown in figure 4.11. As expected, the quality of the fit is better for highly negative back-gate voltage (high hole concentration). In this regime, the resistance of the device is low and the current flowing through the device can be large enough to reveal well defined magneto-resistance oscillations. On the other hand, the best simulated curves fail to reproduce the details of the experimental results for weaker hole concentration. The background subtraction is particularly risky in this regime and can strongly affect the overall shape of the curves, leading to significant discrepancy and fit quality loss. For $V_g \geq -90\,\mathrm{V}$, we estimate that the quality of the experimental data is not good enough for fitting, as even the most obvious features cannot be reproduced with a unique set of parameters. We emphasize on the fact that the very last part of the curves (roughly from 50 T till 55 T) is strongly background dependent and cannot be fitted with confidence whatever the back-gate voltage.

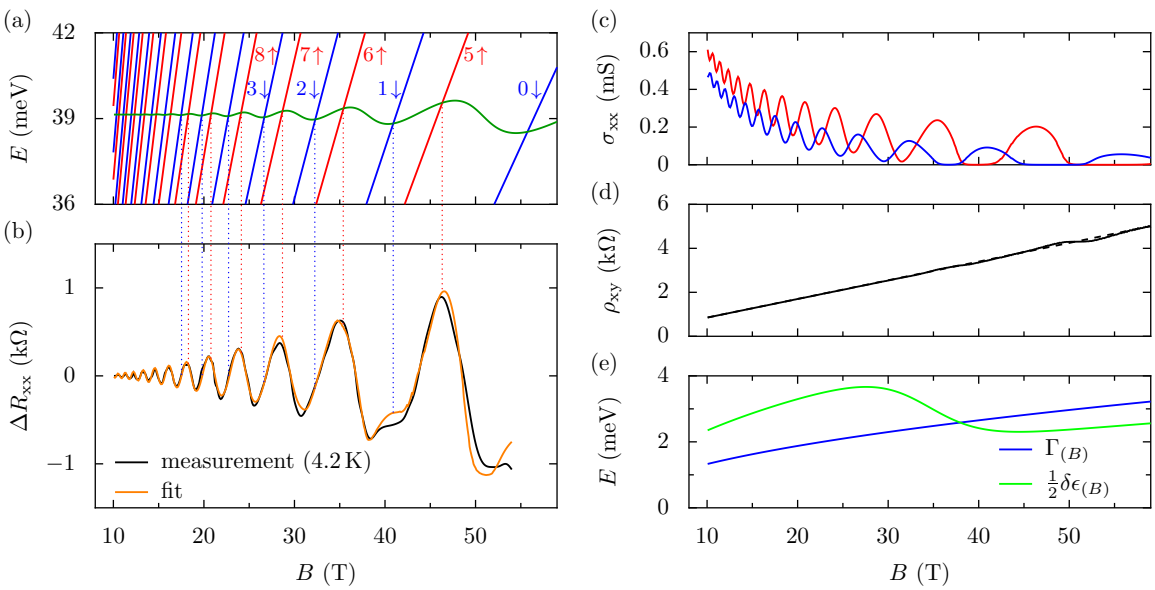

Figure 4.10: Output of the simulation for a given set of input parameters ($E_Z/E_c = 4.3$). a) The electrochemical potential (green curve) is displayed together with the Landau level spectrum for spin up (red lines) and spin down (blue lines). b) Experimental magneto-resistance (black curve) superimposed with the calculated one (orange curve). c) Longitudinal conductivity for spin up (red curve) and spin down (blue curve). d) The transverse resistivity computed using equation 4.7 (solid line) or from classical formula (dotted line). e) Landau level broadening $\Gamma(B)$ compared with the energy cut-off function $1/2\delta\epsilon(B)$.

The fit parameters n^h and ϵ_z/ϵ_c are the most significant and require special attention. The last section of this chapter is devoted to the magnetic-field independent ϵ_z/ϵ_c ratio and we focus here on the hole density evolution with respect to the back-gate voltage. Figure 4.12-a) indicates that the carrier density evolves linearly versus V_{BG} in agreement with the plane capacitor model $n^h = C_g\,(V_{BG} - V_0)$ where V_0 is an offset to the back-gate voltage reflecting the doping and $C_g = \left[\left(\frac{\epsilon_r^{\mathrm{SiO_2}}.\epsilon_0}{d_{\mathrm{SiO_2}}}\right)^{-1} + \left(\frac{\epsilon_r^{\mathrm{BN}}.\epsilon_0}{d_{\mathrm{BN}}}\right)^{-1}\right]^{-1}$ is the gate capacitance per unit area. The silicon oxide dielectric thickness is $d_{\mathrm{SiO_2}} = 280\,\mathrm{nm}$ and the relative dielectric permittivity is $\epsilon_r^{\mathrm{SiO_2}} = 3.9$. We take $\epsilon_r^{\mathrm{BN}} = 3.8$ while the BN thickness is an adjustable parameter, as well as V_0. The best fit provides $C_g = 11.5\,\mathrm{nF.cm^{-2}}$ and $V_0 = -8\,\mathrm{V}$, so that $d_{BN} = 20\,\mathrm{nm}$ in good agreement with the typical thickness of the deposited BN flakes.

The hole (quantum) mobility μ^h is another fit parameter of less importance, since it strongly depends on the way it is linked to Γ (see section 4.2.2). An alternative relation between μ^h and Γ than the one we adopted here - leading, for example, to a magnetic

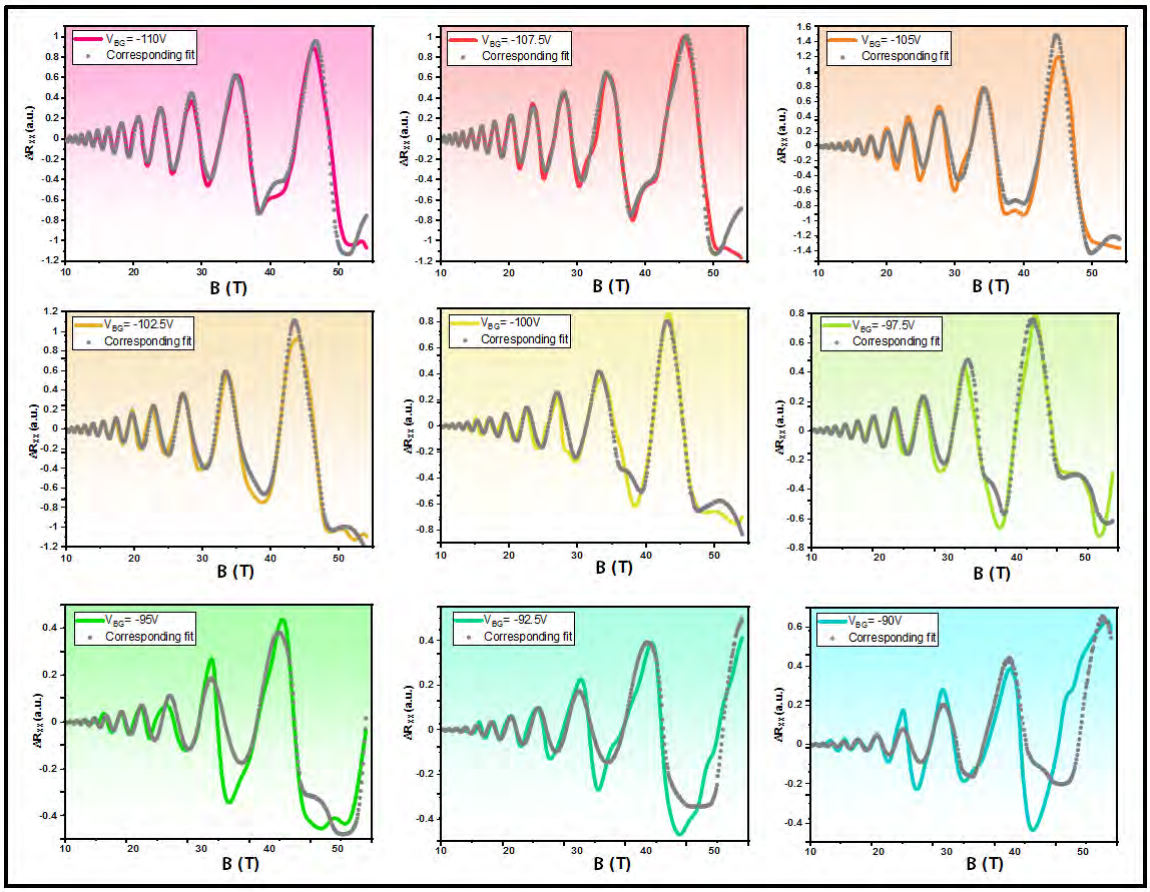

Figure 4.11: Experimental magneto-resistance superimposed with the simulated curves for selected back-gate voltages.

field independent broadening of the Landau levels - modifies the values of μ_h and the profile of the cut-off function, but has only very little influence on the quality of the fit. Therefore, even if the Hall effect would have been experimentally available, an eventual comparison of the extracted values of μ^h with the hole (transport) mobility would be inappropriate. We obtain $\mu^h \sim 2000\,\mathrm{cm^2V^{-1}s^{-1}}$ for $n^h \gtrsim 6.5 \times 10^{12}\,\mathrm{cm^{-2}}$, with a progressive drop down to $\mu^h \sim 1000\,\mathrm{cm^2V^{-1}s^{-1}}$ as the gate voltage increases (*i.e.*, lower hole density). Although uncertain, the absolute values of the hole mobility are in line to the expected ones considering the onset of the SdH oscillations at magnetic field B_{onset} set by the criterion $\mu^h.B_{onset} \sim 1$.

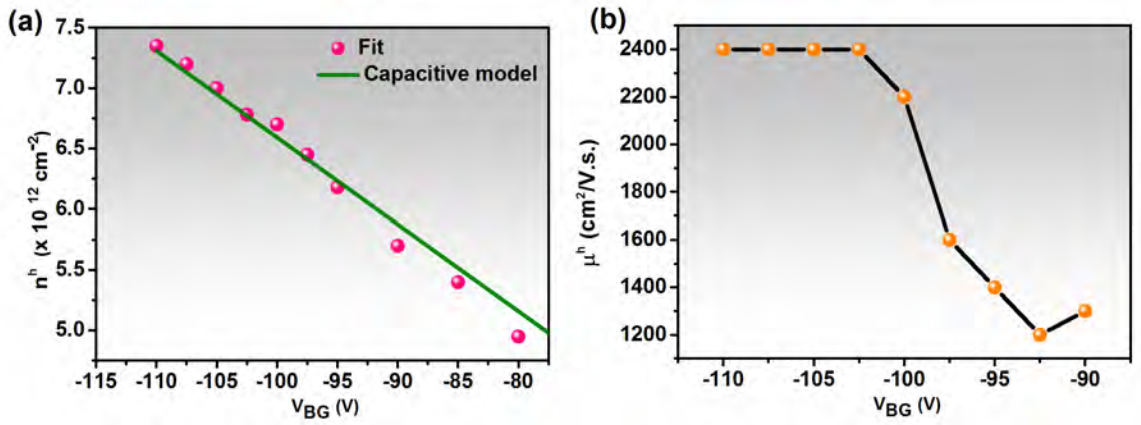

Figure 4.12: a) The hole carrier density extracted from the simulation (dots) and from the plane capacitor model (line). b) Extracted quantum hole mobility from the simulation.

4.3 Experimental determination of the Landé factor

4.3.1 Multiplicity of the ratio E_z/E_c

The carrier density and the ratio E_z/E_c are the most influential fit parameters. The former allows fitting mainly the weak magnetic field regime, where the Landau level broadening is large compared to cyclotron or Zeeman energy. In this regime, the quantum oscillations appear roughly 1/B-periodic and the period is almost solely determined by the carrier density. On the other hand, the ratio E_z/E_c is particularly influential in the high magnetic field regime, where strong departure from 1/B-periodic behavior is observed with the presence of extra peaks, valleys or inflections. Contrary to the carrier density, the value of E_z/E_c is not unique to properly fit the data. The multiplicity of this parameter is evidenced in figure 4.13: for weak enough magnetic field and/or high enough charge carrier concentration, the Landau level spectrum is exactly the same for a particular value of $E_z/E_c \pm N'$, where N' is an even integer. The magnetoresistance spectrum is essentially the result of scattering mechanisms between available states, it does not allow for a direct spin distinction. For a given magnetic field, the energy range where Landau levels of both spin are present constitutes the mixed regime whereas the polarized regime is established when Landau levels have the same spin index. Probing the polarized regime allows establishing the exact value of E_z/Ec, but this regime is experimentally difficult to reach. It requires either high quality samples for which transport properties can be probed at very low charge carrier density, or very high magnetic field, or both. In this work and for the

range of available hole densities, no hint of the polarized regime could be observed, despite magnetic fields as high as 55 T.

On the other hand, the parity of the integer part of the ratio E_z/E_c suffers no doubt. Indeed, a change of ± 1 of this parameter leads to a phase shift of π of the 1/B-periodic quantum oscillations for weak magnetic field. This phase shift could be easily counterbalanced with an adjustment of the carrier density, but this last one would become incompatible with the values expected from the plane capacitor model. We found that the ratio E_z/E_c is close to an even value for $V_{BG} = -110\,\mathrm{V}$. Furthermore, looking at equation 6.14, we notice that the relative amplitude of the quantum oscillations depends on the Landau level index. If the value E_z/E_c is offset modulo 2 and for the same carrier density, Landau levels with different indexes will cross the Fermi energy. We found that the fit quality is not satisfying for $E_z/E_c \sim 2$, whereas we would certainly be probing the polarized regime for $E_z/E_c \sim 6$ or higher. Therefore, this parameter is close to 4. Figure 4.13 illustrates the influence of E_z/E_c for the curve $\mathrm{V}_{BG} = -102.5V$, the best fit gives $Ez/Ec = 4.56$. If this ratio was offset by +2, an additional large amplitude peak corresponding to a spin-up/valley-K Landau level should be observed at $B = 52T$, indicating that the mixed/polarized Landau level transition would occur within our experimental magnetic field range.

4.3.2 Carrier density evolution of the g-factor

In section 4.2.2, we detailed the Landau level energy spectrum of Schrödinger particles which has been used to implement $E_{N,s}$ in the simulation. An alternative would be to use the Landau level energy spectrum of massive Dirac fermions (MDF) as suggested in [17]. Regarding transport properties only, the difference lies in the double spin/valley degeneracy of the 0th Landau level, as evidenced in figure 4.14 which compares the Landau level energy spectrum (at a given magnetic field) as a function of the ratio E_z/E_c. The Landau level energy spectra are identical for any given value of E_z/E_c in the massive Dirac fermion model and for $E_z/E_c + 1$ in the Schrödinger fermions (SCHF) model. As a consequence, the simulation provides exactly the same outputs and it is impossible to distinguish between the nature of the charge carriers. When the Zeeman energy is weaker than the cyclotron energy, e.g. when we know by other mean that the ratio E_z/E_c is not larger than 1, the two different models would translate into a shift of the SdH oscillations by half a period. This effect has been particularly put forward in graphene to distinguish its peculiar electronic properties (originating from massless Dirac fermions) from those of standard semiconducting 2DEG. However for systems such as TMDCs where E_z can be *a priori* several times larger than E_c, the distinction is impossible.

Figure 6.18 shows the ratio E_z/E_c extracted from the fit in the explored hole density

range. The black marks refers to the SCHF model where the $N = 0$ landau level is two-fold degenerate at zero magnetic field, whereas the gray dots correspond to the MDF model with broken symmetry of the zeroth Landau level for K and k' valleys. We note that E_z/E_c increases as the carrier density decreases. This trend is in line with the literature dedicated to WSe_2 monolayers, namely Movva *et al.* [13] and Gustafsson *et al.* [12] whose data have been digitized and reproduced in figure 6.18 to ease the comparison. In the former study, the E_z/E_c ratio takes integer values only, since the authors detected the magneto-resistance minima at even(odd)-integer values of the filling factor corresponding to odd(even)-integer E_z/E_c ratio. It is important to note, here, that only parts of their experimental results have been reproduced. The data (blue marks) can also be offset by +2 since the authors cannot experimentally distinguish between these two possible values of E_z/E_c. We have reproduced here the option which adjust best with our experimental data, despite theoretical studies [107, 106] in better agreement with the alternative case. In the latter study however, the E_z/E_c ratio is determined from the electrochemical potential jumps between two successive Landau levels, detected using a single-electron transistor coupled to the WSe_2 monolayer. Interestingly, the MDF model is assumed in reference [13] whereas the authors of reference [12] published their data considering the SCHF model. To ease the comparison, we used vivid color for data corresponding to the SCH model and light color for the MDF model, where the values of E_z/E_c are downshifted by 1. Although our estimation of E_z/E_c is coherent with the values reported by other groups, the inevitable discrepancies may originate from experimental data precision, limitations of the model, or the nature/strength of disorder.
The numerical simulations indicate that, in first approximation, the ratio E_z/E_c does not change with magnetic field. Therefore the reported values of E_z/E_c (as well as $g\star$) in figure 4.15 correspond to the zero-magnetic field case. However, this assertion would certainly fail at higher magnetic field (or lower carrier density), when the system is driven into the polarized regime. Further investigations with higher quality samples are necessary to address this issue. The effective Landé factor is linked to the ratio E_z/E_c through the relation $g^* = \frac{2m_e}{m^*} \times \frac{E_z}{E_c}$. Importantly, the effective Landé factor contains information relative to the strength of the electron-electron interactions as discussed in section 2.2.4. The interaction enhancement of g^* can be intuitively explained by considering the competition between the kinetic and Coulomb interactions. Indeed, within the Hartree-Fock approximation, the exchange energy between two charged particles of same spin is negative and tends to lower the total energy of the system. Therefore, a system composed of particles with the same spin state is favored as the exchange energy increases relative to the kinetic energy. The spin polarization of the system can be measured from the spin susceptibility χ, which

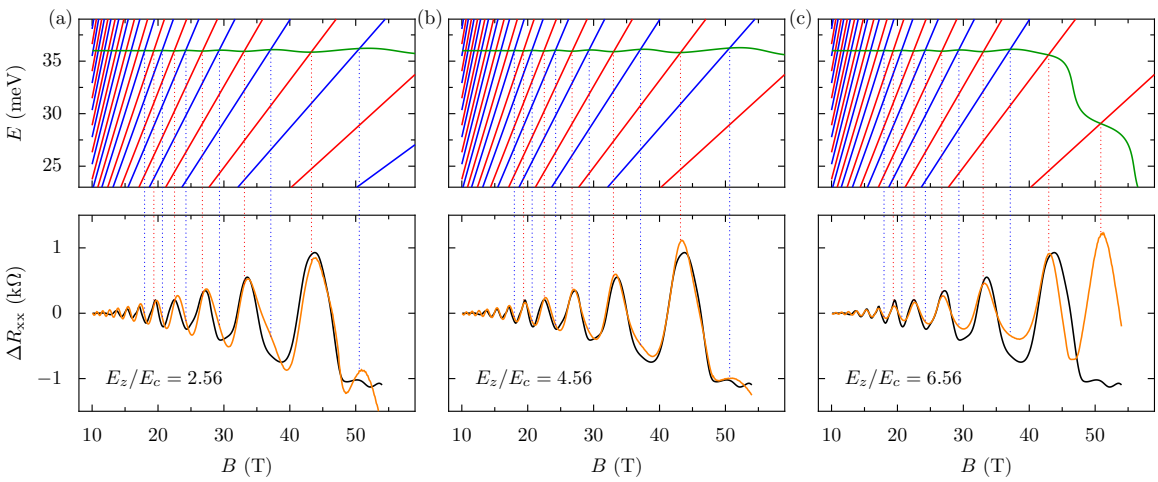

Figure 4.13: Simulation results (orange curves) are compared to the experimental data for $V_{BG} = -102.5\,V$ (black curve), for different possible values of E_z/E_c offset by ± 2. a) For $E_z/E_c = 2.56$, the overall fit is fair but the 1/B-periodic oscillations in the weak magnetic field regime is questionable. b) The best fit is obtained for $E_z/E_c = 4.56$ c) For $E_z/E_c = 6.56$, a transition from the mixed to polarized regime is expected, but not observed experimentally.

is directly linked to g^*.

Actually, the interaction enhancement of the spin susceptibility is better described by the ratio $\chi/\chi_0 = \frac{g^*.m^*}{g_b.m_b}$ where χ_0 is the Pauli susceptibility in the absence of interactions (e.g. g-factor g_b and mass m_b are solely determined from the band-structure). To resume, when the electron-electron interaction increases, so does the exchange energy which tends to favor a spin-polarized state. As a consequence, the spin susceptibility increases as well as the effective Landé factor. The relative strength of the electron-electron interaction is evaluated from the dimensionless parameter r_s defined as the ratio between the Coulomb interaction and the kinetic energy of a particle. In two-dimensional systems, the Coulomb energy writes $\epsilon_{ee} = \frac{q^2\sqrt{\pi.n^h}}{4\pi\epsilon_0\epsilon_r}$ whereas the kinetic energy is $\epsilon_c = \frac{\hbar^2\pi.n^h}{m^*}$. The ratio between these two energy terms is therefore $r_s = \frac{1}{a_B\sqrt{\pi.n^h}} \equiv$ where $a_B = \frac{\hbar^2.4\pi\epsilon_0\epsilon_r}{m^*.q^2}$ is the effective Bohr radius. Considering a_B as a normalization factor, this ratio can be interpreted as the mean distance between the charged particles, regardless the material. The introduction of the effective Bohr radius ($a_B = a_0 \times (\epsilon_r.m_e/m^*)$ where $a_0 = 4\pi\epsilon_0\hbar^2/m_e.q^2$ is the Bohr radius) avoids considering the effect of the medium which inevitably affects the interaction distances. We note that r_s decreases as the carrier density increases or, in another words, the relative strength of electron-electron interactions is enhanced at low carrier density.

The ratio E_z/E_c and the hole density have been converted to g^* versus r_s in figure 4.16 where we assume an interaction independent effective mass $m^* = m_b = 0.45.m_e$. Although the value of the band g-factor for WSe_2 monolayers remains controversial [21, 12, 20, 22], its enhancement with interaction strength is clear even for moderate values of r_s. This study[1] evidences an interaction enhanced g-factor in WSe_2 monolayers for higher hole densities than those reported in the literature.

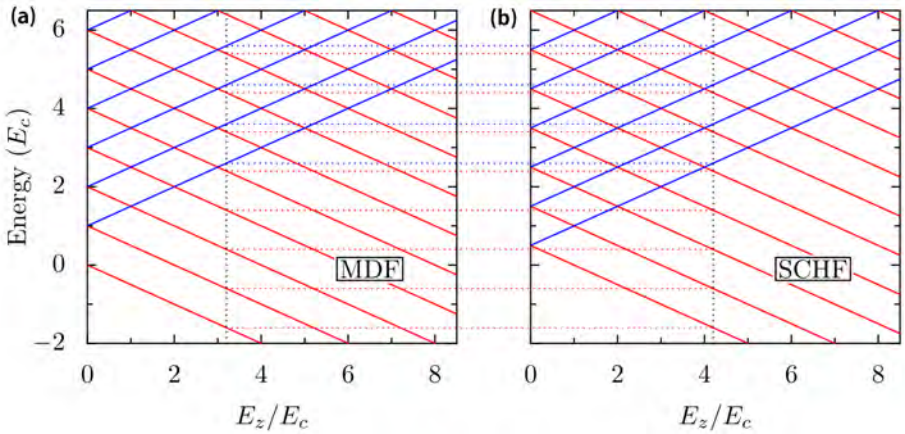

Figure 4.14: a) Comparison of the Landau level energy spectrum between the massive Dirac fermion (MDF) model and the Schrödinger (SCHF) fermion model at a given magnetic field. The same Landau level spectra are evidenced here with $E_z/E_c = 3.2$ for the MDF model and $E_z/E_c = 4.2$ for the SCHF model.

4.4 Concluding remarks

We would like to highlight here the hypothesis and limitations of the study presented in this chapter. First, the experimental results are subjected to doubts considering the geometry of the investigated sample which does not meet the required standards for proper measurement of the longitudinal resistivity. Indeed, the presence of a large WSe_2 flake in electrical contact with the investigated monolayer may affect the equipotentials and current lines in an unpredictable way, even if the current injection and voltage measurement electrodes are not directly connected to it. Even if the experimental data have been checked using either opposite magnetic field or current (or both), we cannot exclude the eventual contribution of this large flake as well as the non-perfect Hall bar geometry of the device. This point can be addressed in the future by etching the sample into a proper Hall bar. Next, the data treatment for

[1] Part of this work was published in [110]

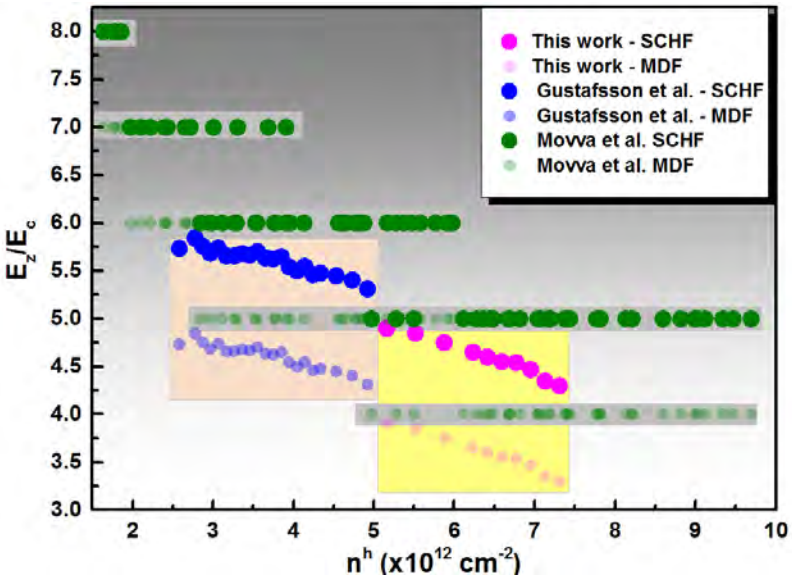

Figure 4.15: Extracted values of Ez/Ec as a function the hole density. The pink dots are the values obtained assuming the SCHF Landau level structure. By down-shifting these values by 1 (light pink dots), we obtain the values corresponding to the MDF Landau levels (LLs) structure. The E_z/E_c ratio is compared to the values found in the literature (blue and green dots), where either the MDF (light color) or SCHF (vivid color) model was considered. Only parts of the experimental data (see main text for details).

background removal of the magneto-resistance is questionable, especially for small hole concentrations where the quantum oscillations are difficult to extract from a large and noisy background. The procedure is manual and therefore user-dependent, affecting mainly the shape and the amplitude of the oscillation extrema. The magnetic field location of the extrema are also affected, but to a lesser extent. Indeed, the related periodicity of the oscillation is a quite robust parameter which is only slightly affected by data treatments. Regrettably, the Hall effect could not be measured because of the sample shape and geometry. Although we had no choice but to simulate the transverse magneto-resistance to properly compute its longitudinal counterpart, we found out that the Hall effect has only very little influence for studying the quantum oscillations. For $\rho_{xy}.\sigma_{xx} << 1$ and considering $\rho_{xy}(B)$ as a smoothly varying function in comparison to the quantum oscillations, we have $\rho_{xx} \sim \sigma_{xx}$. Nevertheless, an experimental access to the Hall effect would have been highly desirable to confirm the carrier density (which wouldn't be an adjustable parameter anymore) and to analyze the Hall plateaus at high field.

There is no exact simple theoretical model to properly fit our experimental data.

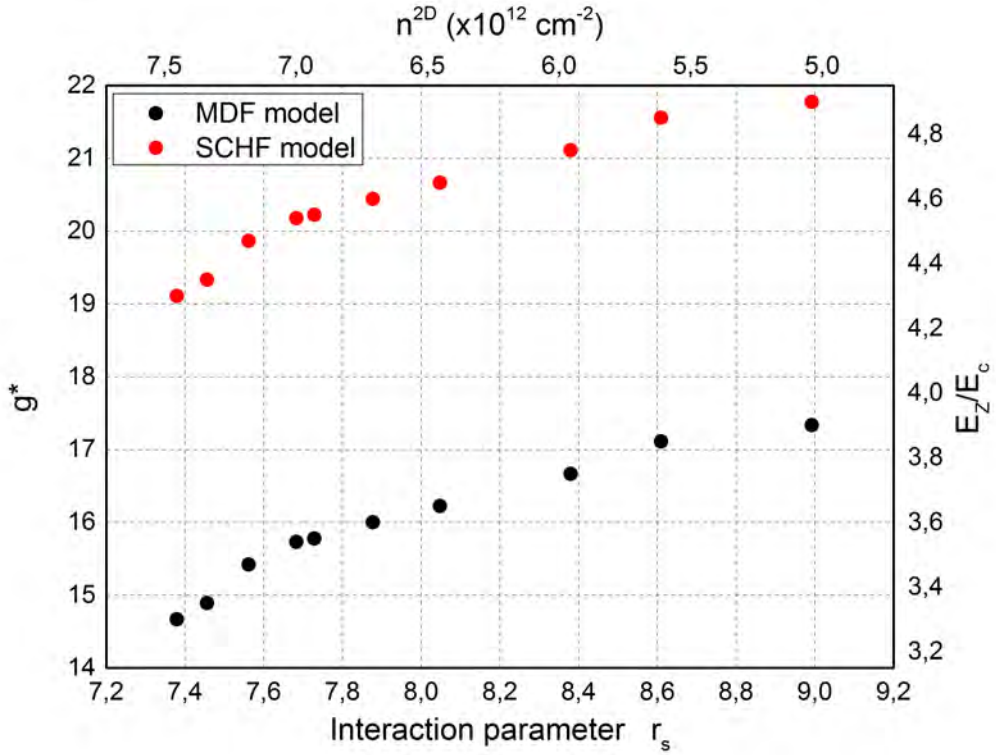

Figure 4.16: Evolution of the Landé factor g^* (left) and the ratio E_z/E_c (right) versus the interaction parameter r_s (bottom) and the carrier density n^h (top) as a function of the carrier density, on the same graph, for two different models. g^* increases as the interaction parameter r_s increases, evidencing an interaction enhanced g-factor in this system. We used $\epsilon_r^{WSe_2,BN} = 1/2.\left(\epsilon_r^{vacuum} + \epsilon_r^{BN}\right) = 2.4$ to compute r_s.

The interplay between the mean scattering time and the Landau level-based density of states is a complex and unknown function, in addition to the eventual localization effects which depends on the microscopic sample details and boundaries of the sample. The use of equation 6.14 is therefore rather inadequate, especially because it was established for scattering centers with short-range potentials. The exact nature of disorder in our sample is certainly a mixture of short-range and long-range defect potentials. This difficulty is addressed phenomenologically by the introduction of a magnetic-field dependent cut-off function of the broadened Landau levels, which acts similar as a mobility edge in the quantum Hall regime. This cut-off function could in principle be related to the localization length, although this quantity is difficult to evaluate without experimental access to the fully developed quantum Hall regime.

We also recall that the exact broadening of the Landau levels is unknown, although we chose a Gaussian broadening adapted for short range defects [67] and long range scatterers where the correlation length of the potential fluctuations is larger than $\ell_B/N^{1/2}$ [105]. Because this condition cannot be verified, it is assumed in the present work.

Despite possible errors in experimental data treatment and the lack of physical justification for some hypothesis in the model, the quality of the magneto-resistivity fit is remarkable for the highest hole density curves, without invoking a field dependence of the ratio E_z/E_c. One of the key ingredient for this success is the self-consistent calculation of the chemical potential, which goes beyond the Lifschitz-Kosevich formula (see section 6.11). Indeed, simulations performed with a magnetic-field independent electrochemical potential reproduces well the low field part of the experimental data, but fail to address properly the high field regime. The relation between the carrier density and the electrochemical potential is provided by equation 6.13. When the hole concentration is constant, the chemical potential must vary. However if the chemical potential is set constant, the carrier density must be magnetic field-dependent. Although real systems are certainly a mixture of these two ideal cases, we believe that the first condition mostly apply for our sample. Indeed, in the plane capacitor geometry, the charge carrier density is related to the total capacitance of the device, including the geometrical and quantum capacitance. The former is very small (considering the large SiO_2 thickness) and dominates the total capacitance. Since this quantity does not depend on the magnetic field, so does the related carrier density.

The simulation is helpful to analyze quantum oscillations from a sample with partial Landau level resolution, e.g. with moderate mobility. However, it would be interesting to reproduce this study with a sample of higher quality. One route to achieve this goal is to fabricate a fully h-BN encapsulated WSe_2 monolayer [16, 13, 12], even if ohmic contact are difficult to achieve in this configuration. The enhancement of the Landé factor certainly depends on disorder and it would be interesting to address this issue with higher mobility samples.

Chapter 5

Conclusion

At cryogenic temperature and under high enough magnetic field, the magnetic confinement of the quasi-particle wave-functions is no more hindered by the disorder. Their subsequent energy quantization into Landau levels reflects some of the fundamentals properties of the host material. In a magneto-transport experiment, the quasi-particle energy spectrum is inferred from the variations of the electrical resistance which is intimately linked to the energy dependent mean scattering time at the Fermi energy. In other words, the magnetic field acts as a tunable knob which changes the Hamiltonian of the system, and the resulting quasi-particle energy spectrum is experimentally probed by the electrical resistance. The comparison between the experimental results and the theoretical models contributes to unveil the specific charge carrier dynamics of a material. This work is dedicated to the study of the electronic properties of monolayer tungsten diselenide (WSe_2) by mean of high magnetic field magneto-transport.

This system has been chosen for several reasons. First, it hosts a two-dimensional gas of charged particles since its thickness reaches the ultimate limit of one stochiometric unit cell. The electronic properties of two-dimensional materials are much different from their bulk counterparts due to the breaking of translational symmetry in one direction. A detailed knowledge of their electronic properties is essential for their integration into future opto-electronic devices. Second, WSe_2 material belongs to the family of transition metal dichalcogenides which are expected to host a new type of quasi-particles named "massive Dirac fermions" when thinned down to a monolayer. Unlike massless Dirac fermions in graphene or Schrödinger fermions in conventional 2D semiconductor systems, the massive Dirac fermions are characterized by both the presence of a direct energy gap and a locking of the spin and valley degrees of freedom. Third, the large effective mass of the holes ($m^* \sim 0.45 \times m_e$) and the low effective dielectric constant of the medium surrounding the monolayer (typically vacuum and hexagonal boron nitride in this study) allows for large interaction parameter. This system is therefore a very interesting platform to study electron-electron interactions.

Actually, due to the energy gap, magneto-optical spectroscopic techniques are particularly adapted to study the electronic properties of monolayer WSe_2. On the contrary, their investigation by mean of the magneto-transport technique remains challenging. The main difficulties are inherent to the quality of the sample (electronic mobility as the main metric of the degree of disorder) and to the electrical contacts with metallic electrodes. The choice of this technique is however motivated since it is sensitive to the degeneracy of the lowest energy Landau level. This property constitutes the

hallmark of the nature of the charge carriers, so that magneto-transport experiments allow for a direct experimental distinction between massive Dirac and Schrödinger fermions in monolayer WSe_2 (provided the Zeeman energy is already known or negligible).

After several attempts, a multiply connected monolayer WSe_2 device with decent electronic mobility and contact resistances has been fabricated. The monolayer lies on hexagonal boron nitride flake itself deposited on a SiO_2/Si substrate, allowing an *in situ* change of the carrier density by electrostatic doping using a back-gate. The as-fabricated device is insulating at cryogenic temperature (4.2 K), but starts conducting when the back-gate voltage is negative. In this configuration, the Fermi energy is closed to the top of the valence band and the electronic properties of holes are probed. The high magnetic field resistance displays a complex quantum oscillation pattern suggesting a competition between the Zeeman energy E_z and the cyclotron energy E_c. We emphasize here the use of strong magnetic fields which were essential to compensate the moderate electronic mobility of the sample in order to reach the quantum transport regime. The data analysis, based on the comparison of the experimental results with simulations involving, among others, the Zeeman energy, allowed to extract the effective Landé factor as a function of the interaction parameter. In agreement with the literature, we confirmed and enlarged the carrier density range where the enhancement of the effective Landé factor has been reported. For systems with negligible Zeeman energy such as graphene, the phase of the quantum oscillations can be related to the nature of the quasi-particles. In this study, on the other hand, the large (several times the cyclotron energy) and *a priori* unknown Zeeman energy prevents an unambiguous determination of the ratio Ez/Ec, which is inferred ± 1 depending on the nature of the charge carriers. An independent measurement of the Zeeman energy is required to address this issue.

A straightforward new research direction would be to study magneto-transport in higher quality samples. Disorder is an important parameter which competes with interaction effects in two dimensional electron gas. With access to higher quality materials, the fully developed quantum Hall regime, the polarized Landau level regime or even the fractional quantum Hall regime could be at reach. This goal can be achieved with cleaner sample fabrication techniques and encapsulation of the monolayer with top and bottom boron nitride flakes. In this configuration however, the fabrication of electrical contacts with low contact resistance remains challenging and requires state-of-the-art clean room processes. The use of graphene or thin graphite as an interlayer between the WSe_2 monolayer and the metallic electrodes is a promising route towards this objective. Besides, probing the electronic properties of the conduction band by

mean of magneto-transport is another interesting perspective for this material. Despite several attempts, it was not possible to align the Fermi energy with the bottom of the conduction band in this study. The choice of a metal with appropriate work function for the contacting electrodes can certainly help reaching this goal.

Chapter 6

Résumé en français

Contents

6.1 Introduction **99**

6.2 Propriétés électroniques des dichalcogénures de métaux de transition **100**

6.2.1 Généralités 100

6.2.2 Monocouche 100

6.2.3 Bicouche 102

6.2.4 Multi-couche 103

6.3 Transport électronique **104**

6.3.1 Modèle classique de Drude 104

6.3.2 Transport sous champ magnétique intense 105

6.4 Fabrication des dispositifs et caractérisation électrique **108**

6.4.1 Dichalcogénures de métaux de transition : de 3D à 2D . . 108

6.4.2 Fabrication et adressage électrique des échantillons 109

6.4.3 Caractérisation structurale et mesure de l'épaisseur des flocons h-BN/WSe_2 110

6.4.4 Caractérisations électriques 111

6.4.5 Génération de champ magnétique pulsé 112

6.5 Oscillations quantiques dans une monocouche de WSe_2 dopée P **114**

6.5.1 Caractérisation des échantillons et magnéto-transport . . . 114

6.5.2 Simulation du magnéto-transport 116

6.5.3 Détermination expérimentale du facteur de Landé 118

6.6 Conclusion **120**

6.1 Introduction

Contrairement au graphène, les dichalcogénures de métaux de transition ont une bande interdite séparant la bande de valence de la bande de conduction. Cette bande interdite est indirecte dans les matériaux massifs et devient directe lorsque le matériau est aminci à un seul plan stœchiométrique atomique. Au-delà des applications opto-électroniques évidentes, un couplage spin-orbite important fait des monocouches de dichalocogénures de métaux de transition un système particulièrement intéressant pour la recherche fondamentale. En effet, leurs propriétés électroniques impliquent deux degrés de liberté (appelés spin et vallée) qui sont fortement couplés

par l'interaction spin-orbite. Cette thèse expérimentale s'intéresse en particulier à la mono-couche de diséléniure de tungstène (WSe_2). Nous utilisons des conditions extrêmes de champ magnétique intense et de basse température pour quantifier le spectre d'énergie des porteurs de charge en niveaux d'énergie discrets (niveaux de Landau), qui affectent à leur tour les propriétés de transport électrique. Ainsi, la magnéto-résistance constitue l'empreinte digitale du système permettant de révéler son état fondamental. Ce travail constitue la première réalisation de mesures de transport quantique sur des mono-couches de WSe_2 à l'aide d'un champ magnétique pulsé. Il ouvre la voie à de futures améliorations techniques et à la mesure d'autres matériaux de la famille des dichalcogénures de métaux de transition.

6.2 Propriétés électroniques des dichalcogénures de métaux de transition

6.2.1 Généralités

Il existe environ 60 composés différents appartenant à la famille des dichalcogénures de métaux de transition (DCMTs). Les deux tiers d'entre eux possèdent une structure en couches de la forme MX_2 [25], où M représente les atomes des métaux de transition (groupes 4 à 10 du tableau périodique des éléments) et X représente des atomes chalcogènes. Les mono-couches de DCMT sont constituées d'atomes M pris en sandwich par deux couches d'atomes X, qui sont fortement liés par des liaisons covalentes. Dans une structure 3D, de nombreux plans stœchiométriques sont empilés les uns sur les autres et interagissent par des interactions faibles de van der Waals (vdW) [25]. Les DCMTs existent sous trois formes appelées 1T, 2H et 3R. Dans cette nomenclature, le nombre indique le nombre de couches MX_2 présentes dans la cellule unité tandis que la lettre représente le groupe de symétrie (T pour trigonal, H pour hexagonal, R pour rhomboédrique) [32]. Ces polymorphes sont schématisés sur la figure 6.1.

6.2.2 Monocouche

Réseau direct et réseau réciproque

Dans la figure 6.2, les expressions (1) et (2) définissent $\vec{a_1}$ et $\vec{a_2}$ comme les vecteurs primitifs du réseau direct exprimés selon les vecteurs de la base cartésienne $\hat{x}$ et $\hat{y}$. La cellule unité contient un atome de métal et deux atomes de chalcogène. Les expressions (3) et (4) définissent les vecteurs de base du réseau réciproque $\vec{b_1} = \frac{2\pi}{a^2}\left(\vec{a_2} \wedge \vec{k}\right)$ et $\vec{b_2} = \frac{2\pi}{a^2}\left(\vec{k} \wedge \vec{a_1}\right)$ où $\vec{k} = \hat{x} \wedge \hat{y}$ est un vecteur unitaire orienté dans la direction hors du plan. La figure 6.2-b montre l'espace réciproque comprenant les

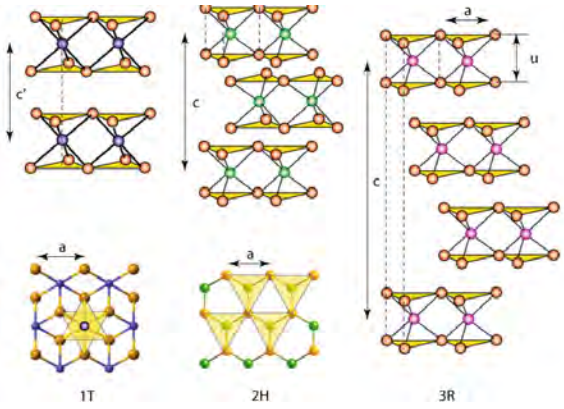

Figure 6.1: Schémas des polymorphes de DCMT de gauche à droite : 1T (symétrie tétragonale, une couche par cellule unité, coordination octaédrique de l'atome métallique), 2H (symétrie hexagonale avec deux couches par cellule unité, coordination prismatique trigonale de l'atome metallique) et 3R (symétrie rhomboédrique avec trois couches par cellule unité, coordination prismatique trigonale de l'atome métallique). Adapté de [28]

points de haute symétrie K, K', Γ et M ; les lignes T, T' et Σ ainsi que les points Q et Q' situés à mi-chemin le long de la ligne $\Gamma - K$ et $\Gamma - K'$. Les six coins de la première zone de Brillouin se trouvent aux points K et K', qui sont inéquivalents.

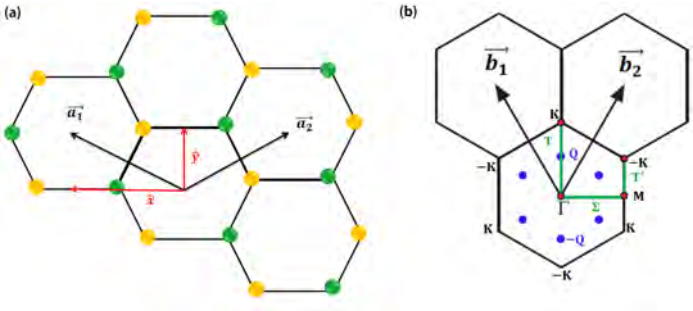

$$\vec{a_1} = \frac{a}{2}(\sqrt{3}\hat{x} + \hat{y}) \quad (6.1)$$
$$\vec{a_2} = \frac{a}{2}(-\sqrt{3}\hat{x} + \hat{y}) \quad (6.2)$$
$$\vec{b_1} = \frac{2\pi}{a}(\frac{\sqrt{3}}{3}\hat{x} + \hat{y}) \quad (6.3)$$
$$\vec{b_2} = \frac{2\pi}{a}(-\frac{\sqrt{3}}{3}\hat{x} + \hat{y}) \quad (6.4)$$

Figure 6.2: a) réseau réél et b) réseau réciproque d'une monocouche de DCMT.

Structure de bande

Les états quantiques électroniques doivent être décrits en prenant en compte l'interaction spin-orbite provenant des orbitales d des atomes métalliques [15]. La symmétrie de réflexion miroir modifie la projection hors du plan d'un état de spin, tandis que sa composante dans le plan reste inchangée. Cependant, la symétrie d'inversion du temps impose un renversement des états de spin lorsque ceux-ci appartiennent à des états électroniques des vallées **K** et **K'** [42, 43]. Ainsi les états quantique sont dégénérés en spin qui est perpendicluaire au plan de la monocouche. Cette propriété importante est représentée dans la figure 6.3 où la levée de degenérescence de spin aux extrema de la bande de valence et de la bande de conduction est interchangée selon l'indice de vallée **K** et **K'**. La bande interdite de spin/vallée est plus grande dans la bande de valence par rapport à celle de la bande de conduction pour les monocouches à base

de tungstène. Ce couplage spin/vallée est inhérent aux TDMCs dont le nombre de couches est impair, incluant la monocouche. Ces systèmes ont en commun l'absence de symétrie d'inversion contrairement aux DCMTs ayant un nombre de couches pair.

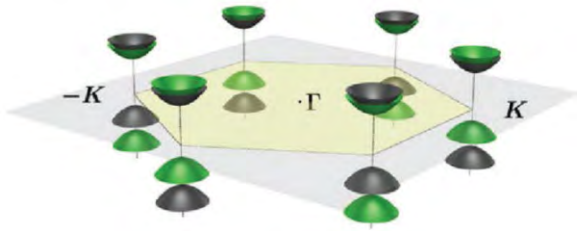

Figure 6.3: Levée de la dégénérescence de spin aux points K et K' de la première zone de Brillouin d'une monocouche de WSe_2. Adapté de [9]

6.2.3 Bicouche

La cellule unité de la bicouche de DCMTs est le double de celle d'une monocouche, où les couches supérieures et inférieures sont tournées dans le plan de 180° l'une par rapport à l'autre. Ce système possède un point de symmétrie d'inversion et donc, même en présence d'un couplage spin-orbite fort, les états électroniques de spin restent dégénérés. En réalité, les deux couches n'interagissent que faiblement via les forces de van der Waals et les propriétés electroniques des bicouches de DCMTs ressemblent, à première vue, à celles de deux monocouches indépendantes tournées de 180° l'une par rapport à l'autre. Cette opération de symétrie commute les deux vallées K et K' (voir figure 6.4) mais laisse le spin inchangé. Ainsi, les propriétés dépendantes de l'indice de vallée se moyennent naturellement à zéro (par exemple effet Hall de vallée, dichroïsme circulaire de vallée) tandis que les effets dépendants du spin s'additionnent (effet Hall de spin et dichroïsme optique de spin). Le signe de l'énergie de clivage de spin est intimement lié à la vallée ainsi qu'à l'indice de couche, qui constitue un nouveau degré de liberté pour les états électroniques (par exemple, la fonction d'onde électronique peut être considéré comme une superposition linéaire de deux fonctions d'onde entièrement localisées soit sur la couche supérieure, soit sur la couche inférieure). Dans le composé WSe_2, le couplage spin-orbite est particulièrement fort et l'énergie de clivage de spin est beaucoup plus grande que l'énergie de saut entre les couches. Il s'ensuit que les états quantiques de spin up (down) sont localisés dans la couche inférieure (supérieure) en fonction de l'indice de vallée. Ainsi et en première approximation, la physique impliquant les indices de vallée reste similaire à celle impliquant deux monocouches découplées. Néanmoins, il est important de souligner qu'un champ électrique perpendiculaire brise la symétrie d'inversion [26] et restaure les propriétés dépendantes de l'indice de de vallée. Par exemple, l'absence de symétrie d'inversion dans les bicouches de MoS_2 et WSe_2 a été mis en évidence par l'application d'un champ électrique perpendiculaire dans les références [16, 13].

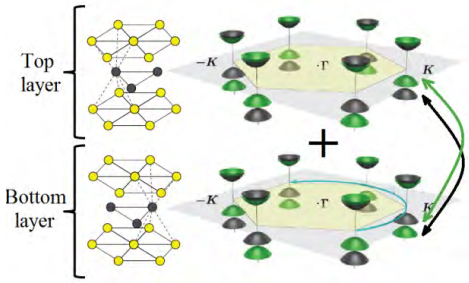

Figure 6.4: Les propriétés électroniques des bicouches DCMT ressemblent à celles de deux DCMT monocouches tournées de 180° l'une par rapport à l'autre. Dans l'espace réciproque, les bords de la première zone de Brillouin (points K et K') sont une superposition des états de chaque monocouche, conduisant à des états de spin dégénérés.

6.2.4 Multi-couche

Dans les multi-couches de DCMTs, les minima des bandes de conduction ne sont pas situés aux points K/K', mais plutôt aux points Q/Q' et Γ avec une relation de dispersion quadratique dans leur voisinage comme le montre la figure 6.5. Pour les DCMTs ayant un nombre de couches pair, les vallées Q et Q' sont reliées par des éléments de symétrie d'inversion de temps et d'inversion par rapport à un point [55]. La symétrie d'inversion est toutefois absente dans les DCMTs ayant un nombre de couches impair de sorte que toutes les sous-bandes aux points Q/Q' sont non-dégénérées en spin. Pour un état électronique donné et en première approximation, le couplage entre les indices de spin et de vallée dans les DCMTs monocouches et bicouches peuvent être étendues aux multi-couches de DCMTs, en considérant cependant les vallées Q/Q' au lieu des vallées K/K' [56].

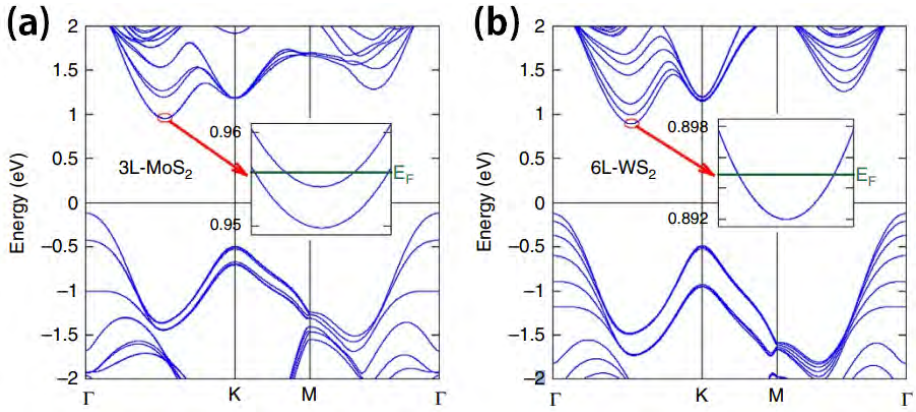

Figure 6.5: (a),(b) structure de bande calculée pour tricouche MoS_2 et 6-couches WS_2. Adapté de [56].

6.3 Transport électronique

6.3.1 Modèle classique de Drude

Le transport électronique implique le mouvement de charges (le courant) sous l'influence de champs électriques et/ou magnétiques. Dans les systèmes diffusifs, les porteurs de charge sont d'une part accélérés par les champs moteurs, d'autre part dispersés et/ou ralentis lors de collisions. Ces interactions opposées conduisent à une vitesse moyenne constante des porteurs de charge appelée vitesse de dérive $\vec{v_d}$. Le traitement classique de la conduction repose sur le modèle de Drude, qui introduit un temps de diffusion moyen pour prendre en compte les processus de diffusion. Nous définissons la densité de courant $\vec{j}$ comme le produit de la densité de porteurs n par la vitesse de dérive $\vec{v_d}$ et la charge élémentaire q, qui peut être respectivement négative ou positive pour les électrons ou les trous.

$$\vec{j} = q.n.\vec{v_d} \tag{6.5}$$

La conductance électrique sonde la diffusion globale des porteurs de charge ayant lieu à un niveau microscopique dans le matériau. En régime stationnaire, la vitesse de dérive divisée par le temps de diffusion moyen définit une accélération qui, multipliée par la masse effective des porteurs de charge, équivaut à une force opposée à celle produite par le champ électrique externe. On peut définir la mobilité μ d'un matériau comme le rapport entre la vitesse de dérive et le champ électrique et, en appliquant la loi de Newton, nous montrons que la mobilité s'exprime alternativement en fonction du temps de diffusion moyen, de la masse effective et la charge des porteurs.

$$\underbrace{q.\vec{E}}_{\vec{F}_c} - \underbrace{m^*.\vec{v}_d/\tau}_{\vec{F}_{drift}} = 0 \Leftrightarrow \mu = \frac{|\vec{v}_d|}{|\vec{E}|} = \frac{q\tau}{m^*} \tag{6.6}$$

En combinant les équations 6.5 et 6.6, la densité de courant peut s'écrire en fonction du champ électrique où le facteur de proportionnalité définit la conductivité σ_0 du matériau. En l'absence de champ magnétique, la résistivité est l'inverse de la conductivité.

$$\sigma_0 = \frac{q^2.\tau.n}{m^*} = n.q.\mu \tag{6.7}$$

$$\rho_0 = \frac{m^*}{q^2.\tau.n} = 1/(n.q.\mu) \tag{6.8}$$

Le modèle classique de Drude décrit la dynamique d'une particule chargée dans un milieu désordonné de manière homogène et sous l'influence d'un champ électrique externe. Le modèle suppose que tous les électrons de conduction se comportent de

manière similaire, de sorte que les observables macroscopiques (conductivité, courant..) sont obtenus en multipliant la dynamique d'une particule par la densité des porteurs de charge. Cette approche simple de la conductivité du matériau fournit le point de départ d'une théorie plus complexe (semi-classique) prenant en compte les concepts de la physique statistique où la fonction de distribution de Fermi-Dirac est introduite. En prenant en compte le champ magnétique, la conductivité devient un tenseur qui couple les composantes de la densité de courant et les composantes du champ électrique. Le tenseur de conductivité (9) et de résistivité (10) sont donnés dans la figure 6.6 en fonction du champ magnétique. Une approche plus complète, à partir de l'équation de Boltzmann est décrite dans le manuscrit de thèse.

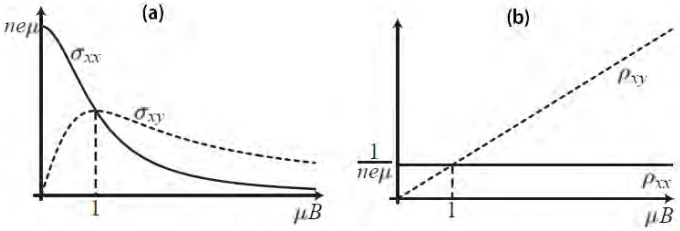

Figure 6.6: Composantes du tenseur de conductivité (a) et de résistivité (b) en fonction du champ magnétique.

$$\sigma = \begin{pmatrix} \frac{\sigma_0}{1+(\mu.B)^2} & \frac{\sigma_0.\mu.B}{1+(\mu.B)^2} \\ -\frac{\sigma_0.\mu.B}{1+(\mu.B)^2} & \frac{\sigma_0}{1+(\mu.B)^2} \end{pmatrix} \quad (6.9)$$

$$\rho = \begin{pmatrix} \rho_0 & -\rho_0.\mu.B \\ \rho_0.\mu.B & \rho_0 \end{pmatrix} \quad (6.10)$$

6.3.2 Transport sous champ magnétique intense

Niveaux de Landau

Lorsque le champ magnétique est suffisamment fort, les porteurs de charge peuvent réaliser au moins une orbite cyclotron avant d'être diffusés. Dans cette description semi-classique, l'orbite circulaire électronique doit correspondre à un nombre entier de fois la longueur d'onde $\lambda = \frac{2\pi}{k} = \frac{h}{p}$. Cette contrainte est nécéssaire puisque la fonction d'onde électronique ne peut pas être définie de manière multiple (c'est à dire avoir une phase différente) à une position donnée. Classiquement, une particule chargée de masse effective m^* et de charge q a un mouvement circulaire en présence d'un champ magnétique externe avec une pulsation constante $\omega_c = q.B/m^*$. On note $\vec{r}$ le rayon et $\vec{v} = \vec{\omega}_c \wedge \vec{r}$ la vitesse de la particule. La phase acquise lorsque la particule chargée se déplace le long de son orbite est $d\varphi = d\left(\vec{k}.\vec{r}\right)$ où $\hbar.\vec{k} = m^*.\vec{v} - q.\vec{A}$. Nous calculons:

$$2\pi.N = \int_{circ} d\varphi = \int_{circ} \vec{k}.\vec{d\ell} = \frac{1}{\hbar}\left[2\pi.m^*.r^2.\frac{e.B}{m^*} - q.B.\pi.r^2\right]$$

$$2\pi.\hbar.N = \pi.r^2.q.B \Leftrightarrow r = \sqrt{2.N}.\ell_B$$

où $\ell_B = \sqrt{\frac{\hbar}{e.B}}$ est la longueur magnétique. Bien que ce modèle heuristique prédise la quantification du rayon du cyclotron et de l'énergie cinétique d'une particule chargée libre en présence d'un champ magnétique, l'interprétation correcte nécessite un traitement mécanique quantique complet détaillé dans le manuscrit de thèse, conduisant au spectre des niveaux de Landau. Nous montrons que la densité d'états d'un gaz d'électrons bidimensionnel sous champ magnétique perpendiculaire est repatie en niveaux d'énergie discrets $\epsilon_N = \hbar.\omega_c\,(N + 1/2)$ appelés "niveaux de Landau", où N est un entier correspondant à l'indice des niveaux de Landau.

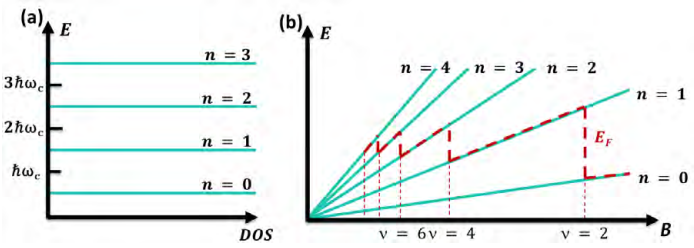

Figure 6.7: (a) Densité d'états pour un gaz d'électrons libres et indépendants en presence d'un champ magnétique. (b) Energie des niveaux de Landau en fonction du champ magnétique. La pente dépend du nombre quantique N (noté n dans la figure).

Les impuretés et les défauts sont toujours présents dans un matériau et agissent comme une source de diffusion pour les porteurs chargés. En conséquence, la durée de vie d'un état quantique est limitée et est notée τ_q. Son interprétation physique est similaire au temps de diffusion moyen de Drude, bien que ce dernier inclue une dépendance de l'angle de diffusion afin de donner plus de poids aux événements de rétrodiffusion. Lorsque le désordre est introduit, la densité d'états est élargie autour des niveaux d'énergie discrets de Landau (voir figure 6.8).

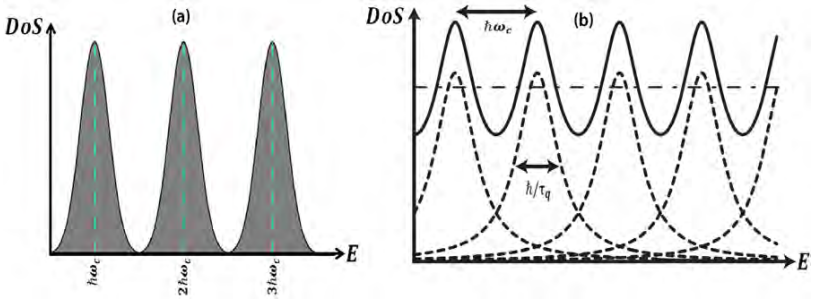

Figure 6.8: (a) Les niveaux de Landau sont élargis à cause du désordre. (b) La somme des niveaux de Landau élargis définit la densité des états totale. La modulation de la densité d'états induite par le champ magnétique peut être détectée expérimentalement si les niveaux de Landau individuels sont suffisamment séparés. Adapté de [65, 70]

Oscillations de Shunikov-de Haas

Pour un champ magnétique faible et en présence de désordre, la densité d'états d'un gaz d'électrons bidimensionnel ondule faiblement au-dessus d'un fond constant. Cette faible modulation de la densité d'états est à l'origine de faibles oscillations de la magnéto-résistance en fonction du champ magnétique, appelées "oscillations de Shubnikov-de Haas". La magetno-resistance est alors donnée par la formule de Lifshitz-Kosevich:

$$\rho_{xx} = \frac{m^*}{n.q^2.\tau_0}\left[1 + 2\exp\left(\frac{-\pi}{\omega_c.\tau_q}\right) \times \frac{\frac{2.\pi^2.k_BT}{\hbar\omega_c}}{\sinh\left(\frac{2\pi^2.k_BT}{\hbar\omega_c}\right)} \times \cos\left(\frac{2\pi.h.n}{2qB}\right)\right] \tag{6.11}$$

La résistivité longitudinale est composée de deux termes. Le premier est constant et correspond à l'expression de la résistivité établie avec le modèle de Drude. Le deuxième terme est une fonction oscillante dont la période est proportionelle à l'inverse du champ magnétique. La résistivité est minimum lorsque l'énergie de Fermi est située entre deux niveaux de Landau. Le terme exponentiel impliquant τ_q est le facteur de Dingle qui est responsable de l'augmentation de l'amplitude des oscillations de la résistivité lorsque le champ magnétique augmente. Le terme $X/\sinh(X)$ (où $X = \frac{2\pi^2.k_BT}{\hbar\omega_c}$) correspond aux effets de la temperaure qui tend à réduire l'amplitude des oscillations. La formule de Lifschitz-Kosevich n'est valable que pour les petits champs magnétiques, où la crête de la densité des états affiche une série de maxima et minima correspondant à l'apparition de niveaux de Landau. Les oscillations de Shubnikov-de Haas constituent une empreinte digitale du matériau étudié : l'étude de la période des oscillations en 1/B fournit un accès direct à la densité des porteurs de charges à condition que leur durée de vie soit suffisamment grande. Au contraire, la densité de porteurs extraite de l'effet Hall est sensible à tous les porteurs de charge quelle que soit leur mobilité. C'est la raison pour laquelle, dans certains systèmes multi-bandes complexes, la densité de porteurs extraite de l'effet Hall est plus grande que son homologue extraite de l'étude des oscillations de Shubnikov-de Haas. Au-delà de la densité de porteurs, la durée de vie quantique τ_q et la masse effective m^* sont des grandeurs essentielles accessibles experimentalement gràce à la formule de Lifschitz-Kosevich.

6.4 Fabrication des dispositifs et caractérisation électrique

6.4.1 Dichalcogénures de métaux de transition : de 3D à 2D

L'approche "top-down" consiste à amincir un matériau massif jusqu'à quelques couches atomiques voire une monocouche. Pour les matériaux exfoliables tels que WSe_2, cette technique réalisée "à la main" est bon marché et facile à mettre en oeuvre mais nécessite une longue expérience et un savoir-faire particulier. Elle produit des systèmes 2D de haute qualité avec des dimensions de quelques dizaines de micromètres carrés. L'objectif est de fabriquer une structure avec une monocouche WSe_2 déposée sur un flocon de nitrure de bore hexagonal (h-BN). Ce système doit ensuite être connecté à plusieurs électrodes métalliques pour les mesures de transport électrique. Les étapes principales de fabrication d'un échantillon sont décrites ci-dessous.

Nettoyage du substrat Si/SiO_2: Nous utilisons des substrats carrés de Si/SiO_2 dopés p avec une taille latérale de 1 cm, ayant un repère alpha-numérique réalisée par lithographie optique. L'épaisseur de l'oxyde de silicium est de 300 nm. Des méthodes sophistiquées sont utilisées pour éliminer les résidus, en commençant par les plus douces jusqu'aux plus agressives, afin de préserver au maximum la couche d'oxyde. Par exemple, l'acétone chaude et/ou la sonication se sont avérées très utiles. En dernier recours, nous utilisons une méthode de nettoyage avec un plasma d'oxygène de faible puissance et un temps d'exposition très limité (1 s à une puissance de radiofréquence de 10 W).

Préparation du substrat: L'objectif est de déposer des flocons de h-BN ayant une épaisseur de quelques couches au hasard sur un substrat standard Si/SiO_2. Pour cela nous découpons une pièce de PDMS (Silicone) que nous déposons sur une lame de verre. Ensuite, nous exfolions plusieurs fois le cristal de h-BN, avec un ruban adhésif. Le ruban adhésif est doucement pressé contre le PDMS et décollé en douceur. Certains flocons de h-BN sont transférés au hasard depuis le ruban adhésif à la surface du PDMS. Enfin, nous mettons le PDMS en contact avec le substrat Si/SiO_2. L'utilisation du PDMS comme étape intermédiaire permet un transfert propre de quelques flocons de h-BN avec des épaisseurs et des tailles différentes, bien isolés les uns des autres, sur le substrat Si/SiO_2. En se référant au contraste obtenu à l'aide d'un microscope optique, nous recherchons les paillettes de h-BN les plus importantes transférées sur le substrat en termes de taille latérale, planéité, épaisseur (maximum 30 nm) et espace libre environnant. Si nécessaire, des mesures AFM sont effectuées pour déterminer précisément l'épaisseur.

Exfoliation de WSe_2 et dépôt sur flocon de h-BN: Les cristaux de WSe_2 massifs sont traités de la même manière que détaillée précédemment. Nous déposons ensuite ce flocon exactement au-dessus du flocon h-BN à l'aide d'un ensemble d'étages mobiles de précision. Cette méthode appelée "technique de transfert à sec" est illustrée dans la figure 6.9. Le système WSe_2/PDMS est aligné avec le substrat h-BN/SiO_2/Si sous l'objectif d'un microscope. La transparence optique du PDMS et de la lame de verre permet la visualisation des flocons WSe_2 et h-BN en ajustant la mise au point du microscope. Une fois que l'alignement souhaité est atteint, les deux flocons sont pressés l'un contre l'autre.

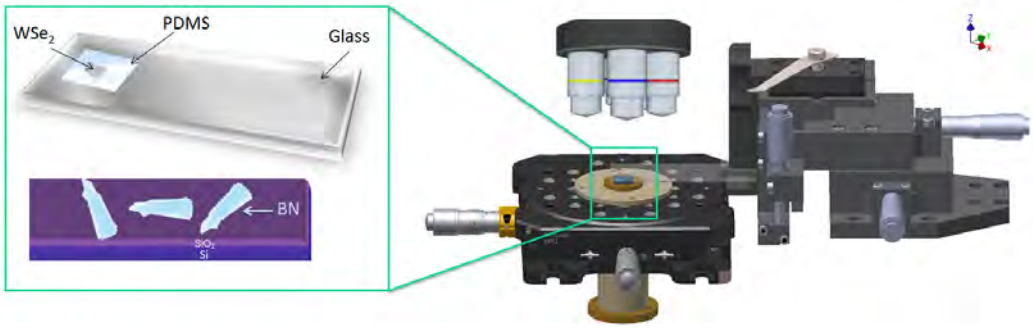

Figure 6.9: Dispositif de micro-alignement des flocons de DCMTs et de h-BN

6.4.2 Fabrication et adressage électrique des échantillons

Lithographie électronique: Cette technique développée dans les années 60, utilise un faisceau d'électrons focalisé sur les zones choisies d'un substrat préalablement recouvert d'une résine électro-sensible. Le substrat est ensuite plongé dans une solution de dissolution, les zones exposées sont éliminées beaucoup plus rapidement que la résine non exposée. Dans ce travail on distingue les micro-électrodes, qui relient directement le flocon de WSe_2 avec une grande précision, des macro-électrodes qui s'étalent sur quelques mm^2 et sont utilisées à des fins d'interconnexion électrique. Nous utilisons les logiciels AutoCAD et kLayout pour concevoir les électrodes (voir figure 6.10). Les marques d'alignement sont dessinées sur les coins de chaque zone de travail pour un réglage précis du faisceau d'électrons.
Metalisation et "lift-off": Une fois que la résine a été développée, l'échantillon est prêt pour la métallisation. Nous déposons un bicouche métallique en platine (Pt) et or (Au) pour les micro-électrodes, tandis que le titane (Ti) et l'or sont utilisés pour les macro-électrodes.

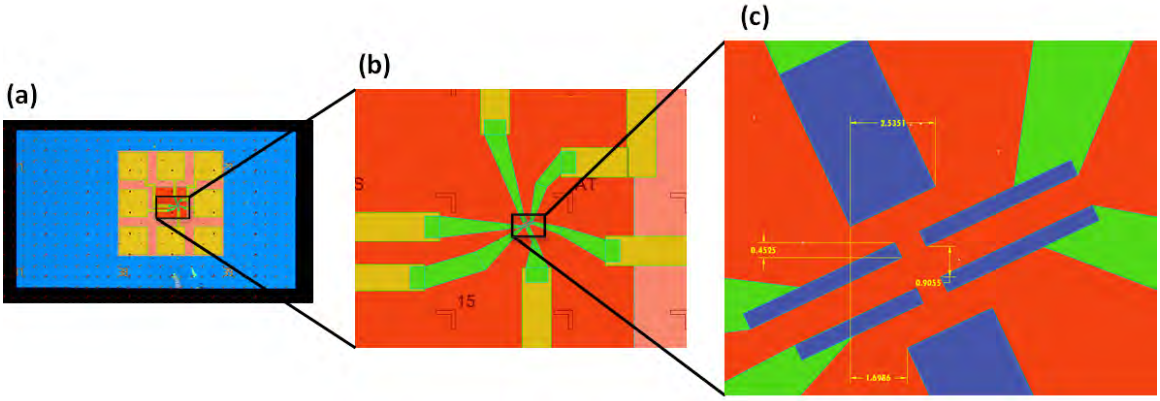

Figure 6.10: a) et b) Dessin des macro-electrodes et des micro-éléctrodes. c) Géométrie barre de Hall typique utilisée

Gravure plasma: Nous avons utilisé la technique de gravure au plasma pour certains échantillons afin d'obtenir une géométrie en barre de Hall bien définie. L'échantillon est d'abord recouvert de résine à l'exception des parties à graver qui sont retirées par lithographie par faisceau d'électrons.

Soudure par thermo-compression: Pour connecter les macro-électrodes de l'échantillon à un contact électrique de plus grande dimension, nous utilisons une machine de micro-soudure. Un fil d'or d'un diamètre 17 μm est plaqué contre l'électrode de l'échantillon tandis qu'une impulsion d'ultra-sons fait fondre le métal localement et assure un bon contact électrique. Le processus est répété sur le plot de connexion, puis coupé.

6.4.3 Caractérisation structurale et mesure de l'épaisseur des flocons h-BN/WSe_2

Les propriétés physiques des DCMTs sont intimement liées au nombre et à la parité du nombre des couches. Le nombre de couches peut être déterminé en utilisant plusieurs méthodes telles que la microscopie optique, la microscopie à force atomique, la photoluminescence, la spectroscopie Raman et la microscopie électronique en transmission. La microscopie optique constitue le moyen le plus simple d'estimer le nombre de couches, pour des échantillons constitués au maximum de 3 couches. Il s'agit d'une méthode non destructive, basée sur le contraste optique, largement utilisée pour les matériaux DCMTs. La microscopie à force atomique a été utilisée pour déterminer l'épaisseur des échantillons réalisés dans ce travail, le mode d'imagerie utilisé est le mode "tapping". La figure 6.11 montre des micrographies AFM pour différents flocons exfoliés de WSe_2 avec différentes épaisseurs. L'intensité de photoluminescence (PL)

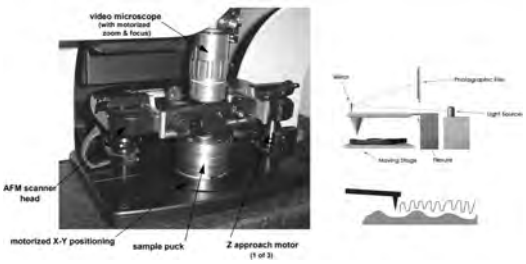

Figure 6.11: Microscope à force atomique (AFM) utilisé pour la détermination de l'épaisseur des flocons. Illustration du mode tapping.

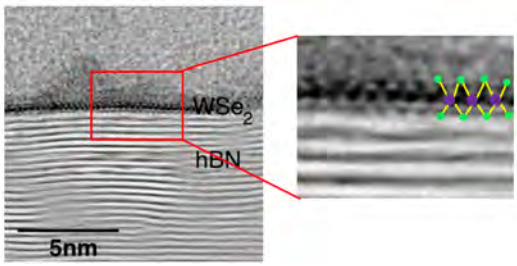

Figure 6.12: Cliché de microscopie électronique en transmission dans lequel le flocon de h-BN apparait comme des franges sombres et claires tandis que le flocon de WSe_2 apparait comme une alternance de points sombres et clairs.

est très faible pour les matériaux à bande interdite indirecte car elle repose sur un processus assisté par phonons à faible rendement quantique. D'autre part, la réponse en PL est élevée pour les DCMTs monocouches, signature d'un semi-conducteur à bande interdite directe [82]. Un pic d'émission PL à 1.63 eV a été rapporté dans les références [44, 7] en accord avec les mesures PL réalisées sur nos échantillons de WSe_2 monocouches. Par ailleurs, la détermination de l'épaisseur peut être effectuée par une observation directe de l'échantillon à l'aide d'une microscopie électronique à transmission. La microscopie électronique en transmission à balayage en champ clair est rapportée sur la figure 6.12.

6.4.4 Caractérisations électriques

Les propriétés de transport de base telles que la densité de porteurs et la mobilité électronique peuvent être obtenues en mesurant le courant en fonction de la tension de grille ou de la tension drain-source (polarisation) [91]. Il convient de mentionner que lorsqu'un contact électrique est réalisé entre un métal et un semi-conducteur, une barrière Schottky est établie. Près de l'interface, un transfert de charges se produit jusqu'à ce que l'énergie de Fermi soit la même dans les deux matériaux. Les flocons de WSe_2 n'étant pas dopés, l'énergie de Fermi se situe dans la bande interdite, le système est un isolant. Lorsqu'une tension négative est appliquée à l'électrode de grille, le potentiel électrochimique des porteurs de charge dans WSe_2 est modifié, ce qui entraîne une diminution de la barrière Schottky lorsque l'énergie de Fermi s'approche du maximum de la bande de valence. Pour une tension de grille négative et suffisamment élevée, l'énergie de Fermi est proche du bord de la bande de valence, cette situation résulte en un courant net mesurable. Le courant augmente rapidement à mesure que

la tension drain-source devient suffisamment élevée, comme le montre la figure 6.13. Lorsque la tension de grille est faible (par exemple de 0 à -45 V), le courant est nul pour la plage de tension de polarisation explorée à T=4.2 K. Pour $V_g < -60$ V, un courant faible apparaît qui ne peut être mesuré que lorsque la tension de polarisation est suffisamment grande, ce qui donne une courbe I(V) fortement non linéaire. La non-linéarité a tendance à disparaître lorsque la tension de grille s'approche de $V_{BG} = -90$ V et finit par disparaître lorsque l'énergie de Fermi est à l'intérieur de la bande de valence. La figure 6.13-b est une représentation alternative de cet effet, où le courant I_D est affiché en fonction à la fois de la tension de polarisation et de la tension de grille arrière dans un diagramme en couleurs. D'autre part, lorsqu'une tension positive est appliquée à l'électrode de grille, les électrons devraient être capables de transporter le courant lorsque l'énergie de Fermi est proche du bord de la bande de conduction. Néanmoins, la tension de grille arrière minimale requise pour réaliser la conduction électronique est hors de portée expérimentale (¿110 V).

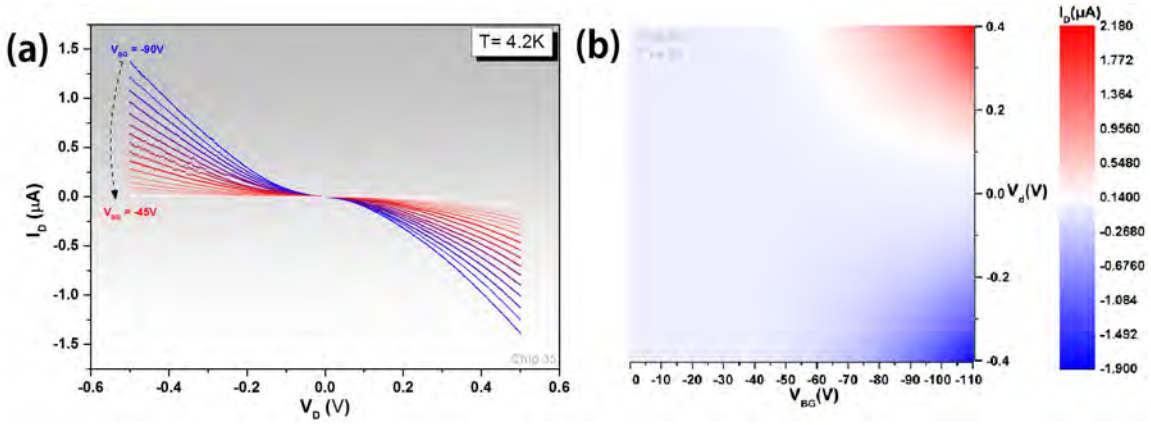

Figure 6.13: a) Courant drain-source pour différentes valeures de la tension de grille de -45 V à -90 V par pas de -2.5 V dans un flocon multi-couches de WSe_2. b) Représentation du courant drain-source avec une carte de couleur en fonction de V_{BG} et V_{ds} pour un flocon monocouche de WSe_2

.

6.4.5 Génération de champ magnétique pulsé

Le travail expérimental réalisé au cours de cette thèse a été réalisé avec des impulsions de champ magnétique d'une durée $\sim$ 300 ms et d'un champ maximum de 55 T, qui pouvaient être répétées toutes les heures environ. Les champs magnétiques pulsés sont produits par la décharge d'une grande batterie de condensateurs dans une bobine résistive refroidie à la température de l'azote liquide (77K). Une diode

”crowbar” est insérée dans le circuit RLC afin d’éviter toute oscillation du courant, de la tension ou du champ. La batterie de condensateurs est capable de stocker une énergie électrostatique de 14 MJ lorsqu’elle est chargée sous une tension maximale de 24 kV. Lorsque la charge est terminée, des thyristors à déclenchement optique laissent le courant circuler vers la bobine génératrice de champ magnétique. Le courant circulant dans le circuit de la bobine, qui est proportionnel au champ magnétique produit, augmentera de manière sinusoïdale jusqu’à atteindre sa valeur maximale, à ce moment la tension au niveau de la batterie de condensateurs change de signe et la diode « crowbar » devient conductrice. L’énergie magnétique stockée dans la bobine se dissipera par effet Joule dans une résistance en série avec le circuit contenant la diode. Le courant, et donc le champ magnétique, diminuera selon une loi exponentielle. La bobine représentée dans l’encart de la figure 6.14 est réalisée en enroulant un fil de cuivre renforcé de zylon noyé dans de la résine époxy.

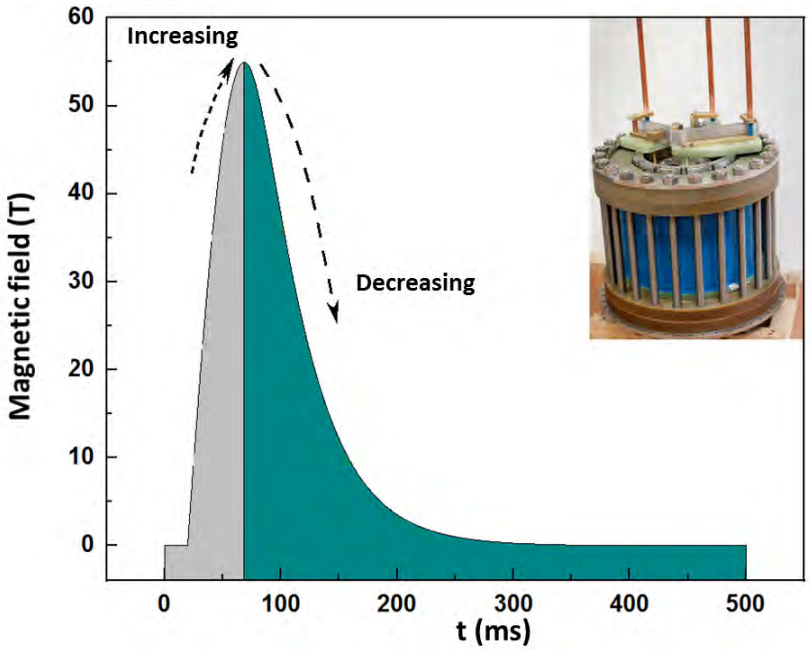

Figure 6.14: Profile du champ magnétique pulsé, atteignant 60 T au maximum. Encart: photographie d’une bobine permettant la génération de champs magnétiques.

6.5 Oscillations quantiques dans une monocouche de WSe_2 dopée P

De nombreux échantillons ont été fabriqués mais seuls quelques-uns d'entre eux ont fourni des résultats de magnéto-transport exploitables. La plupart du temps, la résistance des échantillons était trop grande pour permettre un rapport signal sur bruit signal suffisant pour réaliser des mesures sous champ magnétique intense, sans parler des échecs du processus de fabrication. De plus, les échantillons de monocouches de WSe_2 sont fragiles et une campagne de mesure (d'une à deux semaines en moyenne) dans les conditions extrêmes de basses températures et de champs magnétiques élevés est délicate. Ci-après, nous nous concentrerons sur un échantillon WSe_2 monocouche particulier qui a présenté les meilleures caractéristiques.

6.5.1 Caractérisation des échantillons et magnéto-transport

Fabrication: La figure 6.15 montre l'image au microscope optique de l'échantillon après tout le processus de fabrication. Un flocon de WSe_2 monocouche est déposé sur un flocon de h-BN plus grand, et l'ensemble repose sur un substrat Si/SiO_2. Bien que l'échantillon ne puisse pas être gravé en barre de Hall, la connexion électrique est faite avec deux grands contacts pour l'injection de courant et quatre électrodes situées des deux côtés de l'échantillon.

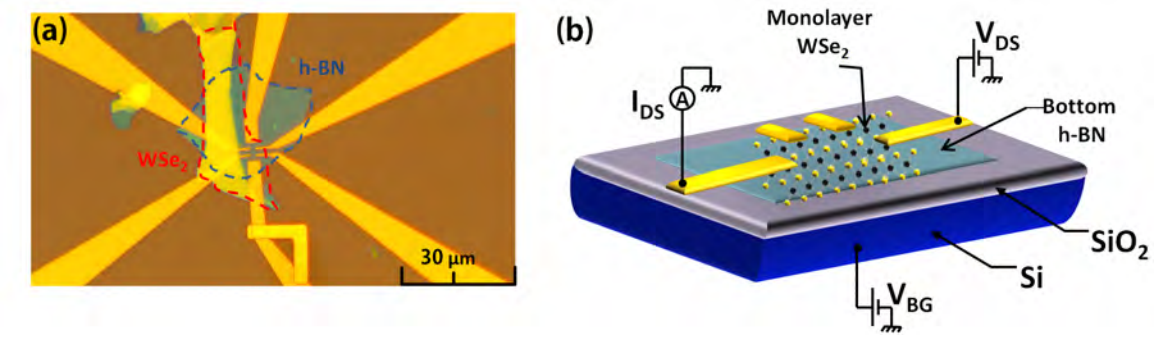

Figure 6.15: a) Image au microscope optique de l'échantillon : une mono-couche de WSe_2 difficilement visible attachée à un flocon épais. Le flocon de WSe_2 et le flocon de BN sur lequel il repose sont entourées de lignes rouges et bleues, respectivement. b) Schéma de connexion électrique des électrodes de mesure de l'échantillon. La densité de porteurs peut être modifiées par effet de champ à l'aide de la tension de grille V_{BG} appliquée sur le substrat de silicium.

Caractérisation: Des techniques de caractérisation structurale et optique ont été mises en oeuvre pour certifier la nature monocouche du flocon de WSe_2 dans cet échantillon. La mesure AFM réalisée sur le bord du flocon de WSe_2 donne une hauteur de marche égale à 0.7 nm, en accord avec l'épaisseur typique d'une monocouche. Une autre confirmation est venue de l'analyse par microscopie électronique à transmission en champ clair réalisée sur l'échantillon après la campagne de mesure. Enfin, une réponse en photoluminescence qui montre un pic d'émission à 1.63 eV est la signature d'une monocouche de WSe2. Après avoir préparé l'échantillon et l'avoir installé dans un insert dédié pour les mesures en champ magnétique pulsé, nous l'avons refroidi à 4 K et mesuré le courant drain-source I_{DS} en fonction de la tension de grille V_{BG}. L'échantillon passe à l'état conducteur uniquement pour les tensions de grille inférieures à une tension de seuil V_{thrBG}, ce qui traduit une conduction par les trous. Le régime de conduction électronique a été recherché pour une tension de grille positive jusqu'à +110 V, mais n'a pas pu être observé pour cet échantillon.

Mesures sous fort champ magnétique: Nous avons effectué des mesures de magnéto-transport sous champ magnétique pulsé jusqu'à 55 T à basse température (4.2 K) pour différentes valeurs de la tension de grille. La magnétorésistance présente des oscillations de grande amplitude superposées à un fond lentement variable lorsque la tension de grille est réglée près de la limite expérimentale maximale (-110 V), c'est-à-dire pour des concentrations de trous élevées. En revanche, pour une tension de grille proche du seuil de conduction, l'injection de courant est perturbée par de grandes barrières de Schottky. L'analyse des oscillations quantiques nécessite leur extraction via la suppression du fond de magnéto-résistance, qui est liée à la variation lente du temps de diffusion moyen induite par le champ magnétique en plus de l'effet de quantification de la densité d'états (formation des niveaux de Landau). Les données, après traitement numérique, sont présentées sur la figure 6.16. Pour toutes les tensions de grille, les oscillations de la magnéto-résistance sont complexes et nous faisons l'hypothèse que l'énergie Zeeman est suffisamment grande pour entrer en compétition avec l'énergie cyclotron, ce qui peut expliquer des oscillations supplémentaires ou déformées par rapport au résultat attendu issu de l'équation de Lifshitz-Kosevich.

Masse effective: La dépendance en température des oscillations quantiques a été étudiée pour déterminer la masse effective des trous. Comme prévu, l'amplitude entre deux extremums successifs diminue avec l'augmentation de la température. La valeur extraite de la masse effective $m^* = (0.45 \pm 0,04) \times m_e$ est en accord avec la littérature [13].

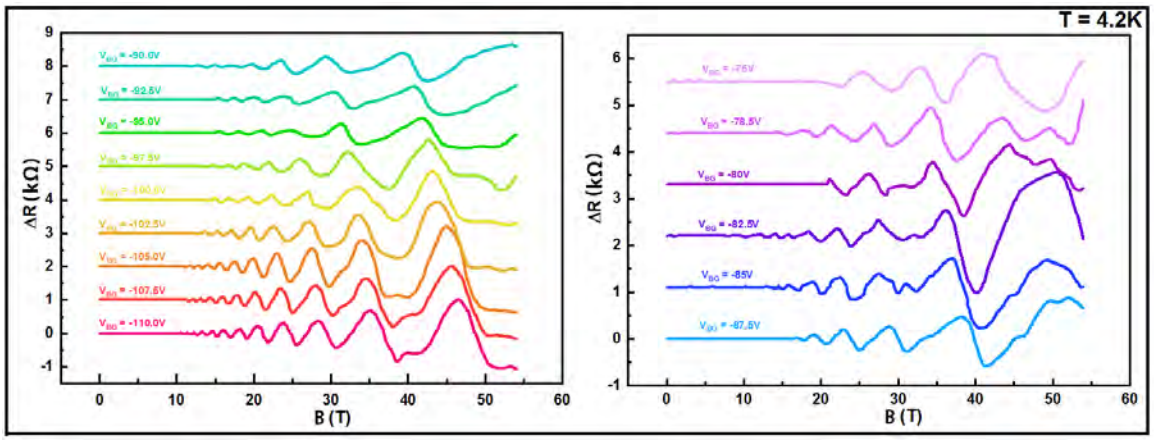

Figure 6.16: Magnéto-résistance à fort champ magnétique d'une mono-couche de WSe_2 à $T = 4.2\,\mathrm{K}$, pour plusieurs tensions de grille. Les courbes sont décalées verticalement et réparties sur deux graphiques pour davantage de lisibilité.

6.5.2 Simulation du magnéto-transport

La formule de Lifschitz-Kosevich, en prenant en compte les contributions de spin, peut reproduire en partie les courbes de résistivité longitudinale, mais n'est pas adaptée à l'analyse des données expérimentales dans leur ensemble. Par conséquent, nous avons décidé, pour étudier les oscillations quantiques au-delà du régime d'oscillation SdH, de développer un modèle pour simuler la composante oscillatoire de la magnétorésistance, à la fois à champ magnétique faible et élevé. Dans un premier temps, nous supposons que les monocouches WSe_2 hébergent des quasi-particules nommées fermions de Dirac massifs (MDF).

Détermination auto-cohérente du potentiel électrochimique : Nous supposons que l'énergie des états quantiques du niveau de Landau d'indice N suit une distribution gaussienne autour de l'énergie $\epsilon_{N,s}$. La densité d'états est donc simulée à l'aide de l'équation 6.12:

$$\rho(\epsilon, B) = \sum_{N=0,s=\pm 1/2}^{N=N_c} \frac{q.B}{h} \times \frac{1}{\sqrt{2\pi}\Gamma(B)} \times \exp\left[-\frac{1}{2}\left(\frac{\epsilon - \epsilon_{N,s}}{\Gamma(B)}\right)^2\right] \tag{6.12}$$

Nous avons introduit la fonction d'élargissement des niveaux de Landau $\Gamma(B)$, qui dépend du champ, et qui est liée à la mobilité (quantique) des trous μ_h, un paramètre d'ajustement, via la relation $\Gamma(B) = \frac{\hbar.q}{m^*}\sqrt{\frac{2B}{\pi.\mu^h}}$. Nous avons supposé que tous les niveaux de Landau ont le même élargissement. Le potentiel électrochimique est noté μ dans la suite. La densité de trous n_h est calculée en comptant les niveaux occupés

jusqu'au potentiel chimique:

$$n^{2D} = \int_0^{\mu_{(B)}} \rho(\epsilon, B).f\left(\epsilon - \mu_{(B)}\right).d\epsilon \tag{6.13}$$

où $f(\epsilon - \mu)$ est la fonction de distribution de Fermi-Dirac. Une routine Python calcule le potentiel électrochimique $\mu(B)$ de sorte que n_h est une constante.

Composants du tenseur de conductivité: La conductivité longitudinale des systèmes 2D homogènes est abordée à l'aide de l'équation 6.14, dérivée de la théorie des perturbations d'ordre élevé de la diffusion sur des impuretés électroniques étendues [24]

$$\sigma_{xx}(B) = \frac{q^2}{h} \sum_{N,s} \left(N + \frac{1}{2}\right) \int_{-\infty}^{\infty} \left[-\frac{df(\epsilon - \mu_{(B)})}{d\epsilon}\right] \times \exp\left[-\frac{1}{2}\left(\frac{\epsilon - \epsilon_{N,s}}{\Gamma}\right)^2\right].d\epsilon \tag{6.14}$$

Cette expression reproduit bien les oscillations de Shubnikov-de Haas à faible champ magnétique, mais ne parvient pas à décrire le régime de champ magnétique élevé. La relation entre la densité d'états et le taux de diffusion est difficile à simuler dans ce régime et, à la place, nous le traitons phénoménologiquement avec une fonction de coupure de largeur $\delta\epsilon(B)$ appliquée sur la queue des niveaux de Landau. La résistivité est finalement simulée en utilisant les équations 6.15:

$$\rho_{xx} = \sigma_{xx} \times \rho_{xy}^2 + \sigma_{xx}^3 \times \rho_{xy}^4 + ... \tag{6.15}$$

où

$$\rho_{xy}(B) = \frac{h}{q^2} \sum_{N,s} \left[\int_{-\infty}^{+\infty} f(\epsilon - \mu_{(B)}) \times \frac{d\epsilon}{\sqrt{2\pi}\Gamma} \exp\left(-\frac{\left(\epsilon - \epsilon_{N,s}\right)^2}{2\Gamma^2}\right)\right]^{-1}$$

est la magnéto-résistance transversale (de Hall).

Simulations, algorithme et procédure d'ajustement: Pour chaque valeur de la tension de grille (c'est-à-dire pour différentes densités de trous n_h), le logiciel importe les données expérimentales $R_{exp}^{xx}(B)$ et minimise la différence entre la résistance longitudinale expérimentale et simulée. En raison du grand nombre de paramètres, la difficulté à réaliser un ajustement sur l'ensemble de la plage de champ magnétique est telle que nous avons décidé de sélectionner manuellement la meilleure courbe d'ajustement. Les paramètres d'ajustement n_h et E_z/E_c sont les plus significatifs

et nécessitent une attention particulière. Le premier influe principalement sur le régime de champ magnétique faible, où l'élargissement des niveaux de Landau est plus grand que l'énergie cyclotron ou Zeeman. Dans ce régime, les oscillations quantiques apparaissent à peu près quasi périodiques en 1/B et la période est presque uniquement déterminée par la densité des porteurs. En revanche, le rapport E_z/E_c est particulièrement influent dans le régime de champ magnétique élevé. Selon sa valeur, on observe la présence de pics, vallées ou inflexions supplémentaires. Contrairement à la densité de porteurs, il n'existe pas une unique valeur de E_z/E_c qui permet d'ajuster correctement la simulation aux données, la figure 6.17 présente les courbes expérimentales avec leurs simulations correspndantes.

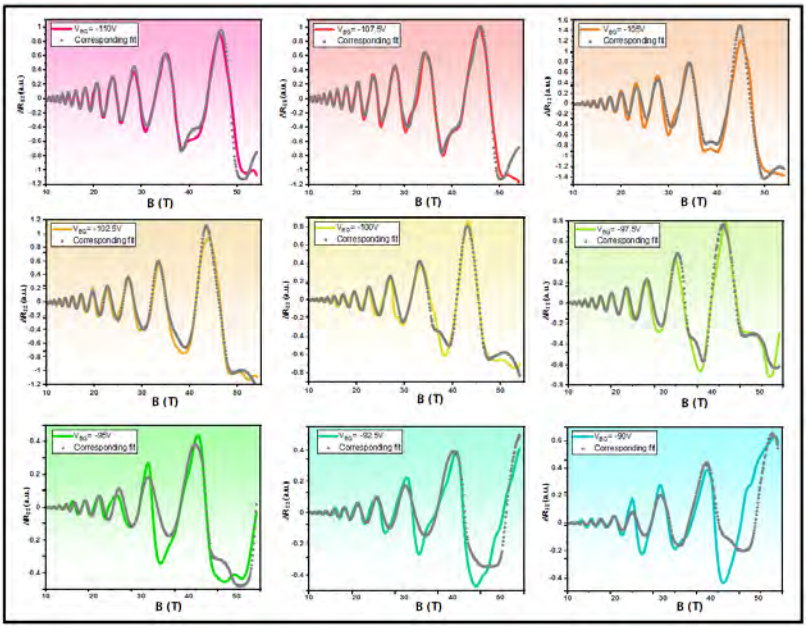

Figure 6.17: Magnéto-résistance expérimentale superposée aux courbes simulées pour certaines tensions de grille.

6.5.3 Détermination expérimentale du facteur de Landé

Multiplicité du rapport Ez / Ec: Pour un champ magnétique assez faible et/ou à concentration de porteurs de charge suffisamment élevée, le spectre de niveau de Landau est exactement le même pour une valeur particulière de $E_z/E_c \pm N_0$, où N_0 est un entier pair. Pour un champ magnétique donné, la gamme d'énergie où les niveaux de Landau des deux spin sont présents constitue le régime mixte alors que le régime polarisé est établi lorsque Landau les niveaux ont le même indice de spin. Sonder le régime polarisé permet d'établir la valeur exacte de E_z/E_c, mais ce régime est

expérimentalement difficile à atteindre. Dans ce travail et pour la plage de densités de trous disponibles, aucune indication du régime polarisé n'a pu être observée, malgré des champs magnétiques aussi élevés que 55 T. En revanche, la parité de la partie entière du rapport E_z/E_c ne souffre aucun doute. En effet, un changement de ± 1 de ce paramètre conduit à un déphasage de 1/B-périodique oscillations quantiques pour champ magnétique faible.

Évolution de la densité de porteuse du facteur g: En revenant sur l'hypothèse concernant la nature des porteurs de charge et en utilisant le spectre d'énergie des niveaux de Landau des Fermions de Schrödinger, les simulations sont adéquates pour un jeu de paramètres identiques sauf en ce qui concerne le rapport E_z/E_c. La différence entre les deux types de porteurs de charge réside dans la dégénérescence du niveau Landau $N = 0$. Ainsi, si le rapport E_z/E_c permet un bon ajustement théorique dans le modèle des Fermions de Dirac Massifs, le rapport $E_z/E_c + 1$ sera tout aussi adéquat avec le modèle des fermions de Schrödinger. En conséquence, il est impossible de distinguer la nature des porteurs de charge. La figure 6.18 montre le rapport E_z/E_c extrait de l'ajustement dans la plage de densité de trous explorée pour les deux modèles considérés. Nous notons que E_z/E_c augmente à mesure que la densité de porteurs diminue. Cette tendance est en accord avec la littérature dédiée aux monocouches de WSe_2 [13, 12]. Le facteur Landé effectif, sensible aux interactions électron-électron, est lié au rapport E_z/E_c par la relation $g^* = \frac{2m_e}{m^*} \times \frac{E_z}{E_c}$. Lorsque la densité de trous diminue, l'énergie associée aux interactions électroniques devient prépondérante devant l'énergie cinétique dans les gas bidimensionnels. Les interactions électroniques incluent l'interaction d'échange, qui est minimisée lorsqu'elle implique deux particules de même spin dans l'approximation de Hartree-Fock. Par conséquent, un système composé de particules avec le même état de spin est favorisé dès lors que les interactions électroniques se renforcent au détriment de l'énergie cinétique. La susceptibilité magnétique de spin est proportionnelle au facteur de Landé effectif et rend compte de l'état de polarisation de spin des systèmes. Ainsi, l'augmentation du facteur de Landé effectif indique une polarisation de spin croissante dans le système, provoqué par le renforcement des interactions électroniques à mesure que la densité de trous diminue.

Remarques finales Malgré d'éventuelles erreurs dans le traitement des données expérimentales et le manque de justification physique pour certaines hypothèses du modèle, la qualité de l'ajustement de magnétorésistivité est remarquable pour les courbes de densité de trous les plus élevées, sans invoquer une dépendance de champ du rapport E_z/E_c. L'un des ingrédients clés de ce succès est le calcul auto-cohérent du potentiel chimique, qui va au-delà de la formule de Lifschitz-Kosevich. En effet, des simulations réalisées avec un potentiel électrochimique indépendent du champ magnétique reproduit bien la partie bas champ des données expérimentales, mais ne

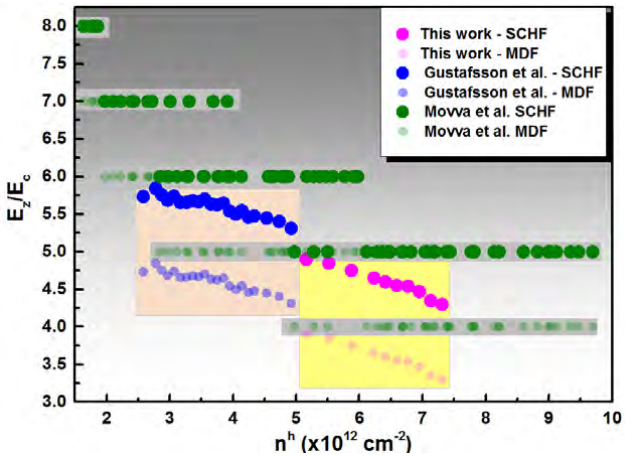

Figure 6.18: Valeurs de Ez/Ec extraites de la simulation en fonction de la densité de trous. Les points roses correspondent au modèle impliquant des fermions de Schrödinger (SCHF). En diminuant ces valeurs de 1 (points roses clair), nous obtenons les valeurs du rapport E_z/E_c avec le modèle impliquant des fermions de Dirac massifs (MDF). Ces grandeurs sont comparées à celles de la littérature (points bleus et verts), où le modèle MDF (couleurs claires) ou SCHF (couleurs vives) sont reportés.

parviennent pas à aborder correctement le régime de champ élevé. La simulation est utile pour analyser les oscillations quantiques d'un échantillon avec Résolution de niveau Landau, par exemple à mobilité modérée. Cependant, il serait intéressant de reproduire cette étude avec un échantillon de meilleure qualité. Une voie pour y parvenir est de fabriquer une mono-couche WSe_2 entièrement encapsulée avec du h-BN [16, 13, 12], même si les contacts ohmiques sont difficiles à réaliser dans cette configuration.

6.6 Conclusion

Cette thèse est dédiée à l'étude des propriétés électroniques d'une mono-couche de diséléniure de tungstène (WSe_2) par magnéto-transport sous champ intense. Ce système a été choisi pour plusieurs raisons. Premièrement, il est le siège d'un gaz bidimensionnel de particules chargées puisque son épaisseur atteint la limite ultime d'un plan stochïométrique atomique. Les propriétés électroniques des systèmes bidimensionnels sont très différentes de leurs homologues massifs en raison de l'absence de symétrie de translation dans une direction. Une connaissance approfondie de leurs propriétés électroniques est essentielle pour leur intégration dans les futurs dispositifs optoélectroniques. Deuxièmement, la monocouche de WSe_2, qui appartient à la famille des dichalcogénures de métaux de transition, est susceptible d'héberger un nouveau type de quasi-particules appelées «fermions de Dirac massifs». Contrairement aux fermions de Dirac sans masse dans le graphène ou aux fermions de Schrödinger dans les systèmes semi-conducteurs 2D, les fermions de Dirac massifs sont caractérisés à la fois par la présence d'une bande d'énergie interdite dans le

spectre des excitations et d'un verrouillage des degrés de liberté de spin et de vallée. Troisièmement, la masse effective des porteurs de charge (en particulier des trous avec $m^* = 0.45 \times m_e$) et la faible constante diélectrique du milieu entourant la mono-couche (le vide et un flocon de nitrure de bore dans cette étude) implique un ratio important entre l'énergie Coulombienne et l'énergie cinétique. Ce système est donc une plate-forme très intéressante pour étudier les interactions entre les particles chargées. L'analyse des données expérimentales, basée sur des simulations impliquant l'énergie Zeeman a permis d'extraire le facteur de Landé effectif en fonction de la densité des porteurs de charge (trous dans cette étude). Ce facteur, sensible à la force des interactions d'échange, augmente lorsque la concentration de trous diminue en accord avec les données de la littérature.

List of Figures

1 Left: Artistic view of micro-mechanical exfoliation of a mono-atomic layer of graphene using an adhesive tape. Right: Range of two-dimensional materials properties for potential applications. x

1.1 (a) Periodic classification of elements, where groups 4-10 transition metal atoms and chalcogen atoms have been highlighted. b) Schematics of the layered atomic structure of the transition metal dichalcogenides. 2

1.2 (a) Side and top views of the two polymorphs of monolayer TMDCs. Left panel trigonal prismatic (2H); right panel octahedral (1T). Chalcogen and metal atoms are shown in orange and green/violet, respectively .(b) Schematics of the structural polytypes of TMDCs from left to right 1T (tetragonal symmetry, one layer per unit cell and, octahedral coordination of the metal), 2H (hexagonal symmetry with two layers per unit cell and trigonal prismatic coordination) and 3R (rhombohedral symmetry with three layers per unit cell and trigonal prismatic coordination of the metal atoms). The yellow-filled triangles highlight the spatial position of the chalcogen atoms. For the 1T and 2H polytypes, top views are additionally shown. Note that in these images the yellow triangles highlight spatial positions of the chalcogen atoms. Adapted from [28]. 3

1.3 Representation of symmetry elements for (a) monolayer and (b) bilayer TMDCs (both with trigonal prismatic configuration of the metal atom). The chalcogen and metal atoms are shown in orange and green respectively. σ_h is the mirror symmetry operation by the horizontal planes sketched in yellow for monolayer and violet for bilayer. The red dot in inset (b) is an inversion symmetry point. 4

1.4 a) Real and b) reciprocal space representation of a monolayer TMDC. 5

1.5 Schematic example of Kramers degeneracy in a crystal in the case **(a)** no spin-orbit interaction where each level is doubly degenerate, **(b)** both spin-orbit interaction and inversion symmetry are present leading to two-fold degenerate quantum states, **(c)** spin-orbit interaction and no inversion symmetry leading to non-degenerate quantum states. Adapted from [57]. 7

1.6 Schematic density of states of bulk layered TMDCs from different groups of the Periodic Table. Adapted from[33]. 7

1.7 Spin states under $\boldsymbol{\sigma}_h$ symmetry operation. 8

1.8 Out-of-plane spin splitting with opposite signs at the **K** and **K'** points of the 1st BZ in mono-layer WSe_2. Adapted from [9]. 9

1.9 (a),(b) orbitally resolved contributions of Se and W atoms in the band-structure of mono-layer WSe_2 (c) Qualitative contribution of atomic orbitals to the Bloch states at high symmetry points of the FBZ. See the main text for the nomenclature. Adapted from [15]. 9

1.10 SOC splitting at K_v and K_c in TMDCs mono-layers from first-principles calculations. Adapted from [40]. 10

1.11 (a)The experimental monolayer WSe_2 band structure the top of the valence band along the high symmetry lines [18], (b) Normalized PL spectra by the intensity of peak A of thin layers of WSe_2 for N= 1-4 and bulk, (c) Raman spectra of WSe_2 for N=1-4 and bulk [45]. . . . 11

1.12 The electronic properties of 2H-bilayer TMDCs resemble those of two monolayer TMDCs in-plane rotated of 180° to each other. In the reciprocal space, the band edges at K and K' points of a bilayer TMDCs 1st BZ is merely a superposition of the band edge of each monolayer, leading to spin-degenerate states as required for point inversion symmetry systems. 12

1.13 Band structure of mono-, bi-, tri- and quad-layer WSe_2 obtained from DFT calculations including SOC. The horizontal dotted lines in dictates the spin-split bands, which represents the inter-layer hopping strength. Adapted from [37] 13

1.14 (a) Illustration of optical and electronic band-gap. (b) Optical band gap values for group VI TMDCs. Adapted from [28] 13

1.15 (a),(b) calculated band structure of 3L- MoS_2, and 6L-WS_2 .(b) High symmetry point representation in the reciprocal space with the red and the blue color refer to the spin-down and the spin-up respectively. (d) Schematic diagrams for the Bloch bands. Adapted from [56]. 14

2.1 (a) Sketch of a material submitted to an external electric field. (b) Random motion of charge carriers in the absence of electric field : the net current is null. (c) Drift motion of the charge carriers in the presence of an external electric field. 16
2.2 Fermi distribution at different temperatures. Adapted from [61] . . . 19
2.3 The effect of a constant electric field $\mathbf{E} = E_x\hat{x}$ on the **k**-space distribution of quasi-free electrons. (a) The Fermi sphere at equilibrium is centred at zero and is displaced in the out-of-equilibrium stationary state by an amount $\delta k_x = q\tau E_x/\hbar$. (b) The out-of-equilibrium Fermi distribution $f_{(\epsilon(k))}$ only differs from the equilibrium distribution f_0 dashed in the vicinity of the Fermi energy. Adapted from [61] . . . 20
2.4 The Hall effect 24
2.5 a) Components of the conductivity tensor as a function of the magnetic field. At $\mu B = 1$, $\sigma_{xx} = \sigma_{xy}$. (b) Components of the resistivity tensor as a function of magnetic field. For $\mu B = 1$, $\rho_{xx} = \rho_{xy}$ 25
2.6 a) Equipotential (dashed) and electric field lines (solid) for a bar geometry. b) Full view of the equipotentials in a Hall bar configuration 26
2.7 Semi-classical model of a charged particle in a magnetic field. The wave-function is a quasi-plane wave defined by k spreading along a circular trajectory of length L. The wave-function cannot be multiply defined, thus imposing the condition kL = 2πN. 30
2.8 (a) The corresponding density of states DOS for a free 2DEG perpendicular to the magnetic field without disorder. (b) Energy levels for electrons under a magnetic field. The slope depends on the quantum number N. At a fixed electron density the Fermi energy (red dashes) oscillates as a function of the filling factor. 34
2.9 (a) The individual landau levels are broadened due to the presence of charged scatterers causing potential fluctuations in the sample. (b) The sum of broadened Landau levels defines the density of states. The modulation of the density of states induced by the magnetic field can be experimentally detected if the individual Landau levels are sufficiently separated. Adapted from [65, 70]. 35
2.10 (a) Magnetoconductivity oscillations as a function of the inverse of the magnetic field for Sb_2Te_2Se single crystal.(b) Landau levels index for the minima and the maxima of the magnetocondiuctivity. The linear extrapolation of the points crosses the point with the coordinates ($H^{-1} = 0, N = 0.5$) [71] 42

3.1 Optical microscopy photos for different exfoliated h-BN flakes, the thickness **t** is determined using AFM 47

3.2 Micro-alignment setup and precision movable stage under optical microscope 47
3.3 Different steps for stacking exfoliated h-BN and WSe_2 using the dry transfer technique 48
3.4 Basic fabrication process of FET based on TMDCs materials 48
3.5 The resist spinner system. The wafer is maintained onto a chuck with vacuum. The resist is dispensed at the center of the wafer just before spinning. 49
3.6 AutoCAD design for a) macro-electrodes and b) micro-electrodes. c) Hall bar dimension and typical distance between the micro electrodes 50
3.7 (a) Optical miscroscope image of micro-electrodes after left: MIBK development, right: metalization and lift-off. (b) Optical miscroscope image of macro-electrodes after left: MIBK development, right: metalization and lift-off. 51
3.8 (a) Schematic representation for a sputtering process, which encloses the target, the sample holder, the ionised argon gas and the thickness monitor. (b) Evaporation source including the evaporation source, a sample holder and a tungsten filament for Joule heating. 52
3.9 A plasma etching planar system. The plasma consists of oxygen ions accelerated toward the wafer and thus impinging the material to be etched. 52
3.10 (a) WSe_2/h-BN stack before etching. (b) A Hall bar etched device with the parameter shown in table 3.2. (c) Image of an AFM for Hall bar etched device. (d) Etched Hall bar device addressed using classical techniques of e-beam lithography and metal evaporation. 53
3.11 (a) h-BN/WSe_2 electrically contacted device. (b) Full encapsulation with h-BN. (c) Electron beam lithography pattern for the top gate electrode. (d) Top gate metalization. 54
3.12 (a) Left: photograph of dicing machine available at the clean room facility AIME. Right: Dicing of the wafer with an accurate blade. (b) Photograph of the wire bonding machine used during this work. . . . 54
3.13 Left:Optical image of MoS2 under white illumination. Right:thickness determination based on optical contrast and artificial intelligence. Adapted from [80] 55
3.14 Top: Exfoliated WSe_2 flakes with different thicknesses. Middle: thickness determination using AFM. Bottom: height profile obtained from AFM measurements. 56
3.15 AFM for thickness determination with an illustration of the tapping mode. 56

3.16 Room temperature PL spectrum for mono- and bi-layer WSe_2 exfoliated flakes on Si/SiO_2 substrate. The left inset represents the difference between optical and electrical bandgap. The right inset shows the calculated band structure of monolayer obtained from [88]. 57
3.17 Raman spectra of mono-, bi-layer and bulk WSe_2 measured using a 633 nm excitation wavelength. Prominent peaks emerge at $\sim$ 375 cm^{-1} and $\sim$ 395cm^{-1} corresponding to E^1_{2g} and A_{1g} modes. Inset: E^1_{2g}, A_{1g} modes frequency difference as a function of the number of layers. . . . 58
3.18 Bright Field Scanning Transmission Electron Microscopy (BF-STEM) on which the h-BN substrate appears as dark/bright fringes whereas the WSe_2 layer consists of dark spots surrounded by brighter ones. The inter-atomic distance between W and Se atoms correspond to the expected ones. The WSe_2 layer is continuous and reproduces the top surface of h-BN stack. 58
3.19 a) Illustration of band bending at the interface between a metal (Pt) and p-doped SC (WSe_2) and the formation of a Schottky barrier. b) Band diagrams representation for TMDCs FET at $V_D = 0$ for $V_{BG} >$, = and < 0 [92]. 60
3.20 a)Drain-source current for various values of the back-gate voltage from -45 V to -90 V by steps of -2.5 V in a multi-layer WSe_2 field effect transistor at T=4.2K.b)V_{xx} vs V_{BG} at various V_D at T = 4.2K in a monolayer WSe_2 FET 61
3.21 (a) Two-probe and four-probe conductance at room temperature as a function of the back-gate voltage, from which the corresponding field effect mobility is extracted. (b) Strong variation of the contact resistance as a function of the back-voltage 61
3.22 G_{2pt} **vs** (V_{BG} and V_{TG}) varying from 0 to -110V and from -10V to 10V respectively at T=4.2K. The inset represents the connected and top-gated chip 52. The edge of the bottom h-BN, the WSe_2 multi-layer and the top h-BN are limited with dashed lines. 62
3.23 (a) Hysteresis effect on a FET based WSe_2 multi-layer contacted with platinum electrodes at room temperature. (b) The hysteresis effect decreases as the temperature is lowered. 63
3.24 (a) Electrical characteristics of tri-layer WSe_2 before and after annealing at 400 ^{o}C. (b) and (c) Evolution of the device performance after annealing for the p-doped and n-doped regimes, respectively, (t corresponds to the time were I performed the electrical characterisation after removing the sample from the annealing chamber). 64
3.25 a) Schematic electric diagram to produce a pulsed magnetic field. b) New 14 MJ generator at LNCMI. 65

3.26 Pulsed magnetic field as a function of time, reaching 60T at maximum. 66

3.27 (a) a general view of The ^{4}He cryostat inserted inside the coil used for magnetic field generation, in a large nitrogen cryostat with the probe. (b) A detailed description of ^{4}He cryostat with a top and interior view. (c) Head of the rotative probe with a connected sample. 68

3.28 Data acquisition setup. 69

3.29 a) Raw signal: voltage vs magnetic field, b) The parasitic induced voltage has been removed from the sample's signal, c) Windows averaging is used to smooth the signal 70

4.1 a) Optical image of a barely visible monolayer WSe_2 sample attached to a thicker flake. The whole WSe_2 flake and the underlying BN flake are enclosed by red and blue dotted lines, respectively. b) Sketch of the sample with operating electrodes connecting the monolayer WSe_2. The carrier density can be tuned electrostatically using a back-gate voltage V_{BG}. 72

4.2 a) Left: AFM image of the sample. Right: the height profile from monolayer WSe_2 to the underlying BN flake. b) BF-STEM image on which the h-BN flake appears as dark/bright fringes whereas the WSe_2 monolayer consists of dark spots surrounded by brighter ones. c) Photoluminescence spectrum typical of WSe_2 monolayer. 73

4.3 Evolution of the drain-source current as a function of the back-gate voltage, for three different temperatures, evidencing a temperature-dependent back-gate voltage threshold for the "ON" state. The fluctuations of the lowest temperature curve reflects impurity levels in the gap or in the Schottky barriers. 74

4.4 Background removal procedure. a) Raw data. b) Manual identification of the oscillations' extrema, defining the envelope spline functions and the background. c) Background subtracted data. 74

4.5 High field magneto-resistance of monolayer WSe_2 at $T = 4.2\,\mathrm{K}$, for different back-gate voltages. The curves are offset and split into two graphs for clarity. 75

4.6 Determination of the effective mass, where the amplitude of the oscillations as a function of temperature is evaluated for different values of the magnetic field. Insert: temperature evolution of monolayer WSe_2 magneto-resistance at $V_{BG} = -105\,\mathrm{V}$, in the temperature range $1.4\,\mathrm{K}$ to $15\,\mathrm{K}$. 76

4.7 a) Band structure of monolayer WSe_2 at points K and K' of the first Brillouin zone. The dispersion relation can be approximated by a parabolic function for energies close to the top of the spin-split valence bands. b) Under perpendicular magnetic field, the energy is quantized into two-fold degenerate Landau levels, except the non-dispersive $N = 0$ Landau level. Adapted from [19] 78

4.8 Evolution of the chemical potential $\mu(B)$ at $T = 4.2\,\mathrm{K}$ for $\mu^h = 2000\,\mathrm{cm}^2/\mathrm{V.s}$ (blue curve) and $\mu^h = 6000\,\mathrm{cm}^2/\mathrm{V.s}$ (red curve) for a) a sin-degenerate Landau level structure (E_z/E_c is an integer) and b) a spin-resolved Landau level structure. The green dotted line is $\mu(B = 0)$. 80

4.9 a) Spin-resolved broadened Landau levels under high magnetic field. The red curve stands for spin up Landau levels whereas the blue curve represents the spin down. The violet line is the cumulative density of states according to equation 6.12. The filled areas represent the product of the cut-off function $\delta\epsilon(B)$ with the Gaussian broadened Landau levels. Unrealistic parameters have been chosen to prevent overlapping effects and to help understanding the figure: $n^h = 8 \times 10^{12}\,\mathrm{cm}^{-2}$, $B = 60\,\mathrm{T}$, $E_z/E_c = 1/2$, $\mu^h = 2000\,\mathrm{cm}^2/\mathrm{V.s}$, $B_0 = 35\,\mathrm{T}$, $\delta\epsilon(B = 60T) = 6.28\,\mathrm{meV}$. b) Example $\delta\epsilon(B)$ with parameters $A_1 = 1$, $A_2 = 0.2$, $B_0 = 30\,\mathrm{T}$ and $\delta B = 2\,\mathrm{T}$ used to define the cut-off function of the broadened Landau levels. $\delta\epsilon(B)$ defines the actual width of the Landau level states contributing to the conductance. 82

4.10 Output of the simulation for a given set of input parameters ($E_Z/E_c = 4.3$). a) The electrochemical potential (green curve) is displayed together with the Landau level spectrum for spin up (red lines) and spin down (blue lines). b) Experimental magneto-resistance (black curve) superimposed with the calculated one (orange curve). c) Longitudinal conductivity for spin up (red curve) and spin down (blue curve). d) The transverse resistivity computed using equation 4.7 (solid line) or from classical formula (dotted line). e) Landau level broadening $\Gamma(B)$ compared with the energy cut-off function $1/2\delta\epsilon(B)$. 85

4.11 Experimental magneto-resistance superimposed with the simulated curves for selected back-gate voltages. 86

4.12 a) The hole carrier density extracted from the simulation (dots) and from the plane capacitor model (line). b) Extracted quantum hole mobility from the simulation. 87

4.13 Simulation results (orange curves) are compared to the experimental data for $V_{BG} = -102.5\,V$ (black curve), for different possible values of E_z/E_c offset by ± 2. a) For $E_z/E_c = 2.56$, the overall fit is fair but the 1/B-periodic oscillations in the weak magnetic field regime is questionable. b) The best fit is obtained for $E_z/E_c = 4.56$ c) For $E_z/E_c = 6.56$, a transition from the mixed to polarized regime is expected, but not observed experimentally. 90

4.14 a) Comparison of the Landau level energy spectrum between the massive Dirac fermion (MDF) model and the Schrödinger (SCHF) fermion model at a given magnetic field. The same Landau level spectra are evidenced here with $E_z/E_c = 3.2$ for the MDF model and $E_z/E_c = 4.2$ for the SCHF model 91

4.15 Extracted values of Ez/Ec as a function the hole density. The pink dots are the values obtained assuming the SCHF Landau level structure. By down-shifting these values by 1 (light pink dots), we obtain the values corresponding to the MDF LLs structure. The E_z/E_c ratio is compared to the values found in the literature (blue and green dots), where either the MDF (light color) or SCHF (vivid color) model was considered. Only parts of the experimental data (see main text for details). 92

4.16 Evolution of the Landé factor g^* (left) and the ratio E_z/E_c (right) versus the interaction parameter r_s (bottom) and the carrier density n^h (top) as a function of the carrier density, on the same graph, for two different models. g^* increases as the interaction parameter r_s increases, evidencing an interaction enhanced g-factor in this system. We used $\epsilon_r^{WSe_2,BN} = 1/2.\left(\epsilon_r^{vacuum} + \epsilon_r^{BN}\right) = 2.4$ to compute r_s. 93

6.1 Schémas des polymorphes de DCMT de gauche à droite : 1T (symétrie tétragonale, une couche par cellule unité, coordination octaédrique de l'atome métallique), 2H (symétrie hexagonale avec deux couches par cellule unité, coordination prismatique trigonale de l'atome metallique) et 3R (symétrie rhomboédrique avec trois couches par cellule unité, coordination prismatique trigonale de l'atome métallique). Adapté de [28] 101

6.2 a) réseau réél et b) réseau réciproque d'une monocouche de DCMT. . 101

6.3 Levée de la dégénérescence de spin aux points K et K' de la première zone de Brillouin d'une monocouche de WSe_2. Adapté de [9] 102

6.4 Les propriétés électroniques des bicouches DCMT ressemblent à celles de deux DCMT monocouches tournées de 180° l'une par rapport à l'autre. Dans l'espace réciproque, les bords de la première zone de Brillouin (points K et K') sont une superposition des états de chaque monocouche, conduisant à des états de spin dégénérés. 103

6.5 (a),(b) structure de bande calculée pour tricouche MoS_2 et 6-couches WS_2. Adapté de [56]. 103

6.6 Composantes du tenseur de conductivité (a) et de résistivité (b) en fonction du champ magnétique. 105

6.7 (a) Densité d'états pour un gaz d'électrons libres et indépendants en presence d'un champ magnétique. (b) Energie des niveaux de Landau en fonction du champ magnétique. La pente dépend du nombre quantique N (noté n dans la figure). 106

6.8 (a) Les niveaux de Landau sont élargis à cause du désordre. (b) La somme des niveaux de Landau élargis définit la densité des états totale. La modulation de la densité d'états induite par le champ magnétique peut être détectée expérimentalement si les niveaux de Landau individuels sont suffisamment séparés. Adapté de [65, 70] 106

6.9 Dispositif de micro-alignement des flocons de DCMTs et de h-BN . . 109

6.10 a) et b) Dessin des macro-electrodes et des micro-éléctrodes. c) Géométrie barre de Hall typique utilisée 110

6.11 Microscope à force atomique (AFM) utilisé pour la détermination de l'épaisseur des flocons. Illustration du mode tapping. 111

6.12 Cliché de microscopie électronique en transmission dans lequel le flocon de h-BN apparait comme des franges sombres et claires tandis que le flocon de WSe_2 apparait comme une alternance de points sombres et clairs. 111

6.13 a) Courant drain-source pour différentes valeures de la tension de grille de $-45\,\mathrm{V}$ à $-90\,\mathrm{V}$ par pas de $-2.5\,\mathrm{V}$ dans un flocon multi-couches de WSe_2. b) Représentation du courant drain-source avec une carte de couleur en fonction de V_{BG} et V_{ds} pour un flocon monocouche de WSe_2 112

6.14 Profile du champ magnétique pulsé, atteignant 60 T au maximum. Encart: photographie d'une bobine permettant la génération de champs magnétiques. 113

6.15 a) Image au microscope optique de l'échantillon : une mono-couche de WSe_2 difficilement visible attachée à un flocon épais. Le flocon de WSe_2 et le flocon de BN sur lequel il repose sont entourées de lignes rouges et bleues, respectivement. b) Schéma de connexion électrique des électrodes de mesure de l'échantillon. La densité de porteurs peut être modifiées par effet de champ à l'aide de la tension de grille V_{BG} appliquée sur le substrat de silicium. 114
6.16 Magnéto-résistance à fort champ magnétique d'une mono-couche de WSe_2 à $T = 4.2\,K$, pour plusieurs tensions de grille. Les courbes sont décalées verticalement et réparties sur deux graphiques pour davantage de lisibilité. 116
6.17 Magnéto-résistance expérimentale superposée aux courbes simulées pour certaines tensions de grille. 118
6.18 Valeurs de Ez/Ec extraites de la simulation en fonction de la densité de trous. Les points roses correspondent au modèle impliquant des fermions de Schrödinger (SCHF). En diminuant ces valeurs de 1 (points roses clair), nous obtenons les valeurs du rapport E_z/E_c avec le modèle impliquant des fermions de Dirac massifs (MDF). Ces grandeurs sont comparées à celles de la littérature (points bleus et verts), où le modèle MDF (couleurs claires) ou SCHF (couleurs vives) sont reportés. . . . 120

List of Tables

1.1 Space groups and wave vector symmetry elements for 2H TMDCs. Adapted from [27]. 6

3.1 Pattern parameters for micro and macro-electrodes. 50
3.2 Etching parameters. 53

4.1 List of parameters for the simulation and their effect on the simulated magneto-resistance 84

Bibliography

[1] Klaus von Klitzing , Reviews of Modern Physics **58**, 519 (1986)

[2] Stormer, Horst L and Tsui, Daniel C and Gossard, Arthur C , Reviews of Modern Physics **71**, S298 (1999)

[3] Novoselov Kostya. S and Geim Andre. K and Morozov Sergei. V and Jiang D. and Zhang. Y, and Dubonos Sergey. V and Grigorieva Irina. V and Firsov Alexandr. A, Science **306**, 666 (2004).

[4] David J. Thouless, F. Duncan M. Haldane, J. Michael Kosterlitz , Nobel prize lectures **2016**

[5] K. S. Novoselov, A. K. Geim, S. V. Morozov, D. Jiang, M. I. Katsnelson, I. V. Grigorieva, S. V. Dubonos, and A. A. Firsov, Nature **438**, 197 (2005).

[6] A. Splendiani, L. Sun, Y. Zhang, T. Li, J. Kim, C.-Y. Chim, G. Galli, and F. Wang, Nano Letters **10**, 1271 (2010)

[7] K. F. Mak, C. Lee, J. Hone, J. Shan, and T. F. Heinz, Physical Review Letters **105**, 136805 (2010).

[8] Gusakova, Julia and Wang, Xingli and Shiau, Li Lynn and Krivosheeva, Anna and Shaposhnikov, Victor and Borisenko, Victor and Gusakov, Vasilii and Tay, Beng Kang, physica status solidi (a) **214**, 1700218 (2017).

[9] D. Xiao, G. B. Liu, W. X. Feng, X. D. Xu, and W. Yao, Physical Review Letters **108**, 196802 (2012).

[10] W. Zhao, Z. Ghorannevis, L. Chu, M. Toh, C. Kloc, P.-H. Tan, and G. Eda, ACS Nano **7**, 791 (2013).

[11] R. Pisoni, Z. J. Lei, P. Back, M. Eich, H. Overweg, Y. Lee, K. Watanabe, T. Taniguchi, T. Ihn, and K. Ensslin, Applied Physics Letters **112**, 123101 (2018).

[12] M. V. Gustafsson, M. Yankowitz, C. Forsythe, D. Rhodes, K. Watanabe, T. Taniguchi, J. Hone, X. Y. Zhu, and C. R. Dean, Nature Materials **17**, 411 (2018).

[13] H. C. P. Movva, B. Fallahazad, K. Kim, S. Larentis, T. Taniguchi, K. Watanabe, S. K. Banerjee, and E. Tutuc, Physical Review Letters **118**, 247701 (2017).

[14] Allain, Adrien and Kis, Andras, Acs Nano**8**, 7180 (2014).

[15] Z. Y. Zhu, Y. C. Cheng, and U. Schwingenschlogl, Physical Review B **84**, 153402 (2011).

[16] J. Lin, T. Han, B. A. Piot, Z. Wu, S. Xu, G. Long, L. An, P. Cheung, P. P. Zheng, P. Plochocka, X. Dai, D. K. Maude, F. Zhang, and N. Wang, Nano Letters **19**, 1736 (2019).

[17] F. Rose, M. O. Goerbig, and F. Piechon, Physical Review B **88**, 125438 (2013).

[18] D. Le, A. Barinov, E. Preciado, M. Isarraraz, I. Tanabe, T. Komesu, C. Troha, L. Bartels, T. S. Rahman, and P. A. Dowben, Journal of Physics: Condensed Matter **27**, 182201 (2015).

[19] X. Li, F. Zhang, and Q. Niu, Physical Review Letters **110**, 066803 (2013).

[20] A. Kormanyos, P. Rakyta, and G. Burkard, New Journal of Physics **17**, 103006 (2015).

[21] Z. F. Wang, J. Shan, and K. F. Mak, Nature Nanotechnology **12**, 144 (2017).

[22] Z. F. Wang, J. Shan, and K. F. Mak, Physical Review B **95**, 155406 (2017).

[23] T. Ando and Y. Uemura, Journal of the Physical Society of Japan **36**, 959 (1974).

[24] R. R. Gerhardts, Physica Status Solidi B **245**, 378 (2008).

[25] Wilson. JA and Yoffe. AD, Physical Review Letters **18**, 193 (2006).

[26] Mak, Kin Fai and He, Keliang and Shan, Jie and Heinz, Tony F, Nature nanotechnology **7**, 494 (2012).

[27] Ribeiro-Soares, Jenaina and Almeida, RM and Barros, Eduardo B and Araujo, Paulo T and Dresselhaus, Mildred S and Cançado, Luiz G and Jorio, Ado, Physical Review B **90**, 115438 (2014).

[28] Kolobov, Alexander V and Tominaga, Junji, Springer **239**,(2016).

[29] Chu, Rui-Lin and Liu, Gui-Bin and Yao, Wang and Xu, Xiaodong and Xiao, Di and Zhang, Chuanwei, Physical Review B **89**, 155317 (2014).

[30] Jiang, Tao and Liu, Hengrui and Huang, Di and Zhang, Shuai and Li, Yingguo and Gong, Xingao and Shen, Yuen-Ron and Liu, Wei-Tao and Wu, Shiwei, Nature nanotechnology **9**, 825 (2014).

[31] Tinkham, Michael, McGraw-Hill **0-486-43247-5**, (1992).

[32] F. Hulliger, Springer **306**, 83 (1968).

[33] Chhowalla, Manish and Shin, Hyeon Suk and Eda, Goki and Li, Lain-Jong and Loh, Kian Ping and Zhang, Hua, Nature chemistry **5**, 263 (2013).

[34] Li, Tianshu and Galli, Giulia, The Journal of Physical Chemistry C **111**, 16192 (2007).

[35] Ugeda, Miguel M and Bradley, Aaron J and Shi, Su-Fei and Felipe, H and Zhang, Yi and Qiu, Diana Y and Ruan, Wei and Mo, Sung-Kwan and Hussain, Zahid and Shen, Zhi-Xun and others, Nature materials **13**, 1091 (2014).

[36] Schmidt, Hennrik and Giustiniano, Francesco and Eda, Goki, Chemical Society Reviews **44**, 7715 (2015).

[37] Roldán, Rafael and Silva-Guillén, Jose A and López-Sancho, M Pilar and Guinea, Francisco and Cappelluti, Emmanuele and Ordejón, Pablo, Annalen der Physik **526**, 9 (2014).

[38] Mattheiss, LF, Physical Review B **8**, 3719 (1973).

[39] Dresselhaus, Gene, Physical Review **100**, 580 (1955).

[40] Liu, Gui-Bin and Xiao, Di and Yao, Yugui and Xu, Xiaodong and Yao, Wang, Chemical Society Reviews **44**, 2643 (2015).

[41] Ramasubramaniam, Ashwin, Physical Review B **86**, 115409 (2012).

[42] Dresselhaus, Mildred S and Dresselhaus, Gene and Jorio, Ado, Springer **ISBN 978-3-642-06945-1**, 2008.

[43] Gong, Zhirui and Liu, Gui-Bin and Yu, Hongyi and Xiao, Di and Cui, Xiaodong and Xu, Xiaodong and Yao, Wang, Nature communications **4**, 2035 (2013).

[44] Splendiani, Andrea and Sun, Liang and Zhang, Yuanbo and Li, Tianshu and Kim, Jonghwan and Chim, Chi-Yung and Galli, Giulia and Wang, Feng, Nano letters **10**, 1271 (2010).

[45] Zeng, Hualing and Liu, Gui-Bin and Dai, Junfeng and Yan, Yajun and Zhu, Bairen and He, Ruicong and Xie, Lu and Xu, Shijie and Chen, Xianhui and Yao, Wang and others, Scientific reports **3**, 1608 (2013).

[46] Cheiwchanchamnangij, Tawinan and Lambrecht, Walter RL, Physical Review B **85**, 205302 (2012).

[47] Kadantsev, Eugene S and Hawrylak, Pawel, Solid State Communications **152**, 909 (2012).

[48] Kormányos, Andor and Zólyomi, Viktor and Drummond, Neil D and Burkard, Guido, Physical Review X **4**, 011034 (2014).

[49] He, Jiangang and Hummer, Kerstin and Franchini, Cesare, Physical Review B **89**, 075409 (2014).

[50] Ramasubramaniam, Ashwin and Naveh, Doron and Towe, Elias, Physical Review B **84**, 205325 (2011).

[51] Tonndorf, Philipp and Schmidt, Robert and Böttger, Philipp and Zhang, Xiao and Börner, Janna and Liebig, Andreas and Albrecht, Manfred and Kloc, Christian and Gordan, Ovidiu and Zahn, Dietrich RT and others, Optics express **21**, 4908 (2013).

[52] Debbichi, L and Eriksson, Olle and Lebègue, Sébastien, Physical Review B **89**, 205311 (2014).

[53] Liu, Qihang and Li, Linze and Li, Yafei and Gao, Zhengxiang and Chen, Zhongfang and Lu, Jing, The Journal of Physical Chemistry C **3116**, 21556 (2012).

[54] Ruiz-Tijerina, David A and Danovich, Mark and Yelgel, Celal and Zólyomi, Viktor and Fal'ko, Vladimir I, Physical Review B **98**, 035411 (2018).

[55] Wu, Zefei and Xu, Shuigang and Lu, Huanhuan and Khamoshi, Armin and Liu, Gui-Bin and Han, Tianyi and Wu, Yingying and Lin, Jiangxiazi and Long, Gen and He, Yuheng and others, Nature communications **7**, 1 (2016).

[56] Liu, Hongjun and Chen, Jinglei and Yu, Hongyi and Yang, Fang and Jiao, Lu and Liu, Gui-Bin and Ho, Wingking and Gao, Chunlei and Jia, Jinfeng and Yao, Wang and others, Nature communications **6**, 1 (2015).

[57] Dresselhaus, Mildred S and Dresselhaus, Gene and Jorio, Ado, Springer **ISBN 978-3-642-06945-1**, 2008.

[58] Kubota, Yoichi and Watanabe, Kenji and Tsuda, Osamu and Taniguchi, Takashi, Science **317**, 932 (2007).

[59] Hall, Edwin H and others, American Journal of Mathematics **2**, 3 (1879).

[60] Hall, EH, American Journal of Science **11**, 200 (1880).

[61] Lüth, Hans and Ibach, Harald, Springer-Verlag Berlin Heidelberg **2003**.

[62] Fowler, Alan B and Fang, Frank F and Howard, William E and Stiles, Philip J, Physical Review letters **16**, 901 (1966).

[63] Schubnikow, L and De Haas, WJ, Nature **126**, 500 (1930).

[64] Heinzel, Thomas and Zozoulenko, Igor, Wiley Online Library **ISBN: 9783527618910**, (2003).

[65] Ihn, Thomas, Oxford University Press **ISBN-13: 9780199534425**, 2010.

[66] ahay, Marc and Bandyopadhyay, Supriyo, John Wiley & Sons **ISBN 9721118988756** , 2017.

[67] Ando, Tsuneya and Fowler, Alan B and Stern, Frank, Reviews of Modern Physics **54**, 437 (1982).

[68] Laikhtman, B and Altshuler, EL, Annals of Physics **232**, 332 (1994).

[69] Dingle, RB, Proceedings of the Royal Society of London. Series A. Mathematical and Physical Sciences **211**, 517 (1952).

[70] Ferry, David and Goodnick, Stephen Marshall, Cambridge university press **ISBN 0-521-66365-2**,1999.

[71] Shrestha, Keshav and Marinova, Vera and Graf, David and Lorenz, Bernd and Chu, Ching Wu, Physical Review B **95**, 075102 (2017).

[72] Park, Hamin and Shin, Gwang Hyuk and Lee, Khang June and Choi, Sung-Yool, Nanoscale **10**, 15205 (2018).

[73] Fogiel, Max, Research and Education Association **ISBN 0878915036** (1972).

[74] Brotons-Gisbert, M and Sánchez-Royo, JF and Martínez-Pastor, JP, Applied Surface Science **354**, 453 (2015).

[75] Gao, Libo and Ren, Wencai and Li, Feng and Cheng, Hui-Ming, ACS nano **2**, 1625 (2008).

[76] Wei, Yaxu and Hu, Chunguang and Li, Yanning and Hu, Xiaotang and Yu, Kaihao and Sun, Litao and Hohage, Michael and Sun, Lidong, Nanotechnology **31**, 315710 (2020).

[77] Zhan, Yongjie and Liu, Zheng and Najmaei, Sina and Ajayan, Pulickel M and Lou, Jun, Nano-Micro small **8**, 966 (2012).

[78] Laturia, Akash and Van de Put, Maarten L and Vandenberghe, William G, npj 2D Materials and Applications **2**, 1 (2018).

[79] Lin, Xiaoyang and Si, Zhizhong and Fu, Wenzhi and Yang, Jianlei and Guo, Side and Cao, Yuan and Zhang, Jin and Wang, Xinhe and Liu, Peng and Jiang, Kaili and others, Nano Research **11**, 6316 (2018).

[80] Li, Yuhao and Kong, Yangyang and Peng, Jinlin and Yu, Chuanbin and Li, Zhi and Li, Penghui and Liu, Yunya and Gao, Cun-Fa and Wu, Rong, Journal of Materiomics **5**, 413 (2019).

[81] Pech-Canul, Martin I and Ravindra, Nuggehalli M, Springer **ISBN 978-3-030-02169-6**, 666 (2019).

[82] Eda, Goki and Yamaguchi, Hisato and Voiry, Damien and Fujita, Takeshi and Chen, Mingwei and Chhowalla, Manish, Nano letters **11**, 5111 (2011).

[83] Molina-Sanchez, Alejandro and Wirtz, Ludger, Physical Review B **84**, 155413 (2011).

[84] Zahn, Dietrich RT and Tonndorf, Philipp and Schmidt, Robert and Böttger, Philipp and Zhang, Xiao and Börner, Janna and Liebig, Andreas and Albrecht, Manfred and Gordan, Ovidiu and de Vasconcellos, Steffen Michaelis and others, Optics express **21**, 4908 (2013).

[85] Zhang, Xin and Qiao, Xiao-Fen and Shi, Wei and Wu, Jiang-Bin and Jiang, De-Sheng and Tan, Ping-Heng, Chemical Society Reviews **44**, 2757 (2015).

[86] Larentis, Stefano, PhD thesis **2018**.

[87] Zhao, Weijie and Ghorannevis, Zohreh and Chu, Leiqiang and Toh, Minglin and Kloc, Christian and Tan, Ping-Heng and Eda, Goki, ACS nano **7**, 791 (2013).

[88] Yan, Tengfei and Qiao, Xiaofen and Liu, Xiaona and Tan, Pingheng and Zhang, Xinhui, Applied Physics Letters **105**, 3895 (2014).

[89] Yamamoto, Mahito and Wang, Sheng Tsung and Ni, Meiyan and Lin, Yen-Fu and Li, Song-Lin and Aikawa, Shinya and Jian, Wen-Bin and Ueno, Keiji and Wakabayashi, Katsunori and Tsukagoshi, Kazuhito, Acs Nano **8**, 3895 (2014).

[90] Liang, Fang and Xu, Hejun and Wu, Xing and Wang, Chaolun and Luo, Chen and Zhang, Jian, Chinese Physics B **27**, 037802 (2018).

[91] Streetman, Ben G and Banerjee, Sanjay, Prentice Hall, 1995 **ISBN 013149726X**, (2001).

[92] Movva, Hema Chandra Prakash, PhD thesis **0000-0003-3001-3171**, (2018).

[93] Chuang, Hsun-Jen and Tan, Xuebin and Ghimire, Nirmal Jeevi and Perera, Meeghage Madusanka and Chamlagain, Bhim and Cheng, Mark Ming-Cheng and Yan, Jiaqiang and Mandrus, David and Tomanek, David and Zhou, Zhixian, Nano letters **14**, 3594 (2014).

[94] Derry, GN and Ji-Zhong, Zhang, Physical Review B **39**, 1940 (1989).

[95] Kim, Kyounghwan and Larentis, Stefano and Fallahazad, Babak and Lee, Kayoung and Xue, Jiamin and Dillen, David C and Corbet, Chris M and Tutuc, Emanuel, ACS nano **9**, 4527 (2015).

[96] Bals, Sara and Tirry, Wim and Geurts, Remco and Yang, Zhiqing and Schryvers, Dominique, Microscopy and Microanalysis **13**, 80 (2007).

[97] Nellist, Peter D, Science of microscopy **ISBN 978-1-4419-7199-9**, 65 (2007).

[98] Ghatak, Subhamoy and Pal, Atindra Nath and Ghosh, Arindam, ACS nano **5**, 7707 (2011).

[99] Park, Woanseo and Park, Juhun and Jang, Jingon and Lee, Hyungwoo and Jeong, Hyunhak and Cho, Kyungjune and Hong, Seunghun and Lee, Takhee, Nanotechnology **24**, 095202 (2013).

[100] Late, Dattatray J and Liu, Bin and Matte, HSS Ramakrishna and Dravid, Vinayak P and Rao, CNR, ACS nano **6**, 5635 (2012).

[101] Namgung, Seok Daniel and Yang, Suk and Park, Kyung and Cho, Ah-Jin and Kim, Hojoong and Kwon, Jang-Yeon, Nanoscale research letters **10**, 1 (2015).

[102] Liu, Zheng and Gong, Yongji and Zhou, Wu and Ma, Lulu and Yu, Jingjiang and Idrobo, Juan Carlos and Jung, Jeil and MacDonald, Allan H and Vajtai, Robert and Lou, Jun and others, Nature communications **4**, 61 (2013).

[103] Paszkowicz, W and Pelka, JB and Knapp, M and Szyszko, T and Podsiadlo, SJAPA, Applied Physics A **75**, 431 (2002).

[104] Liu, Gui-Bin and Shan, Wen-Yu and Yao, Yugui and Yao, Wang and Xiao, Di, Physical Review B **88**, 8 (2013).

[105] Raikh, M. E. and Shahbazyan, T. V., Phys. Rev. B **47**, 1522 (1993).

[106] Attaccalite, Claudio and Moroni, Saverio and Gori-Giorgi, Paola and Bachelet, Giovanni B., Physical Review Letter **88**, 256601 (2002).

[107] Wang, Zefang and Shan, Jie and Mak, Kin Fai, Nature nanotechnology **12**, 144 (2017).

[108] Li Lu Hua, Xing Tan, Chen Ying, and Jones Rob, Advanced materials interfaces **1**, 1300132 (2014).

[109] Rolf R. Gerhardts, Surface science **58**, 227 (1976).

[110] Banan Kerdi, Mathieu Pierre, Robin Cours, Bénédicte Warot-Fonrose, Michel Goiran, and Walter Escoffier, Physical Review B **102**, 1555106 (2020).